# Phases and phase transitions in non-equilibrium quantum matter

*Oliver Lunt*

A dissertation submitted in partial fulfillment
of the requirements for the degree of
**Doctor of Philosophy**
of
**University College London**.

Department of Physics & Astronomy
University College London

August 5th, 2021

I, Oliver Lunt, confirm that the work presented in this report is my own. Where information has been derived from other sources, I confirm that this has been indicated in the work.

# Abstract

This thesis focuses on two recent examples of non-equilibrium quantum phase transitions. In the first part we discuss discrete time crystals (DTCs), which are defined by the fact that they spontaneously break discrete time-translation symmetry. In early realizations of DTCs, many-body localization (MBL) played a crucial role in preventing the periodic drive from heating the system to infinite temperature, which would preclude any possibility of symmetry-breaking. This thesis explores the possibility that dissipation may play an equivalent role, allowing for the possibility of time-translation symmetry-breaking without MBL. We describe the results of an experiment exploring DTC order in a doped semiconductor system with significant dissipation, and a potential description of the interplay of driving, dissipation and interactions using a central spin model.

In the second part we discuss measurement-induced phase transitions, where the steady-state entanglement can undergo a phase transition as a function of the measurement rate. First we explore the role of the underlying unitary dynamics in the nature of the phase transition. Previous work has revealed an apparent dichotomy between interacting and non-interacting systems, where interacting systems have a phase transition from volume-law to area-law entanglement at a finite critical measurement rate $p$, whereas the volume-law for non-interacting systems is destroyed at any $p > 0$. We study this transition for MBL systems, and find an interpolation between these extremes depending on the measurement basis. We discuss the relevance of the emergent integrability characteristic of MBL and how this intersects with the measurements. Next we study the critical properties of this transition in random 1+1D and 2+1D Clifford circuits, aiming to explore connections with percolation. We utilize a graph-state based simulation algorithm, which provides access to geometric properties of entanglement. We find bulk exponents close to percolation, but possible differences in surface behaviour.

# Impact Statement

Many of the potential applications of quantum mechanics, such as in computing, communication, and metrology, require the creation and control of quantum states away from thermal equilibrium. Some of the key challenges in these fields are related to the fact that in many cases thermalization seems inevitable. But in recent years it has been realized that there are some mechanisms by which we can robustly avoid thermalization and its limitations. This thesis explores some novel phases and phase-transitions that are enabled by this move away from thermal equilibrium. Some of these phases may have near-term technological applications — discrete time crystals could potentially play a role in metrology, given their robust subharmonic response — but as with many aspects of fundamental physics, the most impactful applications may not yet be apparent. More generally, this thesis provides a small contribution to our collective exploration into the new world of non-equilibrium phases of matter.

# Acknowledgements

First I would like to thank my supervisor, Arijeet Pal, for his help and guidance throughout my PhD. He involved me in several collaborations, while also giving me the freedom to work on what I found most interesting. An important part of the PhD process is learning to think more broadly about what really matters, and to this end I have learnt a lot from Arijeet.

I would also like to thank my collaborators James O'Sullivan, John Morton, and Marcin Szyniszewski. Without their input the work in this thesis would either have been impossible or far diminished.

My time at UCL has been greatly enriched by being a member of the CDT in 'Delivering Quantum Technologies'. I would like to thank all the academics involved in the CDT for creating such a great environment at UCL for people interested in all things quantum. The friends I made through the CDT had a great impact on my general quality of life at UCL. In particular I would like to thank Tom Farshi, Tom Scruby, and Jake Tommey for many lunches that stretched perhaps a little too far into the afternoon.

I would not be writing this without the continued love and support of my parents. Throughout my life they impressed on me the importance of doing something you enjoy, and gave me the freedom to do so. I may well not have been at UCL were it not for the internet sleuthing of my girlfriend, Rachel. Thank you for all the time we have spent together, and for patiently sitting through many pained explanations involving time crystals and starlings.

I would like to dedicate this thesis to my late grandfather, Michael. I can still remember as a young boy him earnestly trying to teach me Ohm's law — I think at that age I did not quite know my current from my voltage, but as I grew up he was always keenly interested in what I had been learning. At one point I sent him my university lecture notes on linear algebra, which in hindsight might have been a step too far, even if he did graciously accept them! He played a formative role in shaping where I am today, and for that I am grateful.

This thesis is based on work contained in the following publications:

- J. O'Sullivan, O. Lunt, C. W. Zollitsch, M. L. W. Thewalt, J. J. L. Morton, A. Pal, *Signatures of discrete time crystalline order in dissipative spin ensembles*, New Journal of Physics **22** 085001 (2020).
- O. Lunt, A. Pal, *Measurement-induced entanglement transitions in many-body localized systems*, Physical Review Research **2**, 043072 (2020).
- O. Lunt, M. Szyniszewski, A. Pal, *Dimensional hybridity in measurement-induced criticality*, arXiv:2012.03857 (2020).

# Contents

## I Discrete time crystals 1

**1 Background 3**

1.1 Absence of continuous time-translation symmetry breaking . 5

1.2 Discrete time-translation symmetry breaking . . . . . . . . . . 8

1.2.1 Definitions of discrete TTSB . . . . . . . . . . . . . . . . 8

1.2.2 Robustness to perturbations . . . . . . . . . . . . . . . . . 10

1.2.3 The issue of heating . . . . . . . . . . . . . . . . . . . . 11

1.3 Experimental evidence of a many-body localized time crystal . . . . . . . . . . . . . . . . . . . . . . . . . 12

1.3.1 Echoing out the disorder . . . . . . . . . . . . . . . . . . . 14

**2 Dissipative discrete time crystals 17**

2.1 DTCs in phosphorous-doped silicon . . . . . . . . . . . . . . . 17

2.2 Experimental observations . . . . . . . . . . . . . . . . . . . . 20

2.3 Theoretical model . . . . . . . . . . . . . . . . . . . . . . . . 22

2.3.1 Description of the model . . . . . . . . . . . . . . . . . . 23

2.3.2 Order parameters for the DTC phase diagram . . . . . 25

2.3.3 Analysis of the phase diagram . . . . . . . . . . . . . . 26

2.4 Comment on the crystalline fraction as a probe for DTC order 28

2.5 Conclusion . . . . . . . . . . . . . . . . . . . . . . . . . . . . 31

# II Measurement-induced phase transitions 33

3 **Background** **35**
  3.1 Entanglement scaling . . . . . . . . . . . . . . . . . . . . . . . . . . 35
  3.2 Entanglement phase transitions . . . . . . . . . . . . . . . . . . . . 37
  3.3 Measurement-induced transitions . . . . . . . . . . . . . . . . . . 37
  3.4 Transitions in the Rényi entropies . . . . . . . . . . . . . . . . . . 39
  3.5 Analytically tractable limits . . . . . . . . . . . . . . . . . . . . . 40
    3.5.1 Transition in the ($n = 0$)-Rényi entropy . . . . . . . . . 40
    3.5.2 Transition in the ($n \geq 1$)-Rényi entropies . . . . . . . . 44
  3.6 Numerical studies of universality . . . . . . . . . . . . . . . . . . 51
    3.6.1 Diagnostics of the transition . . . . . . . . . . . . . . . . . 53
  3.7 Connection with quantum information scrambling . . . . . . . 56
  3.8 Scalability in experiments . . . . . . . . . . . . . . . . . . . . . . 58

4 **Measurement-induced transitions in many-body localized systems** **61**
  4.1 Model . . . . . . . . . . . . . . . . . . . . . . . . . . . . . . . . . . 64
    4.1.1 Transition diagnostics . . . . . . . . . . . . . . . . . . . . 65
    4.1.2 Diagonal entropy . . . . . . . . . . . . . . . . . . . . . . . 66
  4.2 Entanglement dynamics with Z-basis measurements . . . . . . 67
  4.3 Entanglement dynamics with X-basis measurements . . . . . . 70
  4.4 Discussion . . . . . . . . . . . . . . . . . . . . . . . . . . . . . . . 76

5 **Measurement-induced criticality in Clifford circuits** **81**
  5.1 Methods . . . . . . . . . . . . . . . . . . . . . . . . . . . . . . . . 86
    5.1.1 Model . . . . . . . . . . . . . . . . . . . . . . . . . . . . . 86
    5.1.2 Simulation method . . . . . . . . . . . . . . . . . . . . . . 88
    5.1.3 Transition diagnostics . . . . . . . . . . . . . . . . . . . . 89
  5.2 Entanglement transition . . . . . . . . . . . . . . . . . . . . . . . 90
  5.3 Purification transition . . . . . . . . . . . . . . . . . . . . . . . . 98
  5.4 Entanglement clusters . . . . . . . . . . . . . . . . . . . . . . . . 106
  5.5 Discussion . . . . . . . . . . . . . . . . . . . . . . . . . . . . . . . 114

5.A Alternative scaling forms for $I_3$ . . . . . . . . . . . . . . . . . . . . 117
5.B Details of the finite-size scaling . . . . . . . . . . . . . . . . . . . . 118
5.C Critical entanglement dynamics . . . . . . . . . . . . . . . . . . . . 120
5.D Entanglement clusters in the projective transverse field Ising model . . . . . . . . . . . . . . . . . . . . . . . . . . . . 121

**Bibliography** **125**

# List of Figures

1.1 An example of how the subharmonic peak at $\nu = \nu_{\text{drive}}/2$ is not robust against pulse errors for a non-interacting system. This behaviour should appear for many order parameters, but for concreteness one could look at the Fourier spectrum of $\sigma^z$ for one of the spins. . . . . . . . . . . . . . . . . . . . . . . . . . 11

1.2 An overview of the drive protocol used in the MBL trapped ion experiment. Figure taken from Ref. [26]. . . . . . . . . . . . 14

1.3 An overview of the main results of the experiment with MBL trapped ions in Ref. [26], from which these figures have been adapted. Here $\epsilon$ is the rotation error, $W$ controls the strength of the disorder, and $J_0$ controls the strength of the spin-spin interactions. All figures have a fixed nonzero rotation error of $\epsilon = 0.03$. **(a)** No disorder and no interactions results in a subharmonic peak which is unstable to rotation errors. **(b)** Having disorder but no interactions also does not result in a stable subharmonic peak. **(c)** Only the combination of disorder and interactions results in a stable subharmonic peak. . . . . . 15

2.1 An overview of the pulse protocol for the experiment with phosphorous-doped silicon outlined in Ref. [32], from which this figure is adapted. The main part of the drive protocol, outlined in dashed lines, consists of two stages: a 'spin-locking' stage where the spins are free to interact, and a $\pi$-pulse, where the spins are flipped using the BB1 protocol to ensure spatially uniform rotations. . . . . . . . . . . . . . . . . . . . . . . . . . 19

2.2 Experimental data showing a comparison between the normalized Fourier spectra for the trivial phase **(a)** and the DTC phase **(b)**, for a fixed rotation error of $\epsilon = 0.01$. Whereas the subharmonic peak splits for any nonzero $\epsilon$ in the trivial phase, in the DTC phase the subharmonic peak is fixed at $\nu_F/2$ for small but nonzero $\epsilon$. The DTC phase corresponds to $\tau_{\text{lock}} = 100\tau_{\text{flip}}$, while the trivial phase corresponds to $\tau_{\text{lock}} = 10\tau_{\text{flip}}$. . . . . . . 20

2.3 A comparison between experiment and theory of the splitting of the subharmonic Fourier peak as a function of the rotation error $\epsilon$. Whereas in the DTC phase the subharmonic peak remains fixed at half the Floquet frequency in a finite window around $\epsilon = 0$, in the trivial phase it splits immediately for any $\epsilon \neq 0$. The DTC phase corresponds to $\tau_{\text{lock}} = 100\tau_{\text{flip}}$, while the trivial phase corresponds to $\tau_{\text{lock}} = 10\tau_{\text{flip}}$. The asymmetry of the trivial phase data around $\epsilon = 0$ is discussed in the main text. . . . . . . . . . . . . . . . . . . . . . . . . . . . . . . . 21

2.4 Phase diagram of the discrete time crystal with competing dissipation and interactions, using two different order parameters. Fig. 2.4a includes experimental data exploring the strong dissipation/weak interaction phase boundary. **(a)** Phase diagram from the Fourier spectrum of $\langle\sigma_0^z\rangle$, calculating using the driven central spin model coupled to a dissipative bath. The DTC phase corresponds to the dark region, where $\langle\sigma_0^z\rangle$ has a stable peak at half the drive frequency. Unlike the $\pi$-gap phase diagram, there is no dark region in the bottom right because we are looking at $\sigma^z$; in this region $\sigma^y$ exhibits period doubling instead. The red and white stars and corresponding Fourier spectra correspond to experiments with $\tau_{\text{lock}} = 10t_\pi$ and $\tau_{\text{lock}} = 100t_\pi$ respectively. **(b)** $\pi$-gap phase diagram of the discrete time crystal as a function of dephasing rate and $\sigma_i^y\sigma_j^y$ interaction strength. The DTC phase corresponds to $\Delta_\pi/\Delta_0 \ll 1$ (dark regions). The two plots at the bottom are slices through the phase diagram, the left at weak interactions and the right at weak dissipation. Both slices show a clear transition in the $\pi$-gap, though this is more pronounced for the dissipation-driven transition. **Parameters:** $\epsilon = 0.01$, $h = 10\,\text{Hz}$, $N = 5$, 10 disorder realizations; Fourier transforms calculated over $0 \leq n \leq 200$ Floquet periods. Phase diagram axes are in units of the Floquet frequency $\nu_F$. . . . . . . . . . . . . . . . . . . 27

2.5 The dependence of the crystalline fraction $f$ on the rotation angle $\theta = (1+\epsilon)\pi$ in an experiment aiming to observe DTC order in a system of NV centres in black diamond [33]. Here $\epsilon = 0$ corresponds to a perfect spin-flip. The claim is that the data with the longer interaction time $\tau_1 = 275\,\mathrm{ns}$ corresponds to the DTC phase, as evidenced by the 'plateau' dependence of $f$ on the rotation angle near $\theta = \pi$. The red diamonds are a rough indication of the phase boundary. . . . . . . . . . . . . . 29

2.6 The effect of nonuniform rotations on the crystalline fraction. **(a)** Comparison of the crystalline fraction against rotation error of the same sample with and without BB1 pulses turned on. The non-BB1 pulse sequence appears to have a flattened peak, while the BB1 crystalline fraction has no indication of a plateau. **(b)** Simulations of the crystalline fraction using the driven-dissipative central spin model using nonuniform rotation pulses. For a given disorder realization, the rotation error $\epsilon$ is drawn from a Gaussian distribution with mean $\bar{\epsilon}$ and variance $\sigma^2$, clipped at 10% to model the finite extent of the sample. We observe that large values of $\sigma$ result in a distinct flattening of the crystalline fraction curve, consistent with our experimental observations in Fig. 2.6a. . . . . . . . . . . . . . . . 30

3.1 A schematic of the minimal cut formalism for calculating the $(n = 0)$-Rényi entropy. Figure taken from Ref. [68]. . . . . . . . 41

3.2 Schematics for the calculation of the $(n = 0)$-Rényi entropy in the minimal cut formalism. The various entanglement phases correspond to different phases of classical percolation in the spacetime bulk of the quantum circuit, where measurements cut a fraction $p$ of the links. Figure taken from Ref. [68]. . . . . 43

3.3 The entanglement entropy is given by the free energy cost of inserting a domain wall connecting the endpoints of the entanglement region $A$. Figure taken from Ref. [100]. . . . . . 47

3.4 **(a)** Geometry of the statistical mechanical model arising from averaging over the unitary gates and the measurement outcomes. The circles correspond to 'spins' which take values in the permutation group $S_Q$. The values of the spins highlighted in red at the top are fixed by the boundary conditions (either the cyclic permutation for $Z_A$ or the identity for $Z_\emptyset$). **(b)** In the limit of infinite local Hilbert space dimension $q \to \infty$ the model reduces to a $Q$!-state Potts model on a square lattice. Figure taken from Ref. [75]. . . . . . . . . . . . . . . . . . . . . 49

3.5 **(a):** Geometry used to calculate the tripartite information. **(b):** Spacetime picture for calculating the tripartite information within the minimal cut formalism, taken from Ref. [72]. . . . . 54

4.1 **(a)** The critical properties of the transition depend on the measurement basis. Measurements in the X-basis result in a transition from volume-law to area-law entanglement at nonzero $p = p_c^X > 0$, similar to chaotic systems, whereas measurements in the Z-basis result in area-law entanglement for any nonzero $p$, similar to integrable systems. **(b)** Each stage of the dynamics consists of two steps. First the system is evolved in time with the unitary $U_{\mathrm{d}t} = \exp(-iH\mathrm{d}t)$, with $H$ given in Eq. (4.1), and then for each spin we projectively measure in a tensor-product basis with probability $p$ (measurements are represented by the red dots). **(c)** A schematic of the typical support of an 'l-bit' operator, localized at site $i$, in the fully MBL phase. **(d)** A depiction of the geometry used to calculate the tripartite information $I_3(A:B:C)$. . . . . . . . . . . . . . . 62

4.2 A comparison of the dynamics of the tripartite information $I_3$ for $p = 0$ and $p > 0$ with Z-basis measurements, with $N = 12$. For $p = 0$, $I_3$ grows logarithmically in time before saturating to a volume-law. For $p > 0$, $I_3$ initially grows in time, reaching an area-law peak, before decaying to a constant which decreases with system size. The inset shows that the dynamics can be reasonably well described by the scaling form $-I_3(t, p, N) = F[tp^\alpha/N^\gamma]/p^\beta N^\delta$, where $F$ is a single-parameter scaling function and $\alpha = 0.77$, $\beta = 0.80$, $\gamma = 1.14$ and $\delta = 2.19$. The inset data corresponds to 20 separate time series, with $N = 12, 16$ and $0.0005 \leq p \leq 0.005$. . . . . . . . . . . . . . . . . . 68

4.3 **(a)** Scaling of the von Neumann entropy at saturation with subsystem size for a system of size $N = 12$. For $p = 0$ this quantity obeys a volume-law, but for $p > 0$ it saturates to an area-law. **(b)** Scaling of the time $t_{\text{peak}}$ and height $I_3^{\text{max}}$ of the intermediate time peak in the tripartite information $I_3$, as seen in Fig. 4.2. The solid lines are power law fits, decaying approximately as $p^{-1}$. With increasing system size, the peak occurs at later times and is smaller in magnitude, indicating that it is (sub-)area-law. . . . . . . . . . . . . . . . . . . . . . . . . 69

4.4 Dynamics of the diagonal entropy $S_{\text{diag}}$ using the energy eigenbasis, with Z-basis measurements and $N = 12$. $S_{\text{diag}}$ is preserved by Hamiltonian evolution, so for $p = 0$ it remains constant in time. For $p > 0$, projective Z-basis measurements cause it to decay exponentially at a rate proportional to $p$. The inset shows the dependence of the early-time decay rate $\lambda$ on $p$ and $N$, with $\lambda \approx p$, independent of $N$. . . . . . . . . . . . . . 70

4.5 A comparison of the dynamics of the tripartite information $I_3$ with X-basis measurements for values of $p$ below and above the transition at $p_c^X \approx 0.014$. For $p = 0.0025$, $I_3$ grows logarithmically in time before saturating to a volume-law. By $p = 0.06$, the system size scaling has reversed, indicating a transition to an area law. . . . . . . . . . . . . . . . . . . . . . . . . . . . 71

4.6 Dynamics of the diagonal entropy $S_{\text{diag}}$ using the energy eigenbasis, with X-basis measurements and $N = 12$. $S_{\text{diag}}$ is preserved by Hamiltonian evolution, so for $p = 0$ it remains constant in time. For $p > 0$, projective X-basis measurements cause it grow as $S_{\text{diag}}(t) = S_{\text{diag}}(0)e^{-\lambda t} + S_{\text{diag}}(\infty)(1 - e^{-\lambda t})$ at a rate $\lambda$ proportional to $p$. The inset shows the dependence of the early-time decay rate $\lambda$ on $p$ and $N$, with $\lambda \approx p$, independent of $N$. . . . . . . . . . . . . . . . . . . . . . . . . . . . . . 72

4.7 The steady state tripartite information $I_3$ as a function of measurement probability $p$ and system size $N$. The inset shows a data collapse with the fitted parameters $p_c^X = 0.014(2)$ and $\nu = 1.3(2)$. . . . . . . . . . . . . . . . . . . . . . . . . . . 74

4.8 **(a)** Scaling of the steady-state von Neumann entropy with subsystem size $l$. The transition from volume to area-law occurs at $p_c^X \approx 0.014$. **(b)** The steady-state Rényi-$n$ entropies at criticality as a function of $\ln l$. The straight lines are fits to $S_n^l(p = p_c^X) = \alpha(n) \ln l + \beta(n)$. **(c)** The dependence of the log coefficient $\alpha(n)$ on the Rényi index $n$. The solid line is a fit to the form $\alpha(n) = \alpha(\infty)(1 + 1/n)$, where $\alpha(\infty) \approx 0.34$. . . . . . . . 75

4.9 Extracting the dynamical critical exponent $z = 0.98(4)$ using the entanglement entropy of an ancilla qubit as an order parameter for the transition [72, 85]. The ancilla is maximally entangled with the bulk system at the saturation time $t_0$ determined by the dynamics of $I_3$, and then we continue with the dynamics described in Section 4.1 (acting only on the original spins). In performing the data collapse, we exclude times shortly after $t_0$ because the scaling only occurs after an intermediate timescale. . . . . . . . . . . . . . . . . . . . . . . . . 76

5.1 **(a)** Phase diagram for the measurement-induced transition in 2+1D local random Clifford circuits. For measurement probabilities $p < p_c$ the steady state exhibits volume-law entanglement, while for $p \geq p_c$ the steady state is area-law entangled. The entanglement transition and the purification transition coincide. **(b)** The critical point of a $d$-dimensional circuit appears to be described by bulk exponents from the $(d+1)$D percolation. However, entanglement cluster exponents do not match the percolation surface exponents. . . . . . . . . 82

5.2 We employ a graph-state based simulation algorithm [140], where the data encoding the state consists of a graph $\mathcal{G}$ and a list $\{C_i\}_{i=1}^{L^d}$ of one-qubit Cliffords. The entanglement structure is completely fixed by $\mathcal{G}$. Entanglement clusters can be found by a breadth-first search on $\mathcal{G}$, and are here highlighted in different colors. In general the action of a Clifford gate corresponds to updating $\mathcal{G}$ and the list of one-qubit Cliffords. Here we illustrate the simple case of a CZ gate acting on two qubits whose one-qubit Cliffords commute with CZ; in this case the CZ gate simply toggles an edge between the qubits. . . . . . . 84

5.3 **(a)** The sublattice index determines which sublattice of qubits, denoted by ● or ○, are used as the 'controls' for the Clifford gates in that time step. **(b)** Given a choice of sublattice index, the clock index determines in which direction each Clifford gate acts relative to the control. **(c)** The geometry used to calculate the tripartite information $I_3(A : B : C)$. **(d)** One period of the gate sequence on a $2 \times 2$ lattice with periodic boundary conditions, and time moving in the vertical direction. Different colors label different values of the clock index. **(e)** Unit cell of the underlying lattice structure, obtained by contracting each Clifford gate into a point. . . . . . . . . . . . . . . . . . . . . . . . 87

5.4 The steady-state $I_3$ as a function of $(p - p_c)L^{1/\nu}$, where $p_c \approx 0.312(2)$ and $\nu \approx 0.85(9)$. The inset shows the uncollapsed data. This dataset consists of $5 \times 10^4$ circuit realizations. . . . . . . . 91

5.5 'Nodes and links' picture of percolation. **(a)** An example of percolation in the bulk of a 2D system. Percolating bonds cluster within nodes (black dots) connected by links (thick black lines), forming a 'wire frame'. Average distance between nodes is the correlation length $\xi$. There are also smaller structures on the links (dark red), dead ends (red) and structures unconnected to the frame (orange). Minimal-cut path (blue dotted line) can be deformed to only cut through the links (cuts indicated by transparent blue circles), causing an $O(1)$ contribution to the entropy. **(b)** The same example, but in the presence of the final-time boundary. Every structure touching the edge is promoted to be part of the frame. Minimal-cut path generically starts within a smaller structure of size $O(1)$, having now to traverse through larger and larger chambers in order to reach structures of size $\xi$. **(c)** Percolation in the bulk of a 3D system (showing only nodes and links for simplicity). Minimal-cut membrane can be deformed, contributing $O(1)$ to the entropy per one cell of the frame. **(d)** Flattened minimal-cut membrane, showing all the necessary cuts. Near the edge, the membrane traverses layers of structures of increasingly larger sizes (with approximate common ratio $r$). . . . . . . . . . . . . . . . . . . . . 94

5.6 Dynamics and steady-state behavior of the half-plane entanglement $S(L/2 \times L)$ in the volume-law ($p < p_c$), critical ($p = p_c$), and area-law ($p > p_c$) phases. The left column shows the dynamics for $L = 32$, with $S_t \sim Lt$ for $p < p_c$, $S_t \sim L(1 - a/t)$ for $p = p_c$, and $S_t$ saturating in $\mathcal{O}(1)$ time for $p > p_c$. The right column shows the steady-state scaling, with $S_\infty(L) \sim \mathcal{O}(L^2)$ for $p < p_c$, and $S_\infty(L) \sim \mathcal{O}(L)$ for $p \geq p_c$. We use $p = 0.1$, $p = 0.312$, and $p = 0.4$ for the volume-law, critical, and area-law plots respectively. . . . . . . . . . . . . . . . . . . . . . . . . . . 97

5.7 **(a)** The entropy density of an initially maximally-mixed state after evolving for a time $t = 4L$. The black dashed line shows the function $A(p_c - p)^{2\nu}$ with $A \approx 11.7$, and $p_c$ and $\nu$ determined from finite-size scaling of $I_3$. At these system sizes there is still some finite-size drift in the data, but it seems to be approaching the curve described by $A(p_c - p)^{2\nu}$. **(b)** Purification dynamics at $p = p_c$. The data collapse onto a single curve when plotted in terms of $t/L$, indicating a dynamical critical exponent of $z \approx 1$ [the optimal fitted value is $z = 1.07(4)$]. Non-universal early-time dynamics are excluded from the fit. . . . . . . . . . 100

5.8 Extraction of the anomalous scaling exponents $\eta \approx -0.01(5)$, $\eta_{\|} \approx 0.85(4)$, and $\eta_{\perp} \approx 0.46(8)$, shown in **(a)**, **(b)**, and **(c)** respectively, via data collapse at $p = p_c$ of the mutual information $I_2$ between two ancilla qubits which are entangled at time $t_0$ with two system qubits a distance $L/2$ apart. The different exponents are extracted using different boundary conditions and different values of $t_0$ [see main text]. The insets show the uncollapsed data. The $\eta$ dataset consists of $2.5 \times 10^5$ circuit realizations, while the $\eta_{\|}$ and $\eta_{\perp}$ datasets each consist of $1 \times 10^6$ circuit realizations. . . . . . . . . . . . . . . . . . . . . . . . 103

5.9 Extracting the exponents $\beta$ and $\beta_s$ using the entropy $S_{\text{ancilla}}$ of an ancilla qubit which is maximally entangled with a bulk qubit at a time $t_0$, and then further evolved for a time $t = 2L$. **(a)** The bulk exponent $\beta$ is extracted using $t_0 = 2L$. The black dashed curve shows the function $B(p_c - p)^{\beta}$ where $B \approx 3.2$ and $\beta \approx 0.40(1)$. **(b)** The surface exponent $\beta_s$ is extracted using $t_0 = 0$. There the black dashed curve shows the function $C(p_c - p)^{\beta_s}$ where $C \approx 4.6$ and $\beta_s \approx 0.74(2)$. In both cases, $p_c \approx 0.312$ is fixed by finite-size scaling of $I_3$. This dataset consists of $1 \times 10^4$ circuit realizations. . . . . . . . . . . . . . . . 105

5.10 The average size $\overline{s}$ of all entanglement clusters in the steady-state for **(a)** 1+1D and **(b)** 2+1D Clifford circuits. The insets show log-log plots of this quantity at $p = p_c$, with the behaviour well described by the power law $\overline{s} \sim L^{\gamma_{ec}/\nu}$, where $\gamma_{ec}/\nu = 0.95(1)$ for 1+1D and $\gamma_{ec}/\nu = 1.84(2)$ for 2+1D (power-law fits shown in solid red). . . . . . . . . . . . . . . . . . . . . . . . . 109

5.11 The average size $\overline{s_{\max}}$ of the largest entanglement cluster in the steady state for **(a)** 1+1D and **(b)** 2+1D Clifford circuits. The insets show log-log plots of this quantity at $p = p_c$, with the behavior well described by the power law $\overline{s_{\max}}(p_c)/L^d \sim L^{-\beta_{ec}/\nu}$, where $\beta_{ec}/\nu = -0.009(2)$ for 1+1D and $\beta_{ec}/\nu = 0.00(2)$ for 2+1D (power-law fits shown in solid red). Note there are strong finite-size effects in 2+1D, so there the fit is only to sizes $L \geq 40$. . . . . . . . . . . . . . . . . . . . . . . . . . . . . . 111

5.12 Distribution function $n_s$ of the entanglement cluster sizes $s$ in the $p = p_c$ steady state for **(a)** 1+1D and **(b)** 2+1D Clifford circuits, with system sizes $L = 348$ and $L^2 = 48^2$ respectively. For $1 \ll s \ll L^d$, the probability distribution follows a power-law distribution $n_s \sim s^{-\tau}(c_0 + c_1 s^{-\Omega})$ with the leading-order correction to scaling controlled by the exponent $\Omega$. The dashed and dotted lines show fits using the exponents from $d$- and $(d+1)$-dimensional percolation respectively. The peak at large $s$ corresponds to the percolating cluster of size $O(L^d)$ present for $p \leq p_c$. . . . . . . . . . . . . . . . . . . . . . . . . . . . 112

5.A1 **(a)** The steady-state values of $I_3/L$ as a function of $(p - p_c)L^{1/\nu}$, where $p_c \approx 0.303$ and $\nu \approx 1.07$. The inset shows the uncollapsed data. This dataset consists of 50,000 circuit realizations. **(b)** Analogous to Fig. 5.8a, except performed at the alternative critical point $p_c \approx 0.303$ estimated from the data collapse of $I_3/L$. The main plot shows the 'optimal' collapse at $\eta = -0.57$ as determined by minimizing the cost function in Section 5.B, but this clearly does not produce a good data collapse. . . . . 117

5.B1 **(a)** The logarithm of the cost function $\epsilon$ measuring the quality of the data collapse for different values of $p_c$ and $\nu$, compared between two possible indicators of the entanglement transition: the half-plane entanglement entropy $S(L/2)$, and the tripartite information $I_3$. The black dots show the minimum of the cost function for each indicator. See the appendix for a definition of the cost function $\epsilon$. **(b)** A linear-scale close-up of the cost function for the $I_3$ data collapse around the estimated critical point, which is indicated by the black dot. The white line indicates the boundary of the region for which the cost function is less than 2 times its minimum value; this is the region from which the error bars are calculated. At the estimated critical point the cost function attains the value $\epsilon = 1.47$, close to the optimal value $\epsilon \approx 1$. . . . . . . . . . . . . . . . . . . . . . . . . 118

5.C1 The dynamics of the half-plane von Neumann entropy at the critical point $p_c = 0.312$ of the 2+1D Clifford model. **(a)** The data are not linear on a log scale, indicating that the entanglement growth is *not* logarithmic in time (system size is $L = 92$). **(b)** A plot of $S(t, L/2)/L$ as a function of $1/t$, where the linear trend provides support for the scaling $S(t, L) \sim L(1-a/t)$. **(c)** Scaling collapse of $S(t)-bL$ vs $t/L$, with $b = 0.685$ producing the best fit. . . . . . . . . . . . . . . . . . . . . . . . . . . . . 120

5.D1 The mean cluster size $\overline{s}$ and largest cluster size $s_{\mathrm{max}}/L^d$ for the projective transverse field Ising model in 1+1D (left column) and 2+1D (right column). These should scale as $\overline{s} \sim L^{\gamma_{1,1}/\nu}$ and $s_{\mathrm{max}}/L^d \sim L^{-\beta_s/\nu}$ respectively. The critical exponents are all close to the corresponding surface critical exponents of percolation in $(d+1)$-dimensions, with the exception of the mean cluster size in 2+1D, as we discuss in the main text. . . . 122

5.D2 The mean surface cluster size $\overline{s}$ for the site percolation on a 2D square lattice (left) and a 3D simple cubic lattice (right). Blue line is a fit to $\overline{s} = aL^{\gamma_{1,1}/\nu}$ for the largest system sizes, while the red line includes a constant correction to scaling, $\overline{s} = aL^{\gamma_{1,1}/\nu} + b$. Corresponding estimates of $\gamma_{1,1}/\nu$ are given in the legend. . . . . . . . . . . . . . . . . . . . . . . . . . . . 123

# List of Tables

3.1 Critical properties of the measurement-induced transition in 1+1D quantum circuits, reproduced from Ref. [72]. Here $n$ refers to the Rényi index, and all results for $n = 1, 2, 5, \infty$ are for circuits with Haar-random gates. For stabilizer states the Rényi entropies are independent of $n$: the results for Clifford circuits are given in the column labelled '$C$'. The column labelled '$P$' gives the corresponding results for 2D percolation. $\alpha(n)$ refers to the coefficient of the logarithm controlling the scaling of the entanglement entropy at criticality, $S_n(L) \sim \alpha(n) \log L$. . . . . . 52

5.1 Critical exponents of the measurement-induced transition in hybrid 1+1D and 2+1D random Clifford circuits, compared with those of 1D, 2D and 3D percolation (1D P, 2D P, and 3D P respectively). Exponents which appear to differ from percolation are highlighted in red. Those exponents which describe the scaling of entanglement clusters are labelled by the subscript $ec$, and are compared with the bulk and surface exponents for percolation. The exponents for 1+1D Clifford circuits, excluding those describing entanglement clusters, are taken from Ref. [72]. . . . . . . . . . . . . . . . . . . . . . . . . . 85

# Part I

# Discrete time crystals

# Chapter 1

# Background

The study of phases of matter has traditionally focused on those that can exist in systems at thermal equilibrium. At finite temperature this amounts to studying equivalence classes of thermal states,

$$\rho = \frac{e^{-\beta H}}{\mathrm{tr}\left[e^{-\beta H}\right]}, \tag{1.1}$$

while at zero temperature the focus is on ground states. Precisely how the equivalence relation is defined depends on the systems in question. For gapped phases of matter, a popular choice is equivalence under finite-time evolution of a local Hamiltonian [1].

This focus on thermal equilibrium is not unreasonable, given that a wide variety of many-body systems are seen to converge rapidly to equilibrium. This can happen even in closed systems without coupling to an external heat bath, provided one only insists that the system looks *locally* like a thermal state — this is the content of the eigenstate thermalization hypothesis [2–4].

There is an extraordinary richness in the phases of matter that can be realized in this way, but nonetheless the requirement of thermal equilibrium places some restrictions on the types of order that can exist. For example, the Mermin-Wagner-Hohenberg theorem [5–7] prohibits the spontaneous breaking of continuous symmetries in systems with short-range interactions at finite temperature in spatial dimensions $d \leq 2$, and for different reasons it is also widely believed that topological order cannot exist at finite temperature in $d \leq 2$ [8].

Given these considerations, if it were possible to somehow avoid thermal equilibrium (without fine-tuning), then there could be new *non-equilibrium* phases of matter. Some of these may have equivalent equilibrium phases, but in principle there could also be genuinely new phases that can only be realized out of equilibrium.

Discrete time crystals (DTCs) are significant in being perhaps the prototypical example of a non-equilibrium phase that provably cannot exist in thermal equilibrium. They are characterized by the fact that they spontaneously break discrete time-translation symmetry. Momentarily leaving aside precisely how this is defined, the history of DTCs is instructive in illustrating their role as an exemplar of a non-equilibrium phase.

The idea of a time crystal was first proposed in 2012 by Frank Wilczek [9], who had in mind the continuous time version: the generator of the system dynamics has continuous time-translation symmetry, but the ground state spontaneously breaks this symmetry to some discrete subgroup. More concretely, Wilczek's proposed ground state consisted of a soliton rotating periodically around a ring — the periodic fluctuations of the particle density would break the time-translation symmetry. However, it was quickly pointed out that this was not actually the correct ground state for the model he proposed; in fact, the true ground state had no such rotating soliton, and so did not spontaneously break the time-translation symmetry [10–12]. It was later proved in more generality that spontaneously breaking time-translation symmetry is impossible in the ground state or thermal state of a local Hamiltonian [13–15].

## 1.1 Absence of continuous time-translation symmetry breaking

To explain the absence of continuous time-translation symmetry breaking (TTSB) in thermal equilibrium, let us first fix a precise definition of continuous TTSB. We follow the definition given in Ref. [13]. Suppose we have a collection of local observables $\{A_i\}$, where $i$ labels position, and $A_i$ is supported on an $\mathcal{O}(1)$ region around site $i$. To detect symmetry breaking of the symmetry $\mathcal{G}$, the observables $A_i$ should transform non-trivially under $\mathcal{G}$. We could then define spontaneous symmetry breaking of $\mathcal{G}$ in the state $\rho$ as long-range order in the correlation function

$$\lim_{|i-j|\to\infty} \langle A_i A_j \rangle_\rho \neq 0, \tag{1.2}$$

where as usual $\langle \Phi \rangle_\rho = \mathrm{tr}[\Phi\rho]$.

Equivalently, we can define a macroscopic observable $A$ by

$$A = \frac{1}{V}\sum_i A_i, \tag{1.3}$$

where $V$ is the system volume. As an example, one could take $A_i = \sigma_i^z$ to be the local magnetization, so that $A$ is the net magnetization.

Long-range order in the state $\rho$ could then be defined as the existence of a macroscopic observable $A$ with a nonzero value of the limit

$$\lim_{V\to\infty} \langle AA \rangle_\rho \neq 0. \tag{1.4}$$

To generalize this to spontaneous breaking of continuous time-translation symmetry, we then require that this limit is not only nonzero, but is a non-trivial function of time, i.e.

$$\lim_{V\to\infty} \langle A(t)A \rangle = f(t), \tag{1.5}$$

where $A(t)$ is the time-evolved version of $A$ in the Heisenberg picture.

Let us now prove that this is impossible if the expectation value is taken with respect to a thermal state as in Eq. (1.1). The result we are about to show holds at all temperatures [14], but to show that requires a more complicated proof, so for simplicity we will just focus on states satisfying the following condition on the fast decay of correlations. In $d$ spatial dimensions, this means that we consider states $\rho$ which satisfy

$$\left|\mathrm{tr}\left[\rho A_i B_j\right] - \mathrm{tr}[\rho A_i]\mathrm{tr}\left[\rho B_j\right]\right| \leq \|A_i\|\|B_j\| f(|i-j|), \tag{1.6}$$

where $A_i$ and $B_j$ are local observables supported at sites $i$ and $j$ respectively, and the decay function satisfies $f(r) \in o(r^{-d}/\mathrm{polylog}\, r)$. This assumption is satisfied in thermal states at all finite temperatures in $d = 1$ [16] and above a finite critical temperature in $d > 1$ [17].

Given this assumption, we will show the following theorem, which implies that any possible time-dependence of the expectation value $\mathrm{tr}[\rho A(t)B]$ must vanish in the thermodynamic limit $V \longrightarrow \infty$, thus demonstrating the absence of spontaneous symmetry breaking of the continuous time-translation symmetry of the Hamiltonian.

**Theorem** (Huang [15]). *Let $\rho$ be a stationary state with correlation decay $f(r) \in o(r^{-d}/\mathrm{polylog}\, r)$, and consider the 'macroscopic operators' $A = \frac{1}{V}\sum_i A_i$ and $B = \frac{1}{V}\sum_j B_j$. At any time $t \in \mathbb{R}$,*

$$|\mathrm{tr}[\rho A(t)B] - \mathrm{tr}[\rho A]\mathrm{tr}[\rho B]| \in \mathcal{O}(1/V), \tag{1.7}$$

*where $A(t) = e^{iHt}Ae^{-iHt}$ is the time-evolution of $A$ in the Heisenberg picture. $A$ and $B$ do not have to be translationally invariant, and $H$ does not need to be a local*

*Hamiltonian.*

*Proof.* We assume without loss of generality that $\mathrm{tr}[\rho A_i] = \mathrm{tr}\big[\rho B_j\big] = 0$ for any $i, j$. If not we can simply transform $A_i \to A_i - \mathrm{tr}[\rho A_i]\mathbb{1}$ and similarly for $B_j$.

Let $\{|E_1\rangle, |E_2\rangle, \dots\}$ be a complete set of eigenstates of $H$ with energies satisfying $E_1 \le E_2 \le \cdots$, and let $X_{jk} = \langle E_j|X|E_k\rangle$ be the matrix element of the operator $X$ in this basis. Writing out the matrix elements in Eq. (1.7), we have

$$\begin{aligned}
|\mathrm{tr}[\rho A(t)B]| &= \left|\sum_{jk} \rho_{jj} A_{jk} B_{kj} e^{i(E_j - E_k)t}\right| \le \sum_{jk} \rho_{jj} |A_{jk}||B_{kj}| && (1.8)\\
&\le \sqrt{\sum_{jk} \rho_{jj} |A_{jk}|^2 \times \sum_{j'k'} \rho_{j'j'} |B_{k'j'}|^2} && (1.9)\\
&= \sqrt{\sum_{j} \rho_{jj} (AA^\dagger)_{jj} \times \sum_{j'} \rho_{j'j'} (B^\dagger B)_{j'j'}}\\
&= \sqrt{\mathrm{tr}\big[\rho A A^\dagger\big]\mathrm{tr}\big[\rho B^\dagger B\big]}.
\end{aligned}$$

The first step used the fact that $\rho$ is a steady-state of the Hamiltonian, $[\rho, H] = 0$, so we can choose the energy basis such that $\rho$ is diagonal. The second step is the triangle inequality, and the third step is the Cauchy-Schwarz inequality applied to the inner product $\langle A, B\rangle \equiv \sum_{jk} \rho_{jj} A_{jk} B_{kj}$ defined on the space of Hermitian matrices.

Now, considering the first factor,

$$\mathrm{tr}\big[\rho A A^\dagger\big] = \frac{1}{V^2} \sum_{i,i'} \mathrm{tr}\Big[\rho A_i A_{i'}^\dagger\Big] = \frac{\mathcal{O}(1)}{V^2} \sum_{i,i'} f(|i - i'|) \le \frac{\mathcal{O}(1)}{V} \sum_{i \in \mathbb{Z}^d} f(|i|) = \mathcal{O}\left(\frac{1}{V}\right), \tag{1.10}$$

where we used the fact that the operators $A_i$ have $\mathcal{O}(1)$ norm, and that the fast decay properties of $f(r) \in o(r^{-d}/\mathrm{polylog}(r))$ guarantee that $\sum_{i \in \mathbb{Z}^d} f(|i|)$ converges to $\mathcal{O}(1)$. We finish by noting that $\mathrm{tr}\big[\rho B^\dagger B\big]$ can similarly be upper bounded by $\mathcal{O}(1/V)$. □

More generally, one may wonder why it is impossible to spontaneously break time translation symmetry in equilibrium, given that, for example, it is possible to spontaneously break spatial translation symmetry. The resolution is that, compared with other symmetries, time plays a privileged role in equilibrium statistical mechanics, because the time direction defines what we mean by 'equilibrium'.

## 1.2 Discrete time-translation symmetry breaking

Given the results of the previous section, one might be tempted to conclude that any form of time-translation symmetry breaking (TTSB) is impossible. It turns out, however, that a weaker form of TTSB is possible, provided one moves the focus away from states in thermal equilibrium. Instead of breaking *continuous* time-translation symmetry, it turns out to be possible to spontaneously break *discrete* time-translation symmetry. The most natural scenario in which this occurs is in periodically-driven (Floquet) systems, where the periodic drive imposes a discrete $G = \mathbb{Z}$ symmetry on the system. That symmetry can then be spontaneously broken to some discrete subgroup $H$ — in the simplest case, $H = 2\mathbb{Z}$, i.e. there is *period-doubling*.

### 1.2.1 Definitions of discrete TTSB

We give two definitions of TTSB, both proposed by Else et al. in Ref. [18], which we follow as a reference in this section. Each definition has its own merits, with one providing a direct link with experiment, while the other proves helpful for mathematical analysis. Formally they are equivalent, as we will discuss. They apply to systems which are periodically driven, so their Hamiltonians have a discrete time translation symmetry, i.e. $H(t + T) = H(t)$ for some period $T$. Let $\mathcal{L}_f$, the 'Floquet Liouvillian', denote the generator of time-evolution by one period, i.e. $\rho(t + T) = \exp(\mathcal{L}_f T)\rho(t)$. We define short-range correlated states $\rho$ to be those that satisfy cluster decomposition, i.e. $\left|\mathrm{tr}\left[\rho A_i B_j\right] - \mathrm{tr}[\rho A_i]\mathrm{tr}\left[\rho B_j\right]\right| \to 0$ as $|i-j| \to \infty$. Then, for any infinite system, we can define TTSB as follows.

**Definition** (TTSB-1)**:** TTSB occurs if, for every time $t$ and every short-range entangled state $\rho(t)$, there is an observable $\Phi$ such that

$$\mathrm{tr}[\rho(t+T)\Phi] \neq \mathrm{tr}[\rho(t)\Phi].$$

Physically, this means that in a system which has discrete TTSB, we can drive the system with some frequency $\Omega$ and yet there will be some observables which respond at a frequency different to $\Omega$. Systems which spontaneously break discrete time-translation symmetry are termed 'discrete time crystals' (DTCs).

We can also define TTSB in terms of long-range correlations:

**Definition** (TTSB-2)**:** TTSB occurs if all of the eigenstates of the Floquet operator $\mathcal{L}_f$ are long-range correlated.

This is similar to the definition of conventional SSB, except that instead of symmetry-invariant *equilibrium* states, we consider Floquet eigenstates (which are invariant under the same discrete time-translation symmetry as the Liouvillian).

The definitions TTSB-1 and TTSB-2 focus on different aspects of symmetry breaking, but formally they are equivalent. TTSB-2 implies TTSB-1 because, if all the eigenstates of the Floquet operator $\mathcal{L}_f$ are long-range correlated, to get the short-range correlated states which TTSB-1 applies to, we need to consider superpositions of Floquet eigenstates with different eigenvalues. These short-range correlated states will then not exhibit $T$-periodicity because applying the Floquet operator (which corresponds to time evolution by a time

$T$) will not result in the same state, and hence TTSB-1 is satisfied. Conversely, TTSB-1 implies TTSB-2 because Floquet eigenstates are invariant under time evolution by multiples of $T$ by definition, which means that if TTSB-1 occurs, none of these short-range correlated states can be a Floquet eigenstate, and hence we have TTSB-2.

### 1.2.2 Robustness to perturbations

Now, these definitions of TTSB, though precise, leave out one or two key properties of conventional SSB that we might hope to see replicated in TTSB. In particular, in conventional SSB, we expect the symmetry breaking states to be robust against weak perturbations to the Hamiltonian. In other words, we don't expect SSB to require 'fine-tuning' of the Hamiltonian. For example, if one applies a small perturbation to an atom arranged in a crystal lattice, it will still return to its equilibrium position as long as the perturbation isn't too large.

It turns out that there are some models of TTSB that have this property of robustness [19]. However, let us first explore a simple system that seems to obey these definitions of TTSB, but does not have the desired robustness against perturbations.

Consider a system of qubits, and suppose they are driven by a two-pulse protocol given by

$$H_{\text{non-int}}(t) = \begin{cases} -(1+\epsilon)\dfrac{\pi}{2t_1}\sum_i \sigma_i^x, & 0 \le t \bmod T \le t_1; \\ \Delta \sum_i \sigma_i^z, & t_1 \le t \bmod T \le t_1 + t_2, \end{cases} \tag{1.11}$$

where $T = t_1 + t_2$ is the overall period of the Hamiltonian. For $\epsilon = 0$, the spins will flip over the times $0 \le t \bmod T \le t_1$, and then will remain constant over the times $t_1 \le t \bmod T \le t_1 + t_2$. We can think of $H_{\text{non-int}}(t)$ as having a $\mathbb{Z}$ time-translation symmetry, corresponding to translations by integer multiples of the drive period $T$. On the other hand, any observable of the

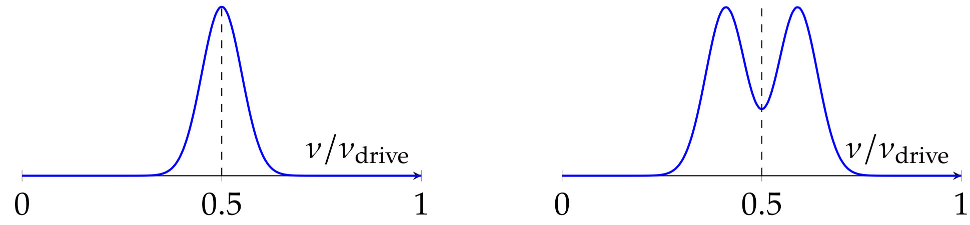

**(a)** $\epsilon = 0$

**(b)** $\epsilon > 0$

**Figure 1.1:** An example of how the subharmonic peak at $\nu = \nu_{\text{drive}}/2$ is not robust against pulse errors for a non-interacting system. This behaviour should appear for many order parameters, but for concreteness one could look at the Fourier spectrum of $\sigma^z$ for one of the spins.

system will not possess this symmetry, because the spins have to be flipped twice to return to their original states. Experimentally, the way one looks for time-translation symmetry breaking is to take some observable, say $\sigma^z$ for one of the spins, and calculate the Fourier spectrum of its expectation value. For $\epsilon = 0$, there is a strong peak at $\nu_{\text{drive}}/2$, as shown in Fig. 1.1a, where $\nu_{\text{drive}} = T^{-1}$ is the drive frequency. In this way, the time-translation symmetry group is spontaneously broken from $\mathbb{Z}$ to $2\mathbb{Z}$.

However, suppose now that, instead of perfectly flipping the spins, there is some pulse error $\epsilon \neq 0$ so that the spins aren't perfectly flipped. For the simple non-interacting Hamiltonian $H_{\text{non-int}}(t)$, any nonzero $\epsilon$ causes beating in the correlation functions of observables[1], which manifests itself in a splitting of the Fourier peak at $\nu = \nu_{\text{drive}}/2$, as shown in Fig. 1.1b. What is non-trivial about time crystals is that the Fourier peak remains pinned at $\nu_{\text{drive}}/2$, even for nonzero pulse error $\epsilon$.

### 1.2.3 The issue of heating

While the move to Floquet systems allows us to avoid the no-go theorems that prevent the possibility of continuous TTSB in equilibrium systems, it brings with it its own challenges. In particular, there is the problem of *heating*. Once we break continuous time-translation symmetry, energy is no longer conserved. The question is then what happens to the system as a result of the energy input from the drive. The answer and possible resolutions depend on whether the system is closed or not.

---

[1] One can get some intuition for this by considering the case of a single qubit governed by the Hamiltonian in Eq. (1.11), and visualizing the motion of the qubit's state on the Bloch sphere. In the absence of fine-tuning, beating occurs due to the combination of oscillations around the $x$- and $z$-axes. The beating disappears when $\epsilon = 0$ because then the spin is aligned along the $z$-axis at all times, and so is unaffected by the rotation around the $z$-axis caused by the $\Delta\sigma^z$ term.

For closed quantum systems, it has been argued that 'generically' — 'generic' here meaning the system obeys the eigenstate thermalization hypothesis — the periodic drive will result in the system heating up to infinite temperature in the steady-state [20], where no symmetry-breaking is possible. Therefore to have a hope of symmetry-breaking, one must have a way of avoiding this heating effect. In a closed system, there are two known ways this can happen without fine-tuning: via many-body localization (MBL), where the system avoids heating up for infinite time, or via pre-thermalization, where the system avoids heating up for an exponentially large time dependent on the drive frequency and the local interactions. Early proposals for discrete time crystals largely focused on closed systems, and so relied on these mechanisms of MBL [18, 21] and pre-thermalization [22].

In open quantum systems, it is well known that the combination of driving and dissipation to a heat bath can result in the system being driven to a non-trivial steady state [23–25]. The focus of this part of the thesis will be on whether this can be utilized to realize discrete time-translation symmetry breaking.

## 1.3 Experimental evidence of a many-body localized time crystal

As explained in Section 1.2.3, many-body localization has been proposed as one possible mechanism by which a closed quantum system can avoid indefinitely heating up when driven, and hence have a chance at displaying time-translation symmetry breaking. An experiment was soon done by the

Monroe group in Maryland aiming to explore this possibility [26]. This experiment used a 1D array of 10 trapped ions, a number small enough that they were able to precisely control the drive applied to each ion. This precision helped them to be confident that they were applying conditions sufficient for many-body localization. The ions they used were $^{171}\mathrm{Yb}^{+}$, and they focused on the effective two-level system generated by the $^{2}\mathrm{S}_{1/2}$ $|F=0, m_F=0\rangle$ and $|F=1, m_F=0\rangle$ hyperfine 'clock' states, which are split by 12.642 831 GHz.

Their drive protocol consisted of three stages, illustrated in Fig. 1.2, which were periodically repeated. The first and second stages correspond to the usual spin-flip and interaction phases that are common in models of DTCs. The third phase consisted of applying local disorder to each ion; this is necessary to produce many-body localization. This drive protocol can be described mathematically by

$$H(t) = \begin{cases} H_1 = g(1-\epsilon)\sum_i \sigma_i^y, & 0 \le t \bmod T < t_1; \\ H_2 = \sum_{ij} J_{ij}\sigma_i^x\sigma_j^x, & t_1 \le t \bmod T < t_1 + t_2; \\ H_3 = \sum_i D_i\sigma_i^x, & t_1 + t_2 \le t \bmod T < t_1 + t_2 + t_3, \end{cases} \tag{1.12}$$

where $T = t_1 + t_2 + t_3$ is the drive period, $g$ is the Rabi frequency such that $gt_1 = \pi/2$, $J_{ij}$ is the spin-spin interaction strength between sites $i$ and $j$, and $D_i$ is a local random field chosen uniformly from the interval $[0, W]$.

One important thing to note is that they were able to control the range of the spin-spin interaction strength $J_{ij}$. More precisely, the spin-spin interactions were generated by spin-dependent optical dipole forces, which resulted in an interaction strength that falls off algebraically as $J_{ij} \propto J_0/|i-j|^{\alpha}$. The exponent $\alpha$ is a controllable parameter which can be tuned from 0 to 3 by varying the laser detuning or the trap frequencies. For their published results, they used $\alpha = 1.5$, which in a 1D spin chain corresponds to a *short-range* interaction, and hence we still expect MBL to persist [27, 28].

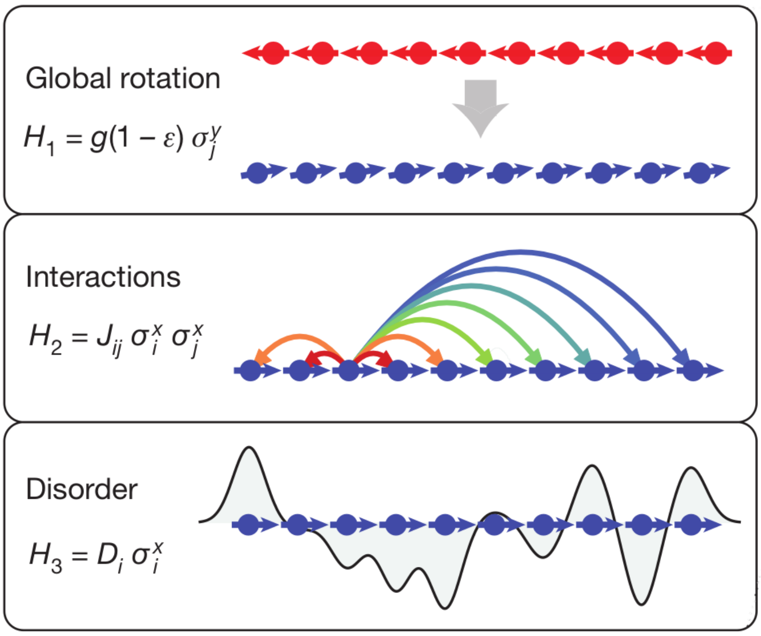
Global rotation
$H_1 = g(1-\varepsilon)\,\sigma_j^y$
Interactions
$H_2 = J_{ij}\,\sigma_i^x\,\sigma_j^x$
Disorder
$H_3 = D_i\,\sigma_i^x$

**Figure 1.2:** An overview of the drive protocol used in the MBL trapped ion experiment. Figure taken from Ref. [26].

In Fig. 1.3 we include a brief overview of their results. Their results match well with theoretical expectations: for weak interactions and no disorder, as shown in Fig. 1.3a, they do not observe a robust subharmonic peak, whereas for strong interactions and strong disorder, as shown in Fig. 1.3c, the peak becomes stable to nonzero rotation errors. Fig. 1.3b shows that disorder (and hence MBL) alone is not sufficient to produce DTC order; in this case it is only the combination of disorder and spin-spin interactions that leads to a stable discrete time crystal.

### 1.3.1 Echoing out the disorder

While the experiment described in the previous section was initially received as one of the first experimental realizations of an MBL discrete time crystal, it was later pointed out that there was an issue with how they had attempted to realize MBL in their Floquet system [29, 30]. Specifically, the disorder required to realize MBL was predominantly present in the local magnetic fields $D_i$. In an undriven system this would be fine, but the problem arises in the intersection with the Floquet drive. The magnetic field term is odd

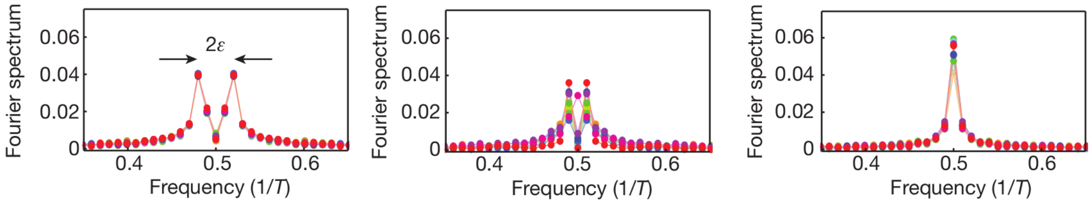

**(a)** $Wt_3 = 0, J_0t_2 = 0$ **(b)** $Wt_3 = \pi, J_0t_2 = 0$ **(c)** $Wt_3 = \pi, J_0t_2 = 0.036$

**Figure 1.3:** An overview of the main results of the experiment with MBL trapped ions in Ref. [26], from which these figures have been adapted. Here $\epsilon$ is the rotation error, $W$ controls the strength of the disorder, and $J_0$ controls the strength of the spin-spin interactions. All figures have a fixed nonzero rotation error of $\epsilon = 0.03$. **(a)** No disorder and no interactions results in a subharmonic peak which is unstable to rotation errors. **(b)** Having disorder but no interactions also does not result in a stable subharmonic peak. **(c)** Only the combination of disorder and interactions results in a stable subharmonic peak.

under the Ising symmetry enacted by the spin-flip phase of the Floquet drive. This means that the protocol effectively enacts a 'spin-echo', such that the magnetic field term is approximately averaged to zero. This removes the dominant disorder from the system, and in the original experiment the residual disorder in the interaction terms $J_{ij}\sigma_i^x\sigma_j^x$ was not sufficient to realize MBL. It was subsequently argued that the DTC order seen in this system was not MBL but rather *prethermal* DTC order, as evidenced by the strong dependence of the long-time dynamics on the initial state.

To realize an MBL DTC in a trapped ion system like this, it is therefore important that the disorder is introduced in a term which is *even* under the Ising symmetry. The obvious candidate is the interaction term $J_{ij}\sigma_i^x\sigma_j^x$, and indeed this has been the focus of a recent experiment [31], which is otherwise quite similar to the experiment previously described.

## Chapter 2

# Dissipative discrete time crystals

While early realizations of discrete time crystals (DTCs) focused on closed quantum systems, it is natural to ask whether it is possible to spontaneously break discrete time-translation symmetry in an open system. This provides a natural route to avoiding the 'heating problem' by coupling to a heat bath, rather than through the mechanisms of many-body localization (MBL) or pre-thermalization that seem necessary for DTCs in closed quantum systems. This is advantageous partly because realizing the conditions for e.g. MBL may be out of reach for many natural physical systems, such as those with long-range interactions [27].

In this chapter, we will discuss an experiment performed at UCL using phosphorous-doped silicon which may provide an example of a dissipative discrete time crystal [32]. There has also been an experiment which observed a DTC in a system of nitrogen-vacancy centres in diamond [33], and an NMR experiment in a spatially *ordered* crystal which obtained similar results [34]. These systems are also not expected to be MBL, but we omit them here for the sake of brevity.

## 2.1 DTCs in phosphorous-doped silicon

The experiment with phosphorous-doped silicon in Ref. [32] was done with silicon isotopically purified to 99.995% $^{28}$Si, which has zero nuclear spin, with the spin-1/2 nuclear spins of the residual $^{29}$Si contributing to dissipation rates. The strongest coherent interaction is between the electronic spins of the phosphorus dopants. These interactions are dipole-dipole interactions, whose strength falls off with their separation $r$ as $r^{-3}$. Hence in 3D these interactions are long-ranged, and there is good evidence to suggest that long-range interactions can lead to the delocalization of a system [27, 28]. In addition, the dissipation due to the residual $^{29}$Si could also delocalize the system [35, 36]. To summarise, this system is not expected to display many-body localization.

As usual, the system was periodically driven, in this case with a two-stage pulse protocol, as outlined in Fig. 2.1. In words, the experimental procedure was roughly as follows. The spins were initially all aligned in the $z$-direction using a large magnetic field of 0.34 T. Then, at the start of the experiment, a $\pi/2$-pulse was applied to rotate the spins into the $x$-$y$ plane. With the spins initialized, a sequence of $N$ Floquet unitaries was applied, each consisting of two pulses. The first was a long 'spin-locking' pulse which enabled the spins to interact with each other. Then a global rotation of the spins by an angle $\phi = (1+\epsilon)\pi$ was performed using a protocol known as 'BB1' in the NMR literature [37]. It consists of a simple $\phi$ rotation pulse, followed by a $\pi(\theta) - 2\pi(3\theta) - \pi(\theta)$ series of corrective pulses, where the phase of the rotation pulse $\pi(\theta)$ is $\theta = \arccos(-\phi/4\pi)$. The purpose of this protocol is to enable extremely spatially uniform rotations, which is important given that the DTC protocol involves monitoring the effect of deliberating introducing some error $\epsilon$ into the spin rotation. Without the corrective pulse, the spatial variation is $\sim 10\%$ across the sample due to variations in the microwave frequency magnetic field generated by the split ring cavity used for driving and detection. Finally, after the sequence of Floquet unitaries, the spins were rotated back to the $z$-plane with another $\pi/2$-pulse, after which they were read out using a Hahn echo.

It is important to note here that the direct interaction *strength* is in some sense

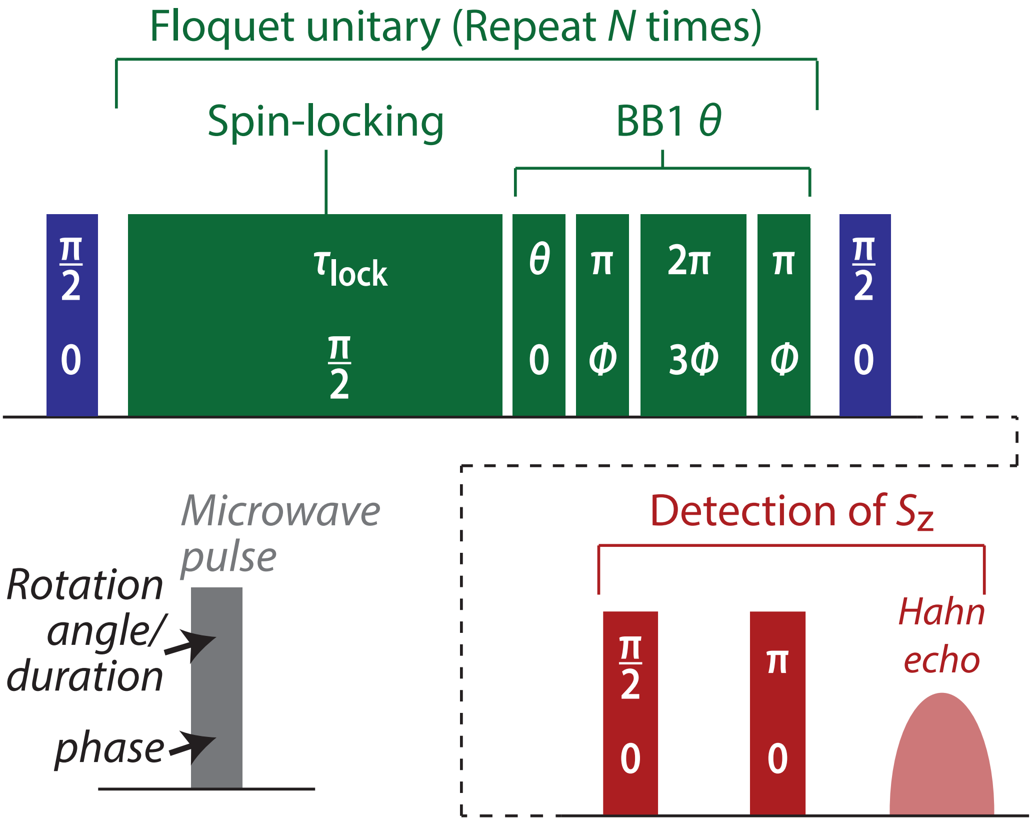
Floquet unitary (Repeat N times)
Spin-locking
BB1 θ
π/2
0
τlock
π/2
θ
0
π
Φ
2π
3Φ
π
Φ
π/2
0
Microwave pulse
Rotation angle/duration
phase
Detection of Sz
π/2
0
π
0
Hahn echo

**Figure 2.1:** An overview of the pulse protocol for the experiment with phosphorous-doped silicon outlined in Ref. [32], from which this figure is adapted. The main part of the drive protocol, outlined in dashed lines, consists of two stages: a 'spin-locking' stage where the spins are free to interact, and a $\pi$-pulse, where the spins are flipped using the BB1 protocol to ensure spatially uniform rotations.

fixed at the point of sample production, since the interaction strength depends only on the distance between spins, and hence the density of phosphorous dopants, which is fixed for a given sample.

There was disorder in this system, which resulted from two sources. The spin-spin interaction strength depends on the distance between the spins, and this varies from spin to spin (it can be controlled by varying the density of phosphorous dopant spins). There was also a magnetic field applied to the sample, and the linewidth in this field resulted in disorder in the local field experienced by each spin.

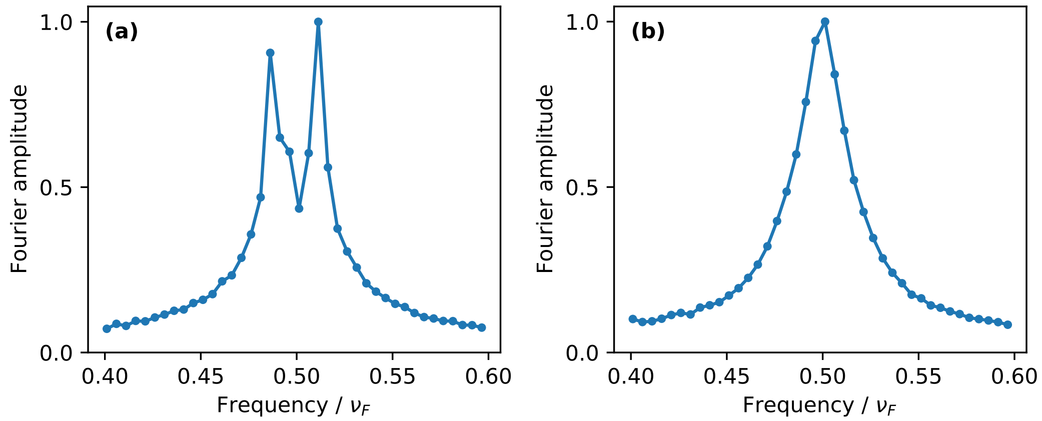

**Figure 2.2:** Experimental data showing a comparison between the normalized Fourier spectra for the trivial phase **(a)** and the DTC phase **(b)**, for a fixed rotation error of $\epsilon = 0.01$. Whereas the subharmonic peak splits for any nonzero $\epsilon$ in the trivial phase, in the DTC phase the subharmonic peak is fixed at $\nu_F/2$ for small but nonzero $\epsilon$. The DTC phase corresponds to $\tau_{\text{lock}} = 100\tau_{\text{flip}}$, while the trivial phase corresponds to $\tau_{\text{lock}} = 10\tau_{\text{flip}}$.

## 2.2 Experimental observations

The main observable in the experiment was the net magnetization, which can be read out using a Hahn echo sequence. The magnetization is monitored stroboscopically at the end of every Floquet period, up to $n = 200$ periods. The resulting time series is then Fourier-transformed, and we monitor for the presence of a robust subharmonic peak at half the drive frequency $\nu_F$. Increasing the duration $\tau_{\text{lock}}$ of the spin-locking pulse lengthens the Floquet period and hence reduces the Floquet frequency $\nu_F$. Since the axes in the phase diagrams are measured in units of $\nu_F$, this allows us to explore regions of the phase diagram with effectively stronger interactions and dephasing.

Fig. 2.2 shows some experimental data comparing the resulting Fourier spectra between the trivial and DTC phases. In both plots the rotation error is fixed at $\epsilon = 0.01$. For the trivial phase, this results in the subharmonic peak immediately splitting, as a result of beating induced by the imperfect spin-flip. However, in the DTC phase the subharmonic peak is robust against imperfections in the Floquet drive, and as a result remains unsplit for small but nonzero $\epsilon$, indicating the robustness of the discrete time-translation

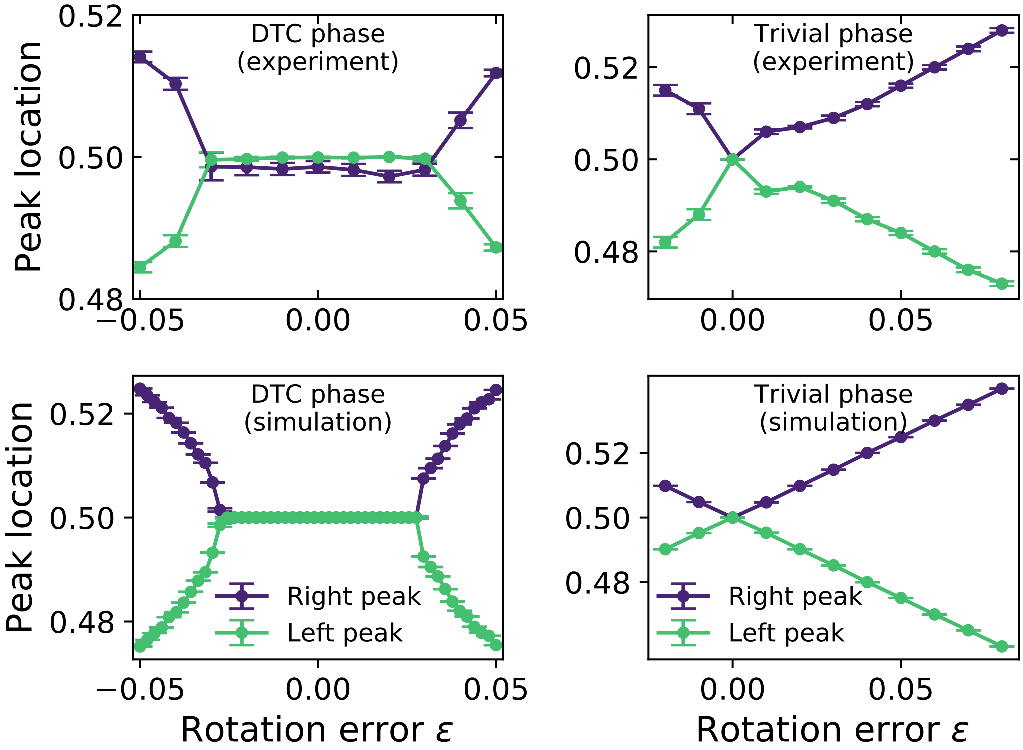

**Figure 2.3:** A comparison between experiment and theory of the splitting of the subharmonic Fourier peak as a function of the rotation error $\epsilon$. Whereas in the DTC phase the subharmonic peak remains fixed at half the Floquet frequency in a finite window around $\epsilon = 0$, in the trivial phase it splits immediately for any $\epsilon \neq 0$. The DTC phase corresponds to $\tau_{\text{lock}} = 100\tau_{\text{flip}}$, while the trivial phase corresponds to $\tau_{\text{lock}} = 10\tau_{\text{flip}}$. The asymmetry of the trivial phase data around $\epsilon = 0$ is discussed in the main text.

symmetry breaking.

To experimentally probe the phase boundary, we sweep the rotation error $\epsilon$, and monitor the positions of the 'left' and 'right' peaks around $\nu_F/2$. In the DTC phase, both of these peaks will be fixed at $\nu_F/2$, but once we enter the trivial phase the peaks will move apart with increasing $\epsilon$. Fig. 2.3 shows a comparison between experiment and theory (see Section 2.3.1) of the predicted phase boundary as a function of $\epsilon$ in both the DTC and trivial phases. As predicted, in the DTC phase the left and right peaks in the Fourier spectrum remain fixed at $\nu_F/2$ for a finite window of $\epsilon$ before eventually splitting at sufficiently large $\epsilon$, i.e. for a sufficiently large perturbation. On the other hand, in the trivial phase the peaks immediately move apart for any nonzero $\epsilon$. One might notice that for the trivial phase data, the collected data is not symmetric around $\epsilon = 0$. This is not a physical effect, but rather is a reflection of the fact that during the experiment collecting this data, there was some variation in the duration of the rotation pulse required for a perfect spin-flip, and as a result data was effectively only collected in the interval $\epsilon \in [-0.02, 0.08]$. This could possibly be due to small variations in the pulse amplifier power output. At any rate, the splitting effect for nonzero $\epsilon$ in the trivial phase remains clear.

## 2.3 Theoretical model

Discrete time crystals can be characterized by their robust subharmonic response to a periodic drive. Intuitively, the dissipation can cancel out any small perturbations to the state or the drive which might otherwise break the subharmonic response. What is more non-trivial is whether this dissipation-stabilized subharmonic response can persist in the presence of destabilizing interactions. In this section we map out the phase diagram of a discrete time crystal (DTC) with competing dissipation and interactions, and numerically show that a dissipation-driven DTC is indeed stable to weak interactions. Further, we explore the opposite regime, where strong interactions stabilize the DTC, and show that this regime is stable to weak dissipation.

In the experiment outlined in Sections 2.1 and 2.2, we explore the strong dissipation/weak interaction regime of this phase diagram, and find that our observations align with the theoretically predicted phase boundary (see Figs. 2.3 and 2.4a). At the other extreme, the weak dissipation/strong interaction regime could be probed by looking at samples with higher concentrations of phosphorus dopants.

To map out the phase diagram of the dissipative DTC as a function of dissipation strength and interaction strength, we use two different probes — they agree in their predictions for the DTC phase boundary. First, we use the experimentally-relevant probe of calculating the dynamics of local observables and whether or not they exhibit stable subharmonic peaks in their Fourier spectra (Fig. 2.4a). Second, we look at the $\pi$-gap of the Floquet Liouvillian (Fig. 2.4b), which we define in Section 2.3.2. The $\pi$-gap was first introduced in Ref. [38] to study emergent symmetries in many-body localized DTCs, but here we generalize it to Liouvillian systems.

### 2.3.1 Description of the model

To produce the phase diagram, we focus on the driven central spin model (CSM) coupled to a dissipative bath. The CSM has been successful as a semiclassical effective model for describing decoherence in solid state systems [39–47]. In the experiment described in Sections 2.1 and 2.2, the strongest coherent interaction is between the electronic spins of the phosphorus dopants, which form the spins in the CSM. However, in the dephasing-dominated regime relevant to this experiment, we do not expect the spatial interaction structure to be important, and view the infinite-range central spin model as an approximation to the long-range dipolar interactions of the phosphorus spins. This theoretical approximation has been validated for describing the decoherence of donor spins in experiments [48–51]. Finally, nuclear spins from residual $^{29}$Si contribute to dissipation rates, and provide a small source of random field for the electron spins.

To have a notion of *competing* interactions and dephasing, we use $\sigma^y\sigma^y$ interactions and $\sigma^z$ dephasing, which in principle should produce DTC-like phenomena in $\sigma^y$ and $\sigma^z$ respectively. Interestingly, in the weakly interacting case, we find that strong $\sigma^z$ dephasing can also stabilize a DTC-like response in $\sigma^y$.

The Hamiltonian of the central spin model with $\sigma^y\sigma^y$ interactions is given by

$$H_{\mathrm{CSM}} = \sum_{i=1}^{N} J_{0i}\sigma_0^y\sigma_i^y + \sum_{j=0}^{N} h_j\sigma_j^z, \tag{2.1}$$

where the central spin has index 0, and the outer spins have indices 1 to $N$. $J_{0i}$ and $h_j$ are modelled as random variables taken from the uniform distributions over $[-h, h]$ and $[-J_y, J_y]$ respectively. To incorporate the driving, the Hamiltonian follows a two-stage protocol given by

$$H(t) = \begin{cases} H_{\mathrm{CSM}}, & \text{for time } \tau_{\mathrm{lock}}; \\ (1+\epsilon)\dfrac{\pi}{2\tau_{\mathrm{flip}}}\displaystyle\sum_{i=0}^{N} \sigma_i^x, & \text{for time } \tau_{\mathrm{flip}}. \end{cases} \tag{2.2}$$

For $\epsilon = 0$, the second stage of the pulse protocol exactly flips the spins. The discrete time crystal phase can be defined operationally by its robustness against nonzero rotation errors $\epsilon$.

In addition to the interactions present within the central spin model, we model the effects of external dephasing using the Lindblad master equation given by

$$\frac{\mathrm{d}\rho}{\mathrm{d}t} = -i[H(t), \rho] + \kappa_1 \sum_{i=0}^{N} \left( \sigma_i^z \rho \sigma_i^{z\dagger} - \frac{1}{2}\left\{ \sigma_i^{z\dagger} \sigma_i^z, \rho \right\} \right). \tag{2.3}$$

Note that this dissipation model enacts XY-dephasing, i.e. it draws the state of a single qubit to the $z$-axis of the Bloch sphere. This can be seen as being in competition with the $\sigma^y \sigma^y$ interactions present within the central spin model [Eq. (2.1)].

In the experiment, $T_{1\rho}$ was measured to be 193 µs for the higher density sample, giving $\kappa_1 \sim 2.3\,\mathrm{kHz}$, while $J$ and $h$ can be estimated from the phosphorus concentration and are of the order 300 Hz and 10 Hz respectively. Hence we expect XY-dephasing to dominate the dynamics of the experimental system.

## 2.3.2 Order parameters for the DTC phase diagram

### 2.3.2.1 Fourier spectra of local observables

In an experiment, a DTC is typically detected by measuring the time-dependence of local observables (or averages thereof), and looking for oscillations at an integer fraction $1/n$ of the drive frequency $\nu_F$ which are robust against perturbations. This robustness can be detected by looking at the Fourier spectra of these local observables; the DTC phase will have a strong peak at $\nu_F/n$ which remains unsplit for a finite window of rotation errors. To use this to produce a phase diagram, we fix a nonzero rotation error $\epsilon$, and then for each set of parameters calculate the Fourier spectrum of $\langle\sigma_0^z\rangle$ in the driven-dissipative central spin model (see Section 2.3.1), assign a value of +1 if the peak is split and 0 if not, and average the result over 10 disorder realizations.

In the strong dephasing limit, both the central and the outer spins exhibit robust period-doubling. The same is also true in the strong interactions limit, where interestingly the outer spins have Fourier spectra which split for *larger* values of $\epsilon$ than the central spin.

### 2.3.2.2 $\pi$-gap

Consider a periodically-driven, or 'Floquet', system. If its dynamics are unitary, then time-evolution at integer multiples of the drive period $T$ can be generated using the *Floquet unitary* $U_F = \mathcal{T}\exp(-i\int_0^T H(t)\mathrm{d}t/\hbar) \equiv \exp(-iH_F T/\hbar)$, where $\mathcal{T}$ denotes time-ordering, and $H_F$ is an effective *Floquet Hamiltonian*. If instead its dynamics are non-unitary, we can make an analogous statement: time-evolution at integer multiples of the drive period $T$ can be generated using the exponential of the *Floquet Liouvillian* $\exp(\mathcal{L}_F T) \equiv \mathcal{T}\exp(\int_0^T \mathcal{L}(t)\mathrm{d}t)$, where $\mathcal{L}(t)$ is the Liouvillian at time $t$.

One can analyze the stroboscopic dynamics of the system by looking at the spectrum of the Floquet Liouvillian $\mathcal{L}_F$. The imaginary part of the spectrum describes the oscillatory modes, while the real part describes the decay modes.

In the $\mathbb{Z}_2$ DTC phase, *$\pi$-pairing* occurs, where the eigenvalues come in pairs with imaginary parts separated by $\pi$. Provided the initial state has significant overlap with these $\pi$-paired states, the subsequent dynamics will exhibit period doubling. The $\pi$-gap $\Delta_\pi$ provides a measure of the extent of $\pi$-pairing across the spectrum of $\mathcal{L}_F$, and is defined as

$$\Delta_\pi = \mathbb{E}\big[\big|\mathrm{Im}\big(\lambda_{i+\mathcal{N}/2} - \lambda_i\big) - \pi\big|\big]. \tag{2.4}$$

Here the $\lambda_i$ are the eigenvalues of $\mathcal{L}_F$, ordered according to their imaginary parts, $\mathcal{N}$ is the total number of eigenvalues, and the average $\mathbb{E}$ is taken uniformly across the spectrum of $\mathcal{L}_F$. For an order parameter, we look at $\Delta_\pi/\Delta_0$, where $\Delta_0 = \mathbb{E}[|\mathrm{Im}(\lambda_{i+1} - \lambda_i)|]$ is the mean nearest-neighbour spacing, which provides a relevant scale to compare against. The $\mathbb{Z}_2$ DTC phase corresponds to $\Delta_\pi/\Delta_0 \ll 1$.

### 2.3.3 Analysis of the phase diagram

The $\pi$-gap has the advantage that it can probe the DTC transition for arbitrary observables. For our purposes, this means we can simultaneously analyze DTCs with i) strong dissipation and weak interactions, and ii) weak dissipation and strong interactions. Fig. 2.4b shows that there are two clear transitions which occur: one at weak interactions upon increasing the dephasing strength, and one at weak dephasing upon increasing the interaction strength. Further, the positions of these transitions are stable against finite interactions or dissipation respectively.

The experiment described in Section 2.2 probes the dephasing-driven DTC transition. The detail to Fig. 2.4a shows experimental Fourier spectra for experiments with $\tau_{\mathrm{lock}} = 10t_\pi$ and $\tau_{\mathrm{lock}} = 100t_\pi$. Increasing $\tau_{\mathrm{lock}}$ lengthens the Floquet period and hence reduces the Floquet frequency $\nu_F$. Since the axes in the phase diagrams are measured in units of $\nu_F$, this allows us to explore regions of the phase diagram with effectively stronger interactions and dephasing. These experimental Fourier spectra thus probe either side of

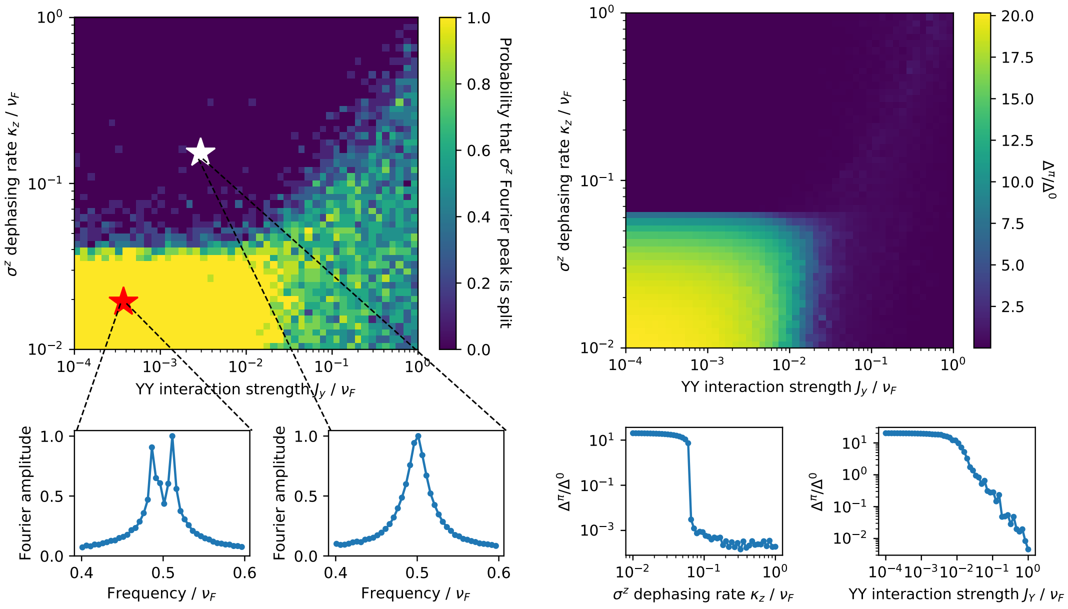

**(a)** **(b)**

**Figure 2.4:** Phase diagram of the discrete time crystal with competing dissipation and interactions, using two different order parameters. Fig. 2.4a includes experimental data exploring the strong dissipation/weak interaction phase boundary. **(a)** Phase diagram from the Fourier spectrum of $\langle \sigma_0^z \rangle$, calculating using the driven central spin model coupled to a dissipative bath. The DTC phase corresponds to the dark region, where $\langle \sigma_0^z \rangle$ has a stable peak at half the drive frequency. Unlike the $\pi$-gap phase diagram, there is no dark region in the bottom right because we are looking at $\sigma^z$; in this region $\sigma^y$ exhibits period doubling instead. The red and white stars and corresponding Fourier spectra correspond to experiments with $\tau_{\text{lock}} = 10t_\pi$ and $\tau_{\text{lock}} = 100t_\pi$ respectively. **(b)** $\pi$-gap phase diagram of the discrete time crystal as a function of dephasing rate and $\sigma_i^y \sigma_j^y$ interaction strength. The DTC phase corresponds to $\Delta_\pi/\Delta_0 \ll 1$ (dark regions). The two plots at the bottom are slices through the phase diagram, the left at weak interactions and the right at weak dissipation. Both slices show a clear transition in the $\pi$-gap, though this is more pronounced for the dissipation-driven transition. **Parameters:** $\epsilon = 0.01$, $h = 10\,\text{Hz}$, $N = 5$, 10 disorder realizations; Fourier transforms calculated over $0 \le n \le 200$ Floquet periods. Phase diagram axes are in units of the Floquet frequency $\nu_F$.

the dissipative DTC phase boundary, and demonstrate that the dissipative DTC is stable in the predicted region, even with potentially destabilizing interactions.

## 2.4 Comment on the crystalline fraction as a probe for DTC order

When observing a discrete time crystal (DTC) in an experiment, one of its characteristic features is the robustness of the subharmonic peak in its Fourier spectrum against perturbations. In the simplest case where the symmetry is broken from $\mathbb{Z} \to 2\mathbb{Z}$, this manifests itself in a robust peak in the Fourier spectrum at half the drive frequency $\nu_F$. The crystalline fraction was introduced in Ref. [33], one of the first experimental reports of DTC order, as an easy measure to probe for the presence of DTC order. It is defined in terms of the Fourier transform $S(\nu)$ as

$$f = \frac{|S(\nu = \nu_F/2)|^2}{\sum_\nu |S(\nu)|^2}, \tag{2.5}$$

giving the fraction of the Fourier amplitude localized at the subharmonic peak. The idea is that one introduces a deliberate error $\epsilon$ into the spin-flip phase of the Floquet drive, and then measures the $\epsilon$-dependence of the crystalline fraction $f$. Ref. [33] argued that in the DTC phase there would be a 'plateau' feature in the plot of $f$ vs $\epsilon$, where in some finite window of $\epsilon$ centred around zero, the crystalline fraction would be approximately constant, thereby giving some indication of robustness. An example of this plateau feature is shown in Fig. 2.5.

The crystalline fraction is clearly an attractive tool, given the ease with which it can be calculated in an experiment. However, although a true DTC would indeed likely give rise to a 'plateau', it is important to distinguish this from other possible causes. In this vein, we give experimental and numerical evidence that it is possible that *spatial inhomogeneities* in the spin-flip applied to spins across the sample can also result in a plateau, even in systems we do not expect to be in the DTC phase. Such spatial inhomogeneity can be quite common in experimental platforms, and can be non-negligible — in

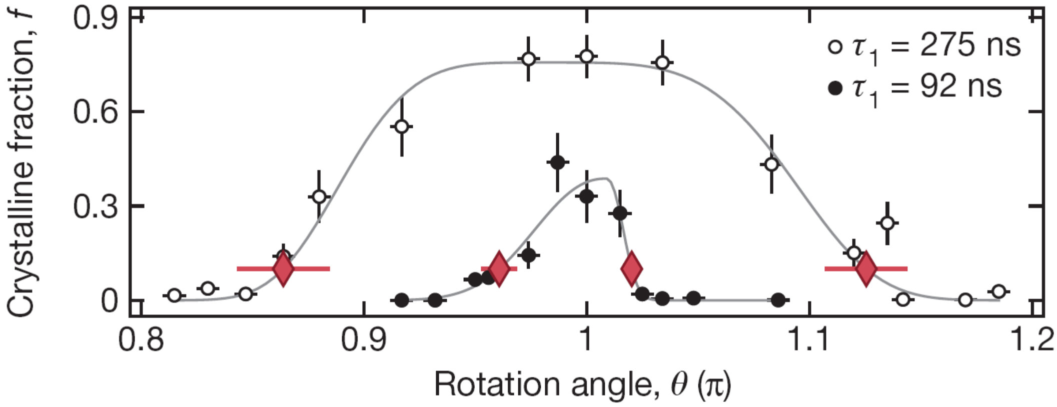

**Figure 2.5:** The dependence of the crystalline fraction $f$ on the rotation angle $\theta = (1 + \epsilon)\pi$ in an experiment aiming to observe DTC order in a system of NV centres in black diamond [33]. Here $\epsilon = 0$ corresponds to a perfect spin-flip. The claim is that the data with the longer interaction time $\tau_1 = 275\,\text{ns}$ corresponds to the DTC phase, as evidenced by the 'plateau' dependence of $f$ on the rotation angle near $\theta = \pi$. The red diamonds are a rough indication of the phase boundary.

the experiment described here, without correction the spatial variation in the rotation angle is ∼ 10% across the sample due to variations in the microwave frequency magnetic field used for driving and detection. This is certainly a large effect, given that even in the DTC phase the subharmonic response can break down at around 5% rotation error (see Fig. 2.3).

In Fig. 2.6a is data from the experiment on phosphorous-doped silicon described in Section 2.1. There the presence of spatial inhomogeneity in the rotation pulse can be largely corrected for by using the BB1 protocol. The data with BB1 shows the crystalline fraction decaying smoothly as the rotation error increases, indicating we are in the trivial phase. However, if we remove BB1, thereby reintroducing spatial inhomogeneity, we find that the crystalline fraction is roughly constant over a wide range of rotation error. We note in passing that the subharmonic oscillations of the Floquet cycles without BB1 also decayed much faster than the oscillations with BB1. A longer duration for the rotation pulse of 300ns in the BB1 data vs 200ns for the non-BB1 data, causing more dephasing and weaker signal, may account for the lower overall crystalline fraction of the BB1 experiment.

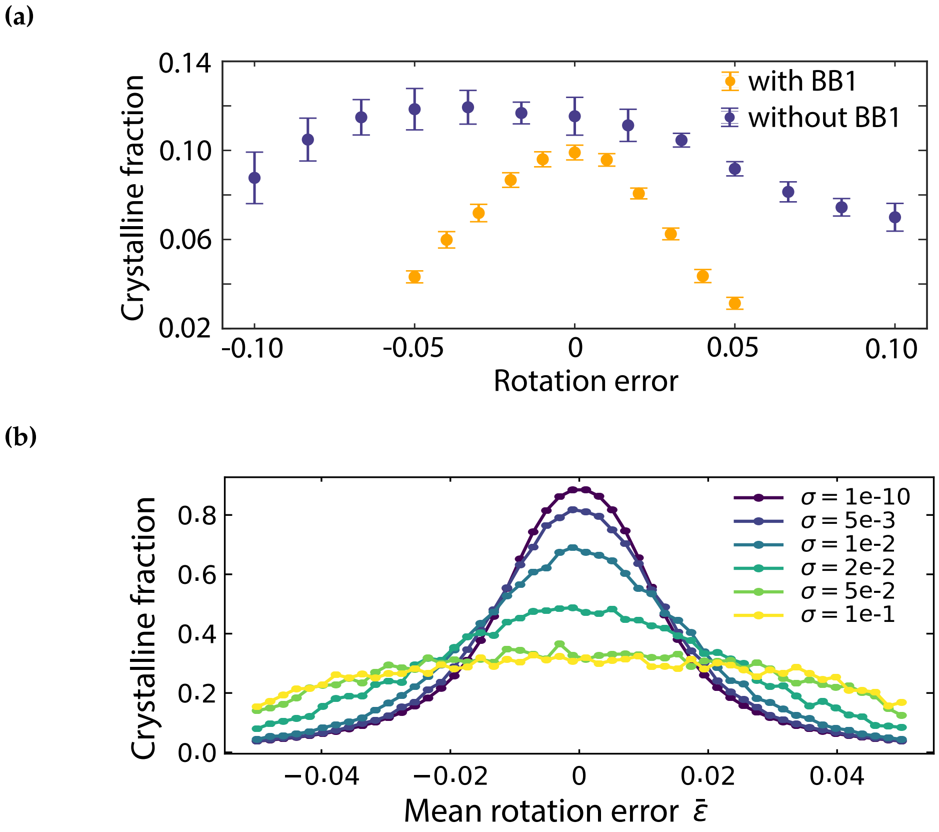

**Figure 2.6:** The effect of nonuniform rotations on the crystalline fraction. **(a)** Comparison of the crystalline fraction against rotation error of the same sample with and without BB1 pulses turned on. The non-BB1 pulse sequence appears to have a flattened peak, while the BB1 crystalline fraction has no indication of a plateau. **(b)** Simulations of the crystalline fraction using the driven-dissipative central spin model using nonuniform rotation pulses. For a given disorder realization, the rotation error $\epsilon$ is drawn from a Gaussian distribution with mean $\bar{\epsilon}$ and variance $\sigma^2$, clipped at 10% to model the finite extent of the sample. We observe that large values of $\sigma$ result in a distinct flattening of the crystalline fraction curve, consistent with our experimental observations in Fig. 2.6a.

To support this analysis, in Fig. 2.6b we show numerical simulations of the driven-dissipative central spin model, where the rotation error applied to each spin is drawn individually from a Gaussian distribution. For a given mean rotation angle $\bar{\epsilon}$, we vary the variance $\sigma^2$ of the distribution to vary the amount of spatial inhomogeneity. The maximum deviation from the mean is fixed at 10% to model the finite extent of the sample. As the data for $\sigma = 10^{-10}$ shows, we are using dissipation and interaction parameters that put us in the trivial phase, where for spatially homogeneous rotations the crystalline fraction decays smoothly with the rotation error. However, upon increasing the rotation variance, we observe a flattening of the crystalline fraction curve, consistent with the experimental observations in Fig. 2.6a. This provides an example of where spatial inomogeneity can produce a spurious 'plateau' signature in the crystalline fraction, which should therefore not be taken as a definitive indication of DTC order.

## 2.5 Conclusion

In this chapter we have discussed the results of an experiment in a driven system of phosphorous-doped silicon in which signatures of discrete time crystalline order were observed. Since dissipation was strong in this system, we modelled it with a driven-dissipative central spin model, and found good agreement between experiment and theory, particularly in the location of the phase boundary. This provides an example where dissipation may play a key role in stabilizing DTC order. We also studied the $\pi$-gap, a spectral measure of the pairing of eigenstates, and found a transition in the $\pi$-gap that coincided with the DTC transition, providing a similarity with MBL time crystals. In the future it would be interesting to further explore the novel possibilities for phases of matter in non-equilibrium systems, of which discrete time crystals are but an early example. It is not yet clear to what extent one could aim for a classification of these phases in the same vein as the current program in classifying topological phases of matter. One direction could be to develop a notion of how non-equilibrium phases are 'equivalent', such as by generalizing quasiadiabatic continuation [52] to non-unitary systems. For local systems this will likely also involve some version of a Lieb-Robinson bound applicable to non-unitary time evolution [17].

# Part II

# Measurement-induced phase transitions

## Chapter 3

# Background

## 3.1 Entanglement scaling

Given a pure quantum state $|\psi\rangle$, the von Neumann entanglement entropy $S_A$ of a subsystem $A$ is defined as $S_A = -\mathrm{tr}\left[\rho_A \log \rho_A\right]$, where $\rho_A = \mathrm{Tr}_{A^c}[|\psi\rangle\langle\psi|]$ is the reduced density matrix of $A$. One can also consider a slightly generalized quantity, the $n$-Rényi entropy

$$S_{n,A} = \frac{1}{1-n} \log \mathrm{tr}\left[\rho_A^n\right], \tag{3.1}$$

where $n \in [0, \infty]$. This is a whole family of entropies, which recovers the von Neumann entropy in the limit $n \to 1$. For the rest of this section, I will mostly refer to the von Neumann entropy as 'the entanglement entropy', and will not write the Rényi index $n$ unless specified otherwise.

In many-body quantum physics, we are often interested in the behaviour of various quantities in the limit of many degrees of freedom, dubbed the 'thermodynamic limit'. In this limit, the entanglement entropy often exhibits a *scaling* form. One possibility is a *volume-law*, where to leading order $S_A \propto |A| + \cdots$ is proportional to the number of degrees of freedom $|A|$ in $A$. Another possibility is an *area-law*, where $S_A \propto |\partial A| + \cdots$ is proportional to the number of degrees of freedom $|\partial A|$ in the boundary of $A$.

These scaling forms occur naturally in various scenarios. For example, a volume-law is ‘typical’, in the sense that a random pure state has volume-law entanglement with probability one in the thermodynamic limit [53]. Volume-laws also emerge in the steady-state of different types of quantum dynamics, including chaotic dynamics, such as in random quantum circuits or chaotic Hamiltonian time evolution [4], as well as time evolution by many-body localized (MBL) Hamiltonians [54–58]. The origin of the volume-law is quite different in these two classes of dynamics: for the chaotic systems it is a consequence of local thermalization, where in the steady-state local reduced density matrices are close to thermal states at an effective temperature $T_{\text{eff}}$ set by the energy density, a statement known as the eigenstate thermalization hypothesis [3] ($T_{\text{eff}} = \infty$ for systems without energy conservation). In MBL systems the steady-state is non-thermal, but nonetheless has a volume-law for a large class of initial states as a result of dephasing between the emergent local integrals of motion present in the MBL phase.

On the other hand, area-laws occur in the ground states of gapped Hamiltonians, a statement proved in 1D [59] and conjectured to hold in higher dimensions (see e.g. [60]). In as much as many of the ordered phases studied by physicists are controlled by these gapped ground states, the subspace of area-law states is sometimes referred to as the ‘physical corner of Hilbert space’. This identification has been particularly fruitful in 1D, where area-law states can be efficiently classically parameterized by matrix product states with constant bond dimension (strictly speaking, the requirement is for an area-law in the ($n < 1$)-Rényi entropies—an area-law in the von Neumann entropy is not sufficient [61]). This has lead to highly effective classical variational algorithms for finding the ground states of 1D gapped Hamiltonians [62].

There are other possibilities for the scaling of entanglement than volume- or area-laws. For example, in 2D conformal field theories (CFTs) the entanglement entropy scales logarithmically, $S_A \propto \log |A| + \cdots$ [63]. This is relevant for continuous phase transitions in 1+1D quantum systems, where the critical point often exhibits conformal symmetry. This logarithm is special to two dimensions—higher dimensional CFTs are expected to obey an area-law to leading order [63, 64].

## 3.2 Entanglement phase transitions

An entanglement phase transition is a type of phase transition at which the qualitative scaling behaviour of the entanglement entropy changes. This should really be understood as a new class of phase transition, distinct from more familiar classes such as thermal phase transitions, 'quantum' phase transitions (i.e. ground state phase transitions), or dynamical phase transitions [65].

Entanglement phase transitions are a relatively recent addition to the cadre of phase transitions. Probably the most well known example is the many-body localization (MBL) transition (though it is not always discussed in these terms). This is a transition at which the eigenstate thermalization hypothesis (ETH) breaks down. In the simplest case, the transition occurs as a function of a 'disorder strength' parameter, such as the variance of a random on-site magnetic field in a Hamiltonian. On the weak-disorder, 'ergodic', side, the energy eigenstates have volume-law entanglement, consistent with the volume-law of thermal states as dictated by the ETH. However, on the strong-disorder side of the transition, the energy eigenstates are only area-law entangled. This can be seen as a consequence of the locality of the emergent integrals of motion which characterize the MBL phase [57]. Thus the MBL transition can be seen as an entanglement transition in terms of the entanglement of energy eigenstates.

## 3.3 Measurement-induced transitions

In this report we will be concerned with a novel mechanism for driving entanglement phase transitions, namely quantum *measurements*. As a minimal model, first consider a local random unitary circuit. Starting from a local product state, the random unitaries will create entanglement locally, causing the overall entanglement of some extensive region to grow linearly in time before saturating to a volume-law. We now imagine modifying this unitary circuit by randomly introducing quantum measurements in between the layers of unitary gates. In the simplest case we can take these measurements to be single-site projective measurements in some fixed basis, and for each site to have a probability $p$ of being measured at each timestep. This will create a competition—the unitaries generate entanglement (locally), while the measurements destroy entanglement (potentially non-locally).

As a result of this competition, what scaling behaviour should the steady-state entanglement have? We can understand the limits fairly easily. At $p = 0$ we recover the random unitary circuit, which results in volume-law entanglement in the steady state. At $p = 1$ every spin is being measured at every timestep, so the steady-state will be some trivial product state with zero entanglement. Hence there should be some sort of transition between volume- and area-law entanglement as a function of $p$. What is interesting is that this transition turns out to be sharp, in the sense that it is a continuous phase transition at which scaling laws and universality emerge. Part of the work in this report will be focused on trying to understand this universality.

Although I have introduced this concept by reference to random unitary circuits [66–86], it is worth noting that these measurement-induced transitions occur in a wide variety of models, including Hamiltonian systems [87–95], and measurement-only models [78, 96–98]. In the spirit of universality, many of these models may fall into the same universality class, despite the differences in their underlying dynamics. However, that is not to say that *all* of these models are in the same universality class—there appear to be some differences in e.g. certain critical exponents for some models. We will explore this issue further in Sec ().

## 3.4 Transitions in the Rényi entropies

One can also ask about the transition for different Rényi entropies. Do they all transition at the same critical measurement probability $p_c$, or can $p_c$ be different for different Rényi entropies? This is relevant for implications about classical simulability, where in 1D an area-law in the $(n < 1)$-Rényi entropies guarantees an efficient representation of the state in terms of constant bond dimension matrix product states.

One can significantly constrain answers to this question by using a few basic properties of the Rényi entropies. For example, by differentiating with respect to $n$ the formula in Eq. (3.1) for the $n$-Rényi entropy, one can show that

$$\frac{\mathrm{d}S_{n,A}}{\mathrm{d}n} = \frac{-1}{(1-n)^2} D(\sigma \parallel \lambda), \tag{3.2}$$

where $D(\sigma \parallel \lambda) = \sum_i \sigma_i \log(\sigma_i/\lambda_i)$ is the relative entropy, taken between the probability distributions $\lambda = \{\lambda_i\}$, given by the eigenvalues of $\rho_A$, and $\sigma = \{\lambda_i^n / \sum_j \lambda_j^n\}$. As a consequence of the non-negativity of the relative entropy, this implies that

$$\frac{\mathrm{d}S_{n,A}}{\mathrm{d}n} \leq 0. \tag{3.3}$$

In other words, the $n$-Rényi entropies are *non-increasing* as a function of $n$. In terms of the measurement-induced transition, this has the consequence that an area-law in the $n$-Rényi entropy implies an area-law in the $(m > n)$-Rényi entropies, and a volume-law in the $n$-Rényi entropy implies a volume-law in the $(m < n)$-Rényi entropies. Note however that we *don't* necessarily have the converse, which would imply that $p_c$ is equal for all Rényi entropies.

However, we *do* have the converse for $m, n > 1$. This is a consequence of the following inequality, valid only for $n > 1$,

$$S_\infty \leq S_n \leq \frac{n}{n-1} S_\infty, \tag{3.4}$$

which implies that all the $(n > 1)$-Rényi entropies must have the same scaling behaviours. This inequality can be proven by using monotonicity of the Rényi entropies and the fact that $S_{\infty,A}$ is simply the largest eigenvalue of $\rho_A$.

## 3.5 Analytically tractable limits

To definitively determine the universality class of a phase transition, it is useful to be able to treat it analytically. For measurement-induced transitions, such treatments are currently available only in a few limits. In this section we will describe two approaches for the measurement-induced transition where the underyling unitary dynamics are generated by Haar-random local unitaries. One applies only to the $(n = 0)$-Rényi entropy, while the other applies to all the $(n \geq 1)$-Rényi entropies but requires a limit of large local Hilbert space dimension. Both reveal an interesting connection to percolation.

### 3.5.1 Transition in the $(n = 0)$-Rényi entropy

The $(n = 0)$-Rényi entropy $S_0$ is equal to the logarithm of the number of nonzero eigenvalues of the density matrix. This means that it might be considered unphysical, since it can change discontinuously under arbitrarily small perturbations to the density matrix. Nonetheless, it admits a particularly simple treatment in terms of the 'minimal cut' formalism. This formalism was initially developed to provide a 'coarse-grained' picture for entanglement growth in local random unitary circuits (viewed as effective minimal models for chaotic quantum dynamics).

To illustrate this approach, consider first a 1+1D local random unitary circuit. Suppose we wanted to calculate the entanglement entropy of a contiguous subsystem $A$ at time $t$. One can think of the random circuit as a tensor network, which needs to be contracted to calculate the final state of the

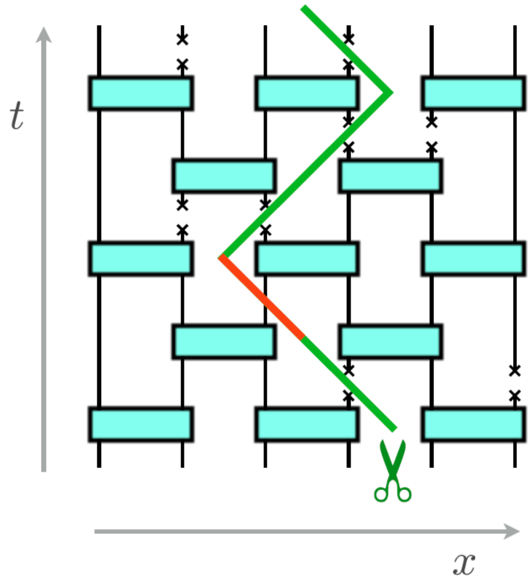

**Figure 3.1:** A schematic of the minimal cut formalism for calculating the ($n = 0$)-Rényi entropy. Figure taken from Ref. [68].

system. The minimal cut prescription involves drawing a line through the spacetime bulk of the quantum circuit which connects the two endpoints of the region $A$. The 'cost' $S_{\text{cut}}$ of this cut is defined as the number of legs of the tensor network which are crossed by the cut. The 'minimal' cut is then the one with the lowest cost. This cut is a useful quantity to consider because it gives a partition of the circuit tensor network into two halves, call them $L$ and $R$, which can then be used to perform a Schmidt decomposition of the overall quantum state,

$$|\psi\rangle = \sum_{i=1}^{q^{S_{\text{cut}}}} \sqrt{\lambda_i}|\mu_i\rangle_L|\nu_i\rangle_R \tag{3.5}$$

where the Schmidt rank (i.e. number of terms in the sum) of this decomposition is given by the cost $S_{\text{cut}}$ of the cut and the local Hilbert space dimension $q$. One of these halves will correspond to subsystem $A$ by virtue of the fact that the cut connected the endpoints of $A$. Since the eigenvalues of the reduced density matrix $\rho_A$ are determined by the Schmidt coefficients, and the ($n = 0$)-Rényi entropy $S_0$ simply counts the logarithm of the number of nonzero eigenvalues, we have the upper bound

$$S_0 \leq S_{\text{cut}}, \tag{3.6}$$

provided we use the convention that logs are measured base $q$. This bound is valid for any cut connecting the endpoints of $A$, but the minimal cut will provide the tightest bound. In fact, owing to the monotonicity of the Rényi entropies, this inequality is valid for all Rényi entropies,

$$S_n \leq S_{\text{cut}}. \tag{3.7}$$

This inequality is useful in itself, but the minimal cut formalism becomes particularly powerful in certain limits where it *exactly* gives the entanglement entropy, rather than just an upper bound. This reduces the calculation of entanglement to a geometric optimization problem (readers familiar with holography will notice the similarity with the Ryu-Takayanagi formula for the entanglement of a boundary region in terms of a 'minimal' surface through the bulk). It is shown in Ref. [86] that, in the case of Haar-random unitaries, the ($n = 0$)-Rényi entropy is given exactly by the minimal cut prescription with probability one—it is this limit we will consider.

Although this formalism was originally developed for solely unitary circuits, projective measurements are easy to incorporate. Since a projective measurement collapses a spin to a single basis state, we no longer have to contract over the leg of the tensor network where the measurement occurred. This means that this leg becomes 'free', and doesn't contribute to the cost of the cut. In other words, measurements can be modelled by picturing them as 'cutting' legs of the tensor network.

It should now be clear where the connection to percolation comes from. Starting from a dense lattice of links corresponding to legs of unitary gates,

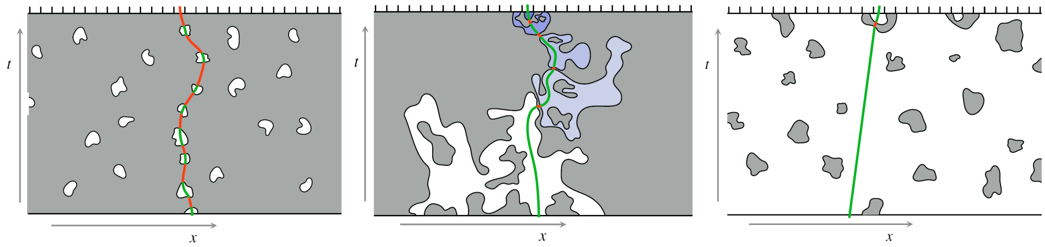

**(a)** Volume-law ($p < p_c$). **(b)** Criticality ($p = p_c$). **(c)** Area-law ($p > p_c$).

**Figure 3.2:** Schematics for the calculation of the ($n = 0$)-Rényi entropy in the minimal cut formalism. The various entanglement phases correspond to different phases of classical percolation in the spacetime bulk of the quantum circuit, where measurements cut a fraction $p$ of the links. Figure taken from Ref. [68].

projective measurements randomly remove a fraction $p$ of these links. The minimal cut then has to percolate through the spacetime bulk of the circuit between the two endpoints of the region for which we want to calculate the entanglement. The volume-law phase corresponds to the percolating phase of the links, since the minimal cut has to cut through some extensive number of links (see Fig. 3.2a), whereas the area-law phase corresponds to the non-percolating phase of the links, where the minimal cut can traverse through the spacetime bulk at $\mathcal{O}(1)$ cost (see Fig. 3.2c). At criticality, owing to the scale-invariant distribution of clusters, to reach the infinite percolating cluster in the bulk from the boundary the cut has to traverse through a series of clusters whose size progressively increase by some $\mathcal{O}(1)$ factor, culminating in $S_0(L) \sim \log L$ scaling in 1D (see Fig. 3.2b).

This logarithmic entanglement scaling at criticality is reminiscent of the behaviour of conformal field theories in 2D. This is to be expected, since the mapping outlined above indicates that the entanglement transition in the ($n = 0$)-Rényi entropy in Haar-random circuits is in the universality class of 2D percolation, which indeed has conformal symmetry at the critical point. The critical measurement probability $p_c = 1/2$ is fixed by this mapping as the critical probability for bond percolation on a 2D square lattice. Numerics also confirm critical exponents consistent with this universality class, such as

$\nu = 4/3$ for the exponent controlling the correlation length $\xi \sim |p - p_c|^{-\nu}$.

One nice feature of the minimal cut formalism is that it readily extends to higher dimensions, suggesting here that in $d$ spatial dimensions, the entanglement transition in the $(n = 0)$-Rényi entropy in Haar-random circuits is in the universality class of $(d + 1)$-dimensional percolation, with the time coordinate of the quantum circuit providing the additional spatial coordinate in the percolation model.

### 3.5.2 Transition in the $(n \geq 1)$-Rényi entropies

The minimal cut formalism outlined in the previous section gave an intuitive physical picture for the entanglement transition in the $(n = 0)$-Rényi entropy in terms of classical percolation. However, it turns out that this simple picture does not describe the *generic* transition, e.g. in the other Rényi entropies, or in circuit models with unitaries drawn from a different distribution than the Haar measure. An easy way to see this is to note that numerics demonstrate that the critical measurement probability $p_c$ seems to be different for the $(n > 0)$-Rényi entropies compared with the value $p_c = 1/2$ for the $(n = 0)$-Rényi entropy. For example, in 1D Haar-random circuits $p_c \approx 0.16$ for the generic transition, with a similar value for 1D random Clifford circuits (in both cases the numerics are on qubits). This value appears to be approximately independent of $n$, provided $n > 0$.

This begs the question of whether it is possible to determine the universality class of the transition in the $(n > 0)$-Rényi entropies. The approach outlined in this section will provide some answers to this question for the $(n \geq 1)$-Rényi entropies, but only in the limit of large local Hilbert space dimension $q \to \infty$. The calculation is more complex than in the previous section, so I will only outline a skeleton of the argument, and will highlight some of its key implications. For more details, see Ref. [75].

We are interested in calculating the $n$-Rényi entropy $S_{n,A}(|\psi\rangle)$ of a region $A$ in the steady state $|\psi\rangle$ of the quantum circuit. The starting point is to note that $S_{n,A}(|\psi\rangle)$ can be expressed using the 'swap-trick' as

$$S_{n,A}(|\psi\rangle) = \frac{1}{1-n} \log \operatorname{tr}\left[(|\psi\rangle\langle\psi|)^{\otimes n} \mathcal{S}_{n,A}\right], \tag{3.8}$$

where the 'swap operator' $\mathcal{S}_{n,A}$ is defined as

$$\mathcal{S}_{n,A} = \prod_x \chi_{g_x}, \qquad g_x = \begin{cases} (12\dots n), & x \in A, \\ \text{identity} = e, & x \in A^c. \end{cases} \tag{3.9}$$

The permutation $g_x$ depends on the site $x$, and is given by the cyclic permutation $(12\dots n)$ if $x$ is in the region $A$, and is given by the identity $e$ otherwise. $\chi_{g_x} = \sum_{[i]} |i_{g_x(1)} i_{g_x(2)} \cdots i_{g_x(n)}\rangle\langle i_1 i_2 \cdots i_n|$ is the representation of $g_x$ on the $n$-fold replicated Hilbert space. Strictly speaking this is a swap only for $n = 2$, where $(12) \circ (12) = e$.

To proceed further we need to perform an average over circuit realizations $C$, given by

$$\overline{S_{n,A}} = \mathbb{E}_C\left( S_{n,A}\left[\frac{C|\psi_0\rangle}{\| \, C|\psi_0\rangle \, \|}\right] \times \operatorname{tr}\left[C|\psi_0\rangle\langle\psi_0|C^\dagger\right]\right). \tag{3.10}$$

The normalization factor $\| \, C|\psi_0\rangle \, \|$ is necessary because the circuit operator $C$ is generically non-unitary due to the presence of measurements (note that we average over measurement outcomes *after* calculating the entanglement entropy, so along a given 'quantum trajectory' the state remains pure). The factor of $\operatorname{tr}\left[C|\psi_0\rangle\langle\psi_0|C^\dagger\right]$ indicates that we are weighting each quantum trajectory by its probability according to the Born rule. In the language of disordered physics, this is a *quenched* average.

Using the swap trick to evaluate the Rényi entropy inside the average, we get

$$\begin{aligned}
\overline{S_{n,A}} &= \frac{1}{1-n}\mathbb{E}_C\left[\log\left(\frac{\mathrm{tr}\big[(C|\psi_0\rangle\langle\psi_0|C^\dagger)^{\otimes n}\mathcal{S}_{n,A}\big]}{\mathrm{tr}\big[(C|\psi_0\rangle\langle\psi_0|C^\dagger)^{\otimes n}\big]}\right)\times\mathrm{tr}\big[C|\psi_0\rangle\langle\psi_0|C^\dagger\big]\right],\\
&= \lim_{m\to 0}\frac{1}{m(1-n)}\mathbb{E}_C\left[\left(\left(\mathrm{tr}\left[\left(C|\psi_0\rangle\langle\psi_0|C^\dagger\right)^{\otimes n}\mathcal{S}_{n,A}\right]\right)^m\right.\right.\\
&\qquad\left.\left.-\left(\mathrm{tr}\left[\left(C|\psi_0\rangle\langle\psi_0|C^\dagger\right)^{\otimes n}\right]\right)^m\right)\times\mathrm{tr}\big[C|\psi_0\rangle\langle\psi_0|C^\dagger\big]\right],\\
&= \lim_{m\to 0}\frac{1}{m(1-n)}\mathbb{E}_C\left[\mathrm{tr}\left[\left(C|\psi_0\rangle\langle\psi_0|C^\dagger\right)^{\otimes nm+1}\left(\mathcal{S}_{n,A}^{\otimes m}-\mathbb{1}\right)\right]\right],
\end{aligned}$$

where in the second line we introduced a replica index $m$ to handle the logarithm using $\log x = \lim_{m\to 0}(x^m-1)/m$. In a sense the swap trick treats the Rényi index $n$ as another replica index, and here the combination of these two uses of the replica trick culminates in the overall replica index $Q = nm+1$, with the replica limit $m \to 0$ corresponding to $Q \to 1$. If we had not included the weighting by the Born rule probability then the replica limit would instead be $Q \to 0$, which is the relevant case for a closely related entanglement transition in random tensor networks [99].

We can gain some physical intuition for this formula by defining the partition functions

$$Z_A = \mathbb{E}_C\left(\mathrm{tr}\left[\left(C|\psi_0\rangle\langle\psi_0|C^\dagger\right)^{\otimes Q}\mathcal{S}_{n,A}^{\otimes m}\right]\right), \tag{3.11}$$

$$Z_\emptyset = \mathbb{E}_C\left(\mathrm{tr}\left[\left(C|\psi_0\rangle\langle\psi_0|C^\dagger\right)^{\otimes Q}\right]\right), \tag{3.12}$$

which correspond to fixing different boundary conditions: $Z_\emptyset$ corresponds to the identity permutation along the whole boundary, whereas $Z_A$ replaces the identity with the cyclic permutation in the region $A$.

Using the fact that $Z_A = Z_\emptyset = 1$ in the replica limit $m \to 0$, we can write the expression for the entanglement entropy as a difference of free energies,

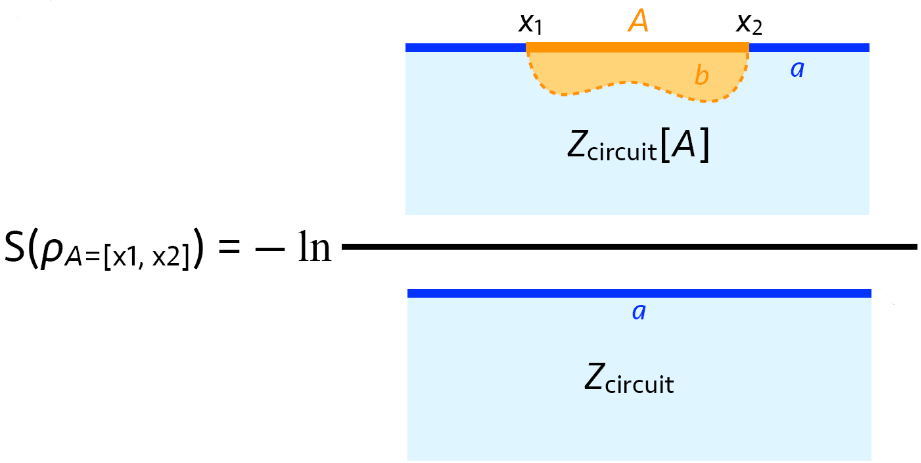

**Figure 3.3:** The entanglement entropy is given by the free energy cost of inserting a domain wall connecting the endpoints of the entanglement region $A$. Figure taken from Ref. [100].

$$\overline{S_{n,A}} = \lim_{m\to 0} \frac{F_A - F_\emptyset}{m(n-1)}, \tag{3.13}$$

where $F_A = -\log Z_A$ and $F_\emptyset = -\log Z_\emptyset$. This free energy difference gives the cost of inserting the domain wall associated with changing the boundary conditions in the entanglement region $A$. Thus we have recovered a similar physical interpretation to the minimal cut formalism: the entanglement entropy corresponds to the free energy cost of a domain wall connecting the endpoints of $A$ through the bulk of a statistical model in $d+1$ dimensions.

Let us note that from Eq. (3.11) one can see that the emergent statistical mechanical model has the symmetry group $G = (S_Q \times S_Q) \ltimes \mathbb{Z}_2$, where the two factors of $S_Q$ represent permutations of the $Q$ replica copies of $C$ and $C^\dagger$ respectively, and the factor of $\mathbb{Z}_2$ represents swapping $C^{\otimes Q}$ and $C^{\dagger \otimes Q}$. The semidirect product structure is a reflection of the fact that the $\mathbb{Z}_2$ action does not commute with the $S_Q \times S_Q$ action. This symmetry group will be relevant when discussing connections with percolation in the limit of infinite local Hilbert space dimension $q \to \infty$.

Now, to calculate the free energy cost of the 'entanglement domain wall' we need to evaluate the ensemble average $\mathbb{E}_C\left[C^{\otimes Q} \otimes C^{\dagger \otimes Q}\right]$ in the replica limit $Q \to 1$. It is here that the limit of large local Hilbert space dimension will prove useful. Averaging over circuit realizations $C$ involves averaging over both unitary gates and measurement Kraus operators. If the unitaries are drawn from the Haar distribution, then there is sufficient structure to calculate these averages exactly. More specifically, *Schur-Weyl duality* allows one to connect properties of the unitary group to properties of the permutation group. In practical terms, this means that the Haar-average over $Q$ copies of a unitary $U$ and its conjugate $U^\dagger$ can be written (using graphical notation borrowed from Ref. [75]) as

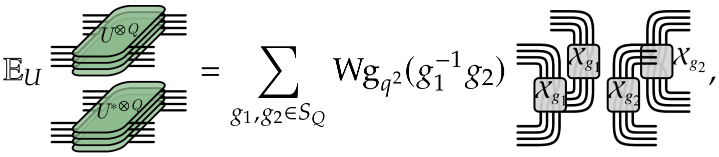

$$\mathbb{E}_U \;\cdots\; = \sum_{g_1, g_2 \in S_Q} \mathrm{Wg}_{q^2}(g_1^{-1} g_2) \;\cdots\;, \qquad (3.14)$$

where $S_Q$ is the permutation group on $Q$ elements, $q$ is the local Hilbert space dimension, $\chi_{g_i}$ is the representation of the group element $g_i$ defined previously, and $\mathrm{Wg}_{q^2}$ is known as the *Weingarten function*. A similar average can also be performed over suitably simple ensembles of Kraus operators representing different measurement outcomes.

Performing averages over both the unitary gates and the measurement outcomes thus converts the quantum circuit into a tensor network which, when contracted, gives the Boltzmann weight for a particular configuration of a statistical mechanical model. In general these weights can be *negative*. This is not necessarily a problem—rather, it is a reflection of the fact that the statistical mechanical model does not obey *reflection positivity*. This is a condition which, roughly speaking, guarantees the unitarity of the quantum field theory resulting from 'Wick-rotating' the statistical mechanical model. But in general this does not need to be satisfied, and indeed there are well-known examples of statistical mechanical models which do not display reflection positivity, such as percolation or models with quenched disorder.

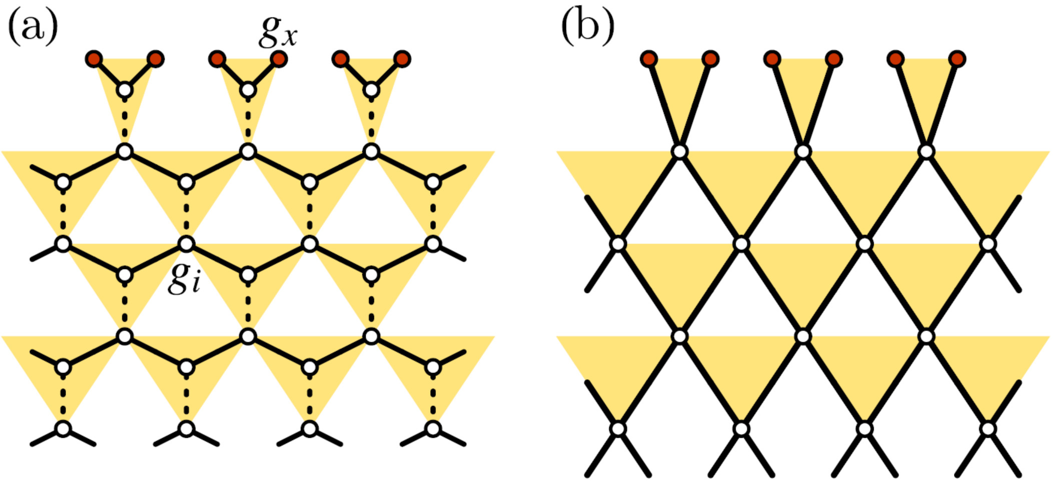

**Figure 3.4:** **(a)** Geometry of the statistical mechanical model arising from averaging over the unitary gates and the measurement outcomes. The circles correspond to 'spins' which take values in the permutation group $S_Q$. The values of the spins highlighted in red at the top are fixed by the boundary conditions (either the cyclic permutation for $Z_A$ or the identity for $Z_\emptyset$). **(b)** In the limit of infinite local Hilbert space dimension $q \to \infty$ the model reduces to a $Q$!-state Potts model on a square lattice. Figure taken from Ref. [75].

We can take this as a signal that, if there is a conformal field theory (CFT) describing the critical point, it should be *non-unitary*. This can also be seen another way. Recall that the central charge $c$ of a CFT provides a measure of how the free energy changes when a finite scale is introduced. In this case, since the partition function $Z_A$ corresponding to the insertion of a domain wall (thus providing a length scale $\sim |A|$) tends to 1 in the replica limit, same as the case $Z_\emptyset$ without a domain wall, we conclude that we should have $c = 0$. It can be shown that the only unitary CFT with $c = 0$ is the trivial CFT containing only the vacuum state, so if there is a non-trivial CFT describing the critical point then it should be non-unitary. Non-unitary CFTs with $c = 0$ are also called *logarithmic* CFTs, which reflects the fact that they may have logarithmic corrections to correlation functions which would otherwise scale purely algebraically in a normal CFT.

Let us now return to the details of the statistical mechanical model describing this entanglement transition. Averaging over the unitary gates and measurement outcomes results in a lattice model of 'spins' which take values in the permutation group $S_Q$ (see Fig. 3.4a). It turns out that the partition function $Z_A$ corresponding to the insertion of a domain wall can be written in terms of a sum over 'triangle weights' $J_p$ as

$$Z_A = \sum_{\{g_i \in S_Q\}} \prod_{\langle ijk \rangle \in \triangledown} J_p(g_i, g_j; g_k), \tag{3.15}$$

where each triangle $\triangledown$ refers to a triangle in the lattice shown in Fig. 3.4a, and the subscript $p$ in $J_p$ indicates that the weight depends on the measurement probability $p$. Strictly in the limit of infinite local Hilbert space dimension $q \to \infty$, this weight is given by

$$J_p(g_i, g_j; g_k) = \Big[(1-p)\delta_{g_i^{-1} g_k} + p\Big]\Big[(1-p)\delta_{g_j^{-1} g_k} + p\Big], \tag{3.16}$$

where we notice that the weight factorizes into two weights defined separately on the links $\langle ik \rangle$ and $\langle jk \rangle$. Treating each group element $g_i \in S_Q$ as a separate colour, this is precisely the weight for a $Q!$-colour Potts model, where the measurement probability $p$ controls the interaction strength. By tuning $p$, the stat mech model undergoes a phase transition from an ordered phase (small $p$) to a disordered phase (large $p$).

The link to percolation then comes from taking the replica limit $Q \to 1$. Since $1! = 1$, we can use the fact that the $n$-state Potts model maps to percolation in the limit $n \to 1$ to make the connection. This demonstrates that the entanglement transition in the ($n \geq 1$)-Rényi entropies is in the 2D percolation universality class in the limit of infinite local Hilbert space dimension $q \to \infty$.

Interestingly however, it turns out that the finite $q$ case is expected to be in a different universality class to percolation. The $q = \infty$ case enjoyed an artificially large symmetry: since the symmetry group of the $n$-state Potts model is $S_n$, our model had a $S_{Q!}$ symmetry group, which is much larger than the $S_Q \times S_Q$ symmetry of the model at finite $q$. One can examine the effect of this explicit breaking of symmetry at finite $q$ by a field-theoretic approach. In a renormalization group flow, typically all possible terms that are compatible with the symmetry of the problem will appear after renormalization. It turns out that the reduced symmetry of the finite $q$ model allows for an extra term (the 'two-hull' operator of the Potts model) in the field theory which is *relevant* at the percolation fixed point. This induces an RG flow away from percolation to some new, currently unknown, fixed point. This demonstrates that we should expect the entanglement transition in the ($n \geq 1$)-Rényi entropies to be in a different universality class from percolation in the case of finite local Hilbert space dimension—which is of course the case relevant to experiments and to numerics. It remains a key current challenge to determine what this new universality class should be.

## 3.6 Numerical studies of universality

Almost all numerical studies of the entanglement transition have been performed on qubits, for obvious reasons of computational tractability. Given the result of the previous section, one would expect the universality class on qubits ($q = 2$) to be different from percolation. Puzzingly, however, numerics on 1+1D systems suggest critical exponents which are remarkably close to those of 2D percolation, despite this being as far away as possible from the $q = \infty$ case where the link to percolation should occur!

Ref. [72] is a helpful reference on this point. They study two models: one where the unitary gates are drawn uniformly over the whole two-qubit unitary group U(4), and the other where they are drawn uniformly over the two-qubit Clifford group. The former corresponds to the model described in the previous section which is most easily treated analytically, while the choice of Clifford gates is useful in studying finite-size scaling because their efficient classical simulability allows for the simulation of much larger systems than

| $n$ | 1 | 2 | 5 | $\infty$ | $C$ | $P$ |
|---|---|---|---|---|---|---|
| $p_c$ | 0.168(5) | 0.162(3) | 0.168(4) | 0.170(4) | 0.154(4) | 0.5 |
| $\nu$ | 1.2(2) | 1.3(1) | 1.4(1) | 1.4(1) | 1.24(7) | 1.33 |
| $\eta$ | 0.19(1) | 0.25(1) | 0.26(1) | 0.26(1) | 0.22(1) | 0.21 |
| $\eta_{\|\|}$ | 0.39(1) | 0.49(1) | 0.49(2) | 0.49(2) | 0.63(1) | 0.67 |
| $\eta_{\perp}$ | 0.23(2) | 0.31(2) | 0.34(1) | 0.34(1) | 0.43(2) | 0.44 |
| $\alpha(n)$ | 1.7(2) | 1.2(2) | 0.9(1) | 0.7(1) | 1.61(3) | 0.55 |

**Table 3.1:** Critical properties of the measurement-induced transition in 1+1D quantum circuits, reproduced from Ref. [72]. Here $n$ refers to the Rényi index, and all results for $n = 1, 2, 5, \infty$ are for circuits with Haar-random gates. For stabilizer states the Rényi entropies are independent of $n$: the results for Clifford circuits are given in the column labelled '$C$'. The column labelled '$P$' gives the corresponding results for 2D percolation. $\alpha(n)$ refers to the coefficient of the logarithm controlling the scaling of the entanglement entropy at criticality, $S_n(L) \sim \alpha(n) \log L$.

the Haar-random case. Clifford dynamics are still sufficiently chaotic to generate volume-law steady-state entanglement, so they provide a somewhat reasonable stand-in for the full unitary group. The critical measurement probability is very close between the two cases: $p_c \approx 0.17$ for Haar-random gates, and $p_c \approx 0.16$ is slightly less for Clifford gates, reflecting the fact that Clifford gates are slightly less chaotic than Haar-random gates. It is not *a priori* obvious though whether this difference in gate set is reflected in the universal properties—the value of $p_c$ is not expected to be universal, but the other critical exponents could match, analogous to how percolation models on different $d$-dimensional lattices have different percolation thresholds but the same critical exponents. The results of Ref. [72], shown in Table 3.1, indicate that there may be a difference in certain *surface* exponents ($\eta_{||}$ and $\eta_{\perp}$), but that the bulk exponents appear to be unaffected. At any rate, what is particularly surprising is how close many of the bulk exponents are to the corresponding values from 2D percolation. This could be an indication that the RG fixed point at finite $q$ is 'near' to the percolation fixed point in some generalized phase diagram.

### 3.6.1 Diagnostics of the transition

In determining critical properties of a transition, it is extremely important to have an accurate estimate of the location $p_c$ of the critical point, since even small differences in $p_c$ can result in fairly large differences in resulting estimates of critical exponents. Given that much of the discussion of measurement-induced transitions has concerned the transition in the entanglement entropy, it seems natural for this to be used as a diagnostic of the transition, and indeed it was used as such in some of the early work on this transition. However, one key issue is that the entanglement entropy is not scale invariant at the critical point, but rather seems to increase with system size—for example, in 1+1D it seems to scale as $S(L) \propto \log L$ with subsystem size $L$. This means that to make a standard scaling ansatz for the entanglement entropy, it is necessary to subtract off the critical contribution to get a scale-invariant remainder. Concretely, one makes the ansatz

$$S(p, L) - S(p_c, L) \sim F\left[(p - p_c)L^{1/\nu}\right], \tag{3.17}$$

where $F$ is a single-parameter scaling function. Unfortunately, in practice this 'subtraction scheme' tends to lead to a sort of 'correlated uncertainty', where there is a large range of values of the critical point $p_c$ that lead to similar qualities of fit to the data, and large variation in the critical exponent $\nu$ depending on the fitted value of $p_c$. This also leads to correlated uncertainty in other critical exponents.

To get around this issue, it is helpful to look for different diagnostics of the transition from which one can more readily 'read off' the location of the critical point. One such diagnostic, proposed in Refs. [72, 80], is the *tripartite information*. Given a partition of the system into four subsystems $A$, $B$, $C$ and $D$, the tripartite information $I_3(A : B : C)$ is defined as

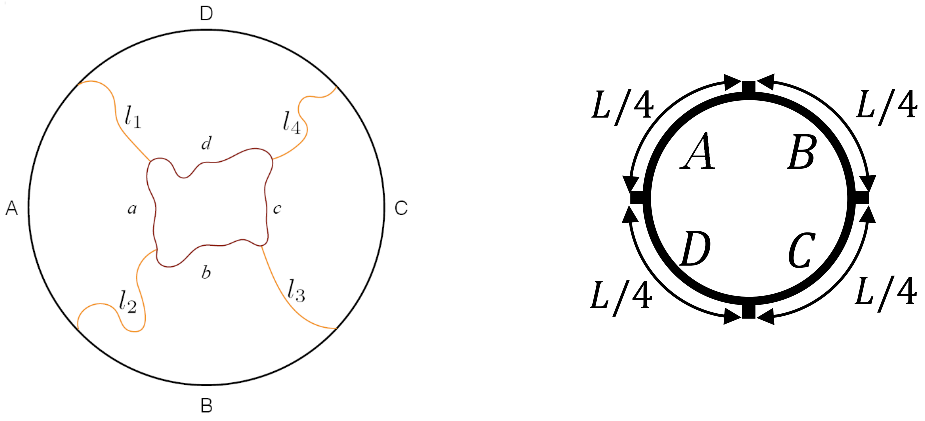

**(a)** **(b)**

**Figure 3.5:** **(a):** Geometry used to calculate the tripartite information. **(b):** Spacetime picture for calculating the tripartite information within the minimal cut formalism, taken from Ref. [72].

$$I_3(A:B:C) = I(A:B) + I(A:C) - I(A:BC), \tag{3.18}$$

where $I(A:B) = S_A + S_B - S_{AB}$ is the mutual information. It it easy to show that, if the system is in a pure state, given a partitioning into four subsystems, the tripartite information does not actually depend on the choice of which three subsystems are used to calculate it, so having fixed a partitioning we will refer to this quantity simply as $I_3$. The original proposal in Refs. [72, 80] focused on 1+1D systems with periodic boundary conditions, and used the partioning shown in Fig. 3.5b. The authors argue that, for this particular choice of geometry, the advantage of the tripartite information is that it cancels out any 'boundary terms' (in a sense I will explain shortly), such that the overall scaling is

$$I_3(p,L) \sim \begin{cases} \mathcal{O}(L), & p < p_c, \\ \mathcal{O}(1), & p = p_c, \\ 0, & p > p_c. \end{cases} \tag{3.19}$$

Importantly, the value at the critical point $p = p_c$ is independent of system size $L$, so the value of $p_c$ can be read off by looking for a crossing point between $I_3(p, L)$ for different system sizes.

The argument for this scaling is based on the 'minimal cut' formalism described in Section 3.5.1, in particular the connection it makes with percolation in the spacetime bulk of the quantum circuit. As such, although this argument is exact for the $(n = 0)$-Rényi entropy in Haar-random circuits, for other setups it is only a heuristic.

Recall that the minimal cut formalism dictates that the entanglement entropy $S_A$ of a contiguous region $A$ is given by the cost of a minimal length cut through the tensor network comprising the quantum circuit generating the final state: this can be pictured as a percolation problem in spacetime. A typical minimal cut will consist of two components: a 'bulk' component $a$, where the cut traverses through the largest 'void' in the bulk of the system where measurements have created a cost-free section to move through, and a 'boundary' component $l_i$, where the cut traverses from one of the boundary points of $A$ to get to the bulk void (see Fig. 3.5a). Separating the contributions to the entanglement entropy into these two components, we have

$$
\begin{aligned}
I_3 =& S_A + S_B + S_C - S_{AB} - S_{BC} - S_{AC} + S_{ABC}, \\
=& l_1 + l_2 + \min(a, b + c + d) + l_2 + l_3 + \min(b, a + c + d) \\
&+ l_3 + l_4 + \min(c, a + b + d) - l_1 - l_3 - \min(a + b, c + d) \\
&- l_2 - l_4 - \min(b + c, a + d) - l_1 - l_2 - l_3 - l_4 - \min(a + c, b + d) \\
&+ l_1 + l_4 + \min(d, a + b + c), \\
=& \min(a, b + c + d) + \min(b, a + c + d) + \min(c, a + b + d) \\
&- \min(a + b, c + d) - \min(b + c, a + d) - \min(a + c, b + d) + \min(d, a + b + c).
\end{aligned}
$$

Crucially, note that all the boundary terms $l_i$ cancelled out. These boundary terms are responsible for the $\log L$ scaling of the entanglement entropy at criticality, so removing this contribution results in the $I_3(p = p_c, L) \sim \mathcal{O}(1)$ scaling which makes the tripartite information a useful probe of the critical point. A similarly judicious choice of geometry was used by Kitaev and Preskill [101] to expose the 'topological term' in the area-law entanglement entropy of 2D topologically ordered systems—for this reason the tripartite information was there referred to as the 'topological entanglement entropy'.

## 3.7 Connection with quantum information scrambling

The notion that the quantum information describing a system can be encoded in highly non-local degrees of freedom, thereby resisting reconstruction by observers with access only to local observables, is known as *scrambling*. Quantum systems which are 'chaotic' are typically strongly scrambling. As an extreme example, a Haar-random unitary $U \in \mathrm{U}(d)$ applied to a pure state $|\psi_0\rangle$ will result in a state $U|\psi_0\rangle$ which looks *locally* very close to a *random* state in the high-dimensional limit $d \to \infty$ [53]. This means that, although it is in principle possible to recover the original state $|\psi_0\rangle$ by applying the inverse operation $U^\dagger$, this requires knowledge of the whole state $U|\psi_0\rangle$, and it is not possible to recover the original state of even a local region of the system without access to this global information.

More physical examples should constrain the dynamics to be local, in the sense of being generated by few-body interactions, and possibly also of being spatially local. Even with these restrictions, there are examples of quantum systems which are strongly scrambling: local random unitary circuits acting on a system of $N$ qudits generate $\epsilon$-approximate unitary $k$-designs in $\mathrm{poly}(t, N, d, \log 1/\epsilon)$ depth [102], which is a particularly strong sense of scrambling—the same is true for random time-dependent Hamiltonian systems [103]. Time independent Hamiltonian systems, one of the most physically relevant cases, do not quite scramble in the strong sense of approximating unitary designs [104], but nonetheless there are examples of Hamiltonian systems which are strong scramblers under a slightly weaker definition of scrambling, such as the exponential decay of out-of-time-ordered correlators [105, 106].

One interesting aspect of the measurement-induced phase transition can be found by asking how the underlying unitary dynamics affects the nature of the phase transition. One of the original motivations for studying these 'hybrid' quantum systems, consisting of alternating unitary dynamics and measurements, was to give a 'minimal model' for the effect of the environment on the dynamics of a quantum system—the measurements constitute *local* interactions between the system and the environment in which, roughly speaking, the environment extracts some information about the state of the system. This suggests that the harder it is for the environment to learn something about the system by measuring local observables, the more resilient the properties of the unitary dynamics will be to the introduction of measurements. More concretely, we expect that more strongly scrambling unitary dynamics will result in larger values of the critical measurement probability $p_c$.

In fact, recent evidence suggests something sharper: a dichotomy between 'strongly scrambling' and 'weakly scrambling' quantum systems. In strongly scrambling systems, such as random quantum circuits or chaotic Hamiltonian models, the critical measurement probability is *nonzero* [66–70, 72–76, 80, 82, 83, 85, 88, 89, 107], whereas in weakly scrambling systems, such as free fermion systems or certain integrable models, the critical measurement probability is *zero* [67, 87, 108], meaning that there is a qualitative change in the entanglement scaling as soon as one introduces measurements at *any* finite rate. In this sense, the entanglement generated by chaotic quantum systems is much more robust than that generated by weakly scrambling quantum systems. This can also be seen through the complementary lens of quantum error correction. Quantum chaotic systems generate quantum error-correcting codes—these codes are somewhat like random codes, but retain a sense of locality due to the locality of the underyling dynamics [80, 109].

## 3.8 Scalability in experiments

As a potentially novel class of phase transition, it would be of great interest to realize a measurement-induced phase transition in an experimental setting. However, there are two barriers to performing the experiment directly in line with the first theoretical explorations, which consisted of random quantum circuits interspersed with measurements. These barriers both become increasingly severe as the system size increases, but it is precisely this limit which is of interest, since only there will the phase transition become apparent.

The first challenge is to measure the entanglement entropy. To calculate the von Neumann entropy, it is necessary to perform full state tomography [110]. This has a cost which scales exponentially with system size, and is unlikely to be feasible beyond 10–20 spins. However, this barrier could possibly be avoided by giving up on the von Neumann entropy and instead calculating a different Rényi entropy. As discussed in previous sections, the $(n \geq 1)$-Rényi entropies seem to have similar scaling properties in the different measurement-induced phases, so this is a reasonable strategy. The Rényi entropies with $n \geq 2$ and integral are easiest to measure, since they correspond to observables in an $n$-fold replicated system. More specifically, the idea is to utilize the identity $\mathrm{tr}[\rho^n] = \mathrm{tr}[S_n \rho^{\otimes n}]$, where $S_n$ is the cyclic permutation operator which permutes the $n$-fold replicated Hilbert space. To do this in an experiment, one has to prepare $n$ *identical* copies of the state, and then measure the operator $S_n$ — in a sense this is a form of interferometry. Clearly this is easiest when $n = 2$, but even then it is still quite a challenge! Nonetheless, in recent years extremely impressive experiments have been performed along these lines [111], so this barrier is not unsurmountable.

However, the next barrier seems more problematic. Even avoiding full state tomography, to be able to measure the expectation value of an operator in a given state $\rho$ requires the ability to repeatedly generate $\rho$, so as to generate sufficient statistics to get a reasonable estimate of the expectation value. Given that the measurements occur randomly in spacetime and have random outcomes, this generates another exponential overhead. Even if we fix the locations of the measurements, their random outcomes mean that if the measurement probability is $p$ and there are $N$ spins with local Hilbert space dimension $q$ which undergo $T$ rounds of measurement, then the number of repetitions to get $O(1)$ samples of a given trajectory is of the order $q^{pNT}$. In fact, since the equilibration time is typically at least $T \sim O(N)$ for local dynamics, this overhead can be exponential in $N^2$.

To date there has been one experiment exploring measurement-induced phase transitions [112], which was performed with a system of trapped ions. They explored the transition through the lens of purification, which fairly generically seems to coincide with the entanglement transition. One strategy they use to mitigate the cost of having many measurements is to consider a slight alteration of the standard protocol. The native two-qubit entangling gate in their system is an 'Ising gate' of the form $U(\theta) = \exp(i\theta\sigma_1^x\sigma_2^x)$. Notice that if measurements are performed in the $\sigma^x$ basis then the steady state will simply be a product state, since the Ising gates cannot generate entanglement from $\sigma^x$ basis product states. Exploiting this fact, the authors consider a protocol where the overall density of measurements $p$ is fixed at a fairly small number, limiting the total number of measurements they have to perform. They then sweep an additional variable, $p_x$, which controls the fraction of measurements that are performed in the $\sigma^x$ basis. The system then transitions from the mixed phase to the pure phase as $p_x$ is increased.

## Chapter 4

# Measurement-induced transitions in many-body localized systems

In this chapter we study the dynamics of an MBL Hamiltonian subjected to projective measurements. Many-body localized systems are characterized by a complete set of quasi-local operators, also known as ‘l-bits’, which are conserved under the dynamics of the system’s Hamiltonian (see Fig. 4.1c) [55, 57, 113, 114]. Due to this robust integrability, one might guess that the measurement-induced entanglement transition in MBL systems is similar to that in integrable systems. Although measurements in MBL and disorder-free integrable models share certain similarities, here we show that measurement-induced transitions performed in certain *bases* (see Fig. 4.1a) can have distinct properties.

To illustrate this point, recall that in a chaotic quantum system local operators spread ballistically, resulting in the rapid scrambling of information with time which can be diagnosed through the decay of out-of-time-order correlators (OTOCs). The implication of this for the measurement-induced entanglement transition is that in chaotic systems the choice of measurement basis does not matter, provided it is local (i.e. close to a tensor product basis). However, in an MBL system, only operators without any overlap with the l-bits are totally scrambled with their out-of-time ordered correlators decaying to zero. For

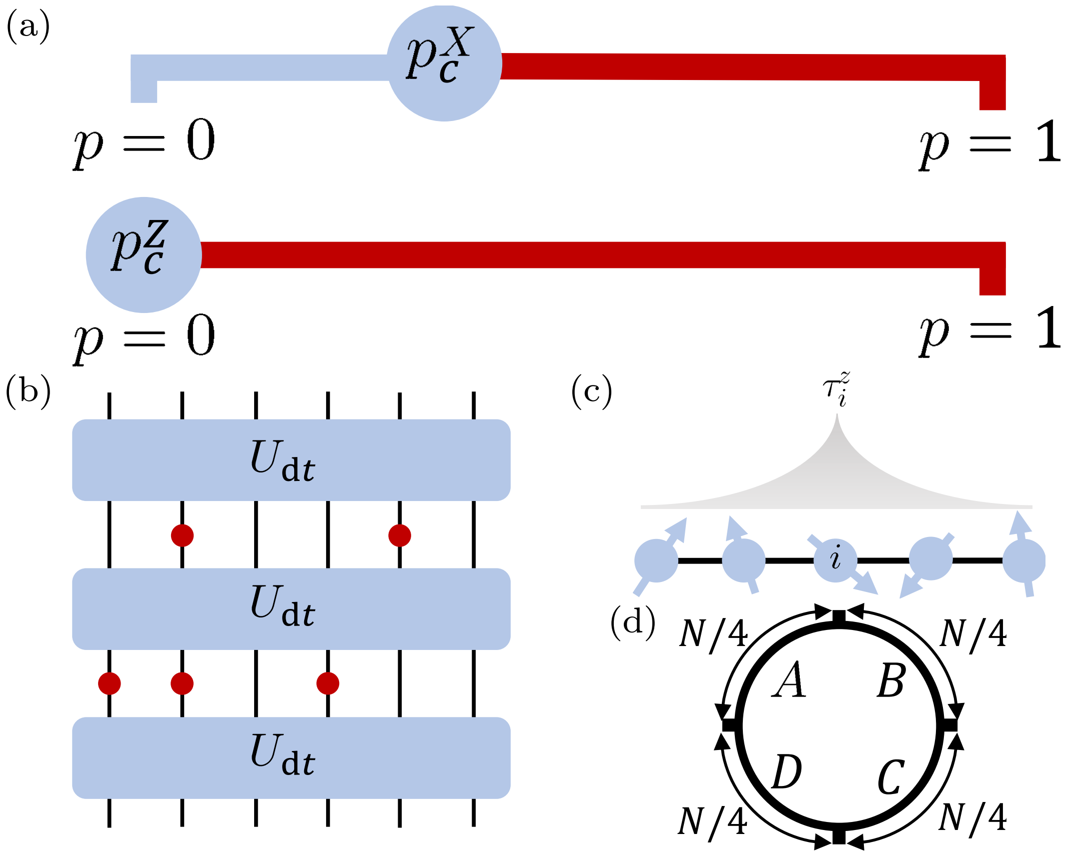

**Figure 4.1:** **(a)** The critical properties of the transition depend on the measurement basis. Measurements in the X-basis result in a transition from volume-law to area-law entanglement at nonzero $p = p_c^X > 0$, similar to chaotic systems, whereas measurements in the Z-basis result in area-law entanglement for any nonzero $p$, similar to integrable systems. **(b)** Each stage of the dynamics consists of two steps. First the system is evolved in time with the unitary $U_{\mathrm{dt}} = \exp(-iH\mathrm{d}t)$, with $H$ given in Eq. (4.1), and then for each spin we projectively measure in a tensor-product basis with probability $p$ (measurements are represented by the red dots). **(c)** A schematic of the typical support of an 'l-bit' operator, localized at site $i$, in the fully MBL phase. **(d)** A depiction of the geometry used to calculate the tripartite information $I_3(A : B : C)$.

example, the late-time limit of the disorder-averaged OTOC of an operator is set by its overlap with the local integrals of motion of the MBL system [115–120]. For the model described by Eq. (4.1), in the strong-disorder limit $W \gg 1$ the l-bits $\{\tau_i^z\}$ are close to the local spin operators $\{S_i^z\}$, dressed by exponentially decaying tails [121–125], as shown in Fig. 4.1c. The l-bits are related to the physical spins by a quasi-local unitary $U$ via $\tau_i^z = US_i^zU^\dagger$, with $U \to \mathbb{1}$ in the strong-disorder limit. This means that the overlap of an operator $O$ with an l-bit $\tau_i^z$ is given by $\mathrm{tr}\left[O\tau_i^z\right] = \mathrm{tr}\left[OS_i^z\right] + \cdots$, where the dots indicate terms which vanish in the limit $W \longrightarrow \infty$. As a result, the operator $S_i^x$ is scrambled by the MBL system, whereas the operator $S_i^z$ remains approximately localized.

This has the consequence that there is a qualitative difference between the nature of the measurement-induced entanglement transition in an MBL system depending on whether the measurements are performed in the basis of $S_i^x$ eigenstates (X-basis) or the basis of $S_i^z$ eigenstates (Z-basis), as shown in Fig. 4.1a. With measurements in the X-basis, the transition from volume to area-law entanglement occurs at a nonzero measurement probability $p_c^X > 0$, similar to previously studied chaotic systems [66–70, 72–76, 80, 82, 83, 85, 88, 89, 107]. On the other hand, with measurements in the Z-basis, the volume-law is destroyed for any nonzero $p$, similar to previously studied integrable systems [67, 87, 108].

This difference can also be related to the interplay between measurements and the phenomenology of entanglement growth in MBL systems. As we discuss in Section 4.1.2, in a measurement-free MBL system, the steady state entanglement is governed by the diagonal entropy, which is constant under Hamiltonian time evolution. Here we show that measurements induce dynamics in the diagonal entropy which qualitatively differ between X-basis measurements and Z-basis measurements, where X-basis measurements tend to maximize the diagonal entropy while Z-basis measurements tend to minimize it. This then drives the steady state to volume-law or area-law entanglement, depending on the measurement basis.

In a recent work [96], the authors investigated the dynamics of a finite-range l-bit model of MBL under local Clifford dynamics. We analyze the full l-bit Hamiltonian, which includes infinite-range interactions between l-bits. It also provides a picture of the measurement-induced entanglement transition in a fully realistic model of MBL and our results are consistent with results in

Ref. [96] where they can be compared.

## 4.1 Model

We study a standard model of MBL, the disordered spin-$\frac{1}{2}$ Heisenberg chain, with a Hamiltonian given by

$$H = J \sum_{\langle ij \rangle} \mathbf{S}_i \cdot \mathbf{S}_j + \sum_{i=1}^{N} h_i S_i^z \tag{4.1}$$

where the $h_i$ are random variables drawn from the uniform distribution on $[-h, h]$, and the double sum runs over nearest neighbours. We use periodic boundary conditions unless stated otherwise. For sufficiently large disorder strength $W \equiv h/J$ this model is many-body localized. Early studies of MBL based on exact diagonalization estimated the critical disorder strength $W_c$ to be around $W_c \approx 3.6$ [126, 127], though more recent studies have argued that $W_c$ has significant finite-size corrections, and have suggested a figure of $W_c \approx 5$ [128]. In this paper we are interested in the region well into the localized phase, and so will take $W = 10$, large enough to avoid issues with finite-size drifts of $W_c$.

To study the effects of measurements on the entangling properties of MBL dynamics, we consider a repeated two-stage protocol, as illustrated in Fig. 4.1b. Starting from an initial Haar-random product state, we apply unitary dynamics generated by the Hamiltonian for some time $\mathrm{d}t$, i.e. $|\psi\rangle \to U_{\mathrm{d}t}|\psi\rangle$, where $U_{\mathrm{d}t} = \exp(-iH\mathrm{d}t)$. Unless otherwise specified we take $\mathrm{d}t = 1$ in units of $J$, independent of $N$, to make the situation comparable with random local circuit models. Then for each spin we projectively measure in a local tensor-product basis with probability $p$, where $p$ can be interpreted as the density of measurements in spacetime. The measurement outcomes are chosen according to the Born rule. To implement a measurement on spin $i$ with outcome $\lambda$, the state is updated via the usual rule $|\psi\rangle \to P_i(\lambda)|\psi\rangle / \|P_i(\lambda)|\psi\rangle\|_2$, where $P_i(\lambda) = |\lambda\rangle\langle\lambda|_i$ is the projector on to the eigenspace associated with the measurement outcome $\lambda$. This process is repeated until the entanglement entropies reach a steady state.

### 4.1.1 Transition diagnostics

To study the measurement-induced entanglement transition in this MBL system, we performed the time-evolution using exact diagonalization. We made use of the fact that the Hamiltonian $H$ in Eq. (4.1) conserves total $S^z$, so in a basis ordered by total $S^z$, $H$ is block-diagonal and one can diagonalize the blocks separately.

To characterize the transition we focused on two quantities: the von Neumann entropy $S_X = -\mathrm{tr}[\rho_X \ln \rho_X]$, and the tripartite information

$$I_3(A : B : C) = I(A : B) + I(A : C) - I(A : BC), \tag{4.2}$$

where $I(A : B) = S_A + S_B - S_{AB}$ is the mutual information. We calculate $I_3(A : B : C) \equiv I_3$ for the geometry shown in Fig. 4.1d. It is easy to show that for a system partitioned into four subsystems, the tripartite information of any three of the subsystems does not depend on the choice of subsystems, so once the partitioning is fixed there is no ambiguity in calling this quantity $I_3$.

As discussed in Refs. [72, 80], the advantage of using the tripartite information here is that it avoids any $\log N$ divergences in the entanglement entropy at criticality, which have been observed in hybrid Haar-random circuit models [72]. Instead, $I_3$ is expected to scale as $I_3 \propto -N$ in the volume-law phase, reach an $\mathcal{O}(1)$ constant at criticality, and then vanish in the area-law phase. This is especially important given the limited system sizes accessible by exact diagonalization.

Throughout this paper we will mostly focus on the von Neumann entropy, and quantities defined in terms of it. However, one can also consider the transitions in the broader family of Rényi entropies, defined as

$$S_n(\rho) = \frac{1}{1-n} \ln \mathrm{Tr}[\rho^n]. \tag{4.3}$$

The Rényi-$n$ entropy tends to the von Neumann entropy in the limit $n \to 1$. For $n > 1$, there is the inequality $S_\infty \leq S_n \leq \frac{n}{n-1} S_\infty$, which implies that all Rényi-$n$ entropies with $n > 1$ must have the same scaling with system size. We consider the transition in the Rényi entropies in Section 4.3.

### 4.1.2 Diagonal entropy

The qualitative difference in the dynamics of the entanglement entropies with Z- or X-basis measurements can also be related to the interplay of measurements with the phenomenology of entanglement growth in MBL systems. In the absence of measurements, the steady-state entanglement of an MBL system is set by the diagonal entropy of the initial state in the energy eigenbasis [54–58], $S(t \to \infty) \propto S_{\text{diag}}(|\psi(0)\rangle)$, with

$$S_{\text{diag}}(|\psi(0)\rangle) = -\sum_i p_i \ln p_i, \quad p_i = |\langle E_i|\psi(0)\rangle|^2, \tag{4.4}$$

where the $\{|E_i\rangle\}$ are the eigenstates of $H$. This is a result of dephasing between l-bits. For many classes of initial states, such as random product states, the average diagonal entropy is extensive in the strong disorder regime, thus giving rise to volume-law steady state entanglement in MBL systems.

It is worth noting that $S_{\text{diag}}$ is constant under time-evolution by $H$, since it depends only on the magnitude of the amplitudes $\langle E_i|\psi(t)\rangle$, which merely pick up a phase. However, once measurements are introduced, the diagonal entropy is no longer preserved in time. Instead, the measurements drive the diagonal entropy to a new steady state, typically at an exponential rate $\lambda \approx p$. The choice of measurement basis determines the nature of this new steady state. In the strong disorder limit, the eigenstates of $H$ are close to product states of $S_i^z$ eigenstates. Thus measurements in the Z-basis tend to drive the diagonal entropy close to zero (see Fig. 4.4), whereas measurements in the X-basis tend to drive it close to its maximum value (see Fig. 4.6).

## 4.2 Entanglement dynamics with Z-basis measurements

In this section we focus on unitary MBL dynamics interspersed with random projective measurements in the Z-basis, and demonstrate the fact that there is a qualitative difference once measurements are introduced with any arbitrarily small probability $p$. That this transition occurs at $p_c^Z = 0$ is similar to previously studied integrable systems [67, 87, 108], which is consistent with the picture of MBL as a form of quasi-integrability robust to local perturbations.

Fig. 4.2 shows a comparison of the dynamics of the tripartite information $I_3$ between $p = 0$ and $p > 0$. For $p = 0$, $I_3$ grows in magnitude logarithmically in time before saturating to a volume-law, similar to the well-known behaviour of the half-chain entanglement entropy. On the other hand, for $p > 0$ the tripartite information initially grows at early times while the diagonal entropy is still large, reaching an area-law peak (see Fig. 4.3b), but eventually the measurements dominate and $I_3$ decays to a smaller area-law. This area-law peak also appears in the Bell pair model of Ref. [67], but there it occurs at an $\mathcal{O}(1)$ time $t_{\text{peak}} \sim 1/p$. In this system, the peak time does still scale as $1/p$, but it also increases with system size (see top panel of Fig. 4.3b). This intermediate-time peak may be a consequence of the total $S^z$ conservation of the Hamiltonian in Eq. (4.1). The initial state is a superposition of a large number of total $S^z$ sectors, allowing for a potentially large entropy at early times, but the Z-basis measurements drive the state towards a Z-basis product state, such that the steady state may only be in a superposition of a few total $S^z$ sectors.

The inset to Fig. 4.2 shows that the dynamics can be reasonably well described

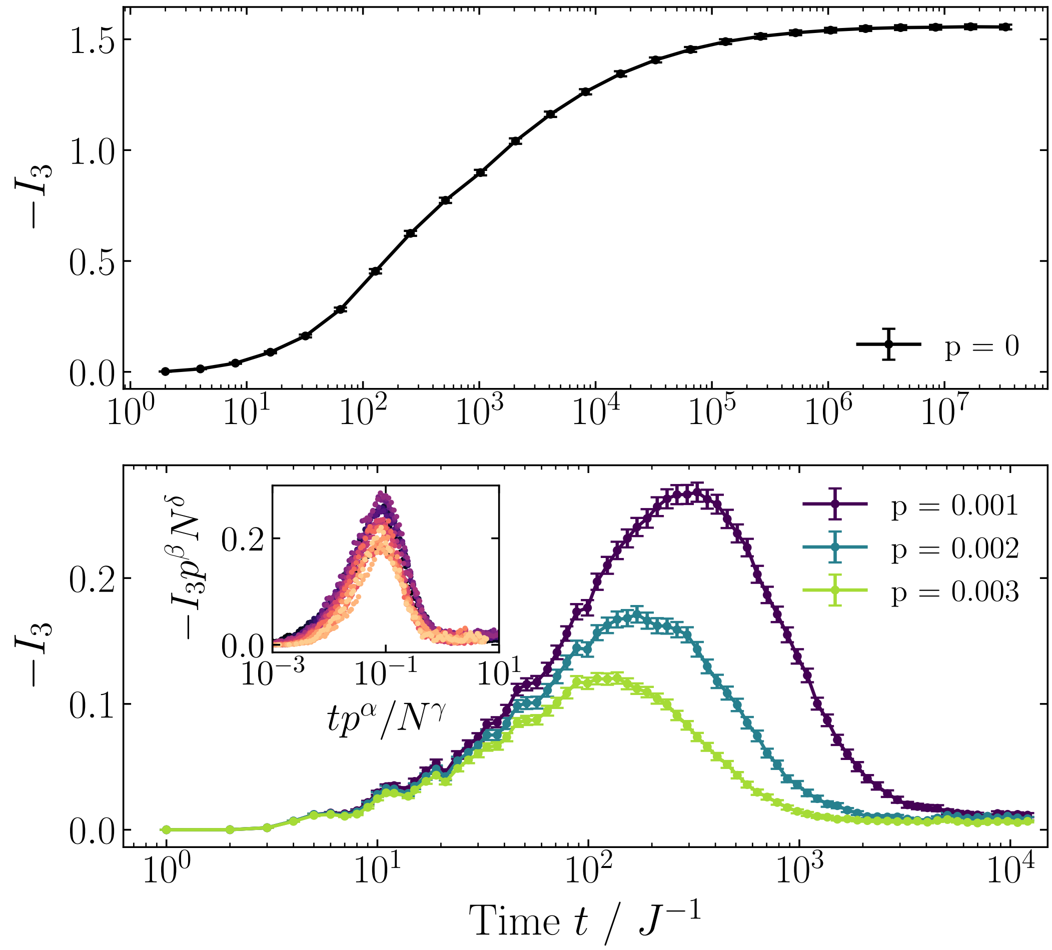

**Figure 4.2:** A comparison of the dynamics of the tripartite information $I_3$ for $p = 0$ and $p > 0$ with Z-basis measurements, with $N = 12$. For $p = 0$, $I_3$ grows logarithmically in time before saturating to a volume-law. For $p > 0$, $I_3$ initially grows in time, reaching an area-law peak, before decaying to a constant which decreases with system size. The inset shows that the dynamics can be reasonably well described by the scaling form $-I_3(t, p, N) = F[tp^\alpha/N^\gamma]/p^\beta N^\delta$, where $F$ is a single-parameter scaling function and $\alpha = 0.77$, $\beta = 0.80$, $\gamma = 1.14$ and $\delta = 2.19$. The inset data corresponds to 20 separate time series, with $N = 12, 16$ and $0.0005 \leq p \leq 0.005$.

by the scaling form $-I_3(t, p, N) = F[tp^\alpha/N^\gamma]/p^\beta N^\delta$, where $F$ is a scaling function and $\alpha = 0.77$, $\beta = 0.80$, $\gamma = 1.14$ and $\delta = 2.19$. We also tested scaling $I_3$ by an exponential in $N$, so $-I_3(t, p, N) = \tilde{F}\left[tp^{\tilde{\alpha}}/N^{\tilde{\gamma}}\right]/p^{\tilde{\beta}} \exp(N\tilde{\delta})$, which resulted in the exponents $\tilde{\alpha} = 0.77$, $\tilde{\beta} = 0.77$, $\tilde{\gamma} = 1.14$ and $\tilde{\delta} = 0.20$. The quality of both fits were qualitatively similar, so with the system sizes accessible we were unable to rule out power-law or exponential scaling of

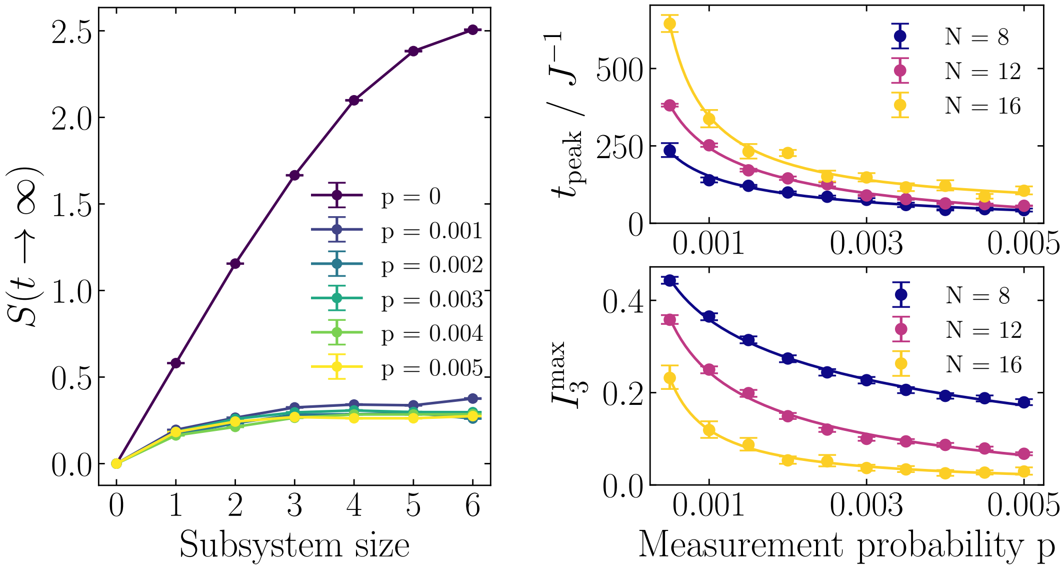

(a) (b)

**Figure 4.3:** **(a)** Scaling of the von Neumann entropy at saturation with subsystem size for a system of size $N = 12$. For $p = 0$ this quantity obeys a volume-law, but for $p > 0$ it saturates to an area-law. **(b)** Scaling of the time $t_{\text{peak}}$ and height $I_3^{\max}$ of the intermediate time peak in the tripartite information $I_3$, as seen in Fig. 4.2. The solid lines are power law fits, decaying approximately as $p^{-1}$. With increasing system size, the peak occurs at later times and is smaller in magnitude, indicating that it is (sub-)area-law.

the $I_3$ peak height with $N$. Regardless, in either case in the thermodynamic limit $N \to \infty$ we expect the steady-state tripartite information to scale to zero with $N$ for any $p > 0$, indicating the instability of the volume-law phase to measurements.

Focusing further on the transition in the steady state, Fig. 4.3a shows the von Neumann entropy of contiguous subsystems of different sizes in the steady state. Whereas for $p = 0$ this quantity is extensive, for $p > 0$ it quickly becomes independent of the size of the subsystem, indicating an area-law. This behaviour can be linked to the measurement-induced dynamics of the diagonal entropy $S_{\text{diag}}$, which governs the steady state entanglement in the measurement-free system. Fig. 4.4 shows that, for any $p > 0$, the diagonal entropy decays exponentially in time, before reaching a steady state which is independent of $p$. The inset to Fig. 4.4 shows that the decay rate $\lambda$ scales

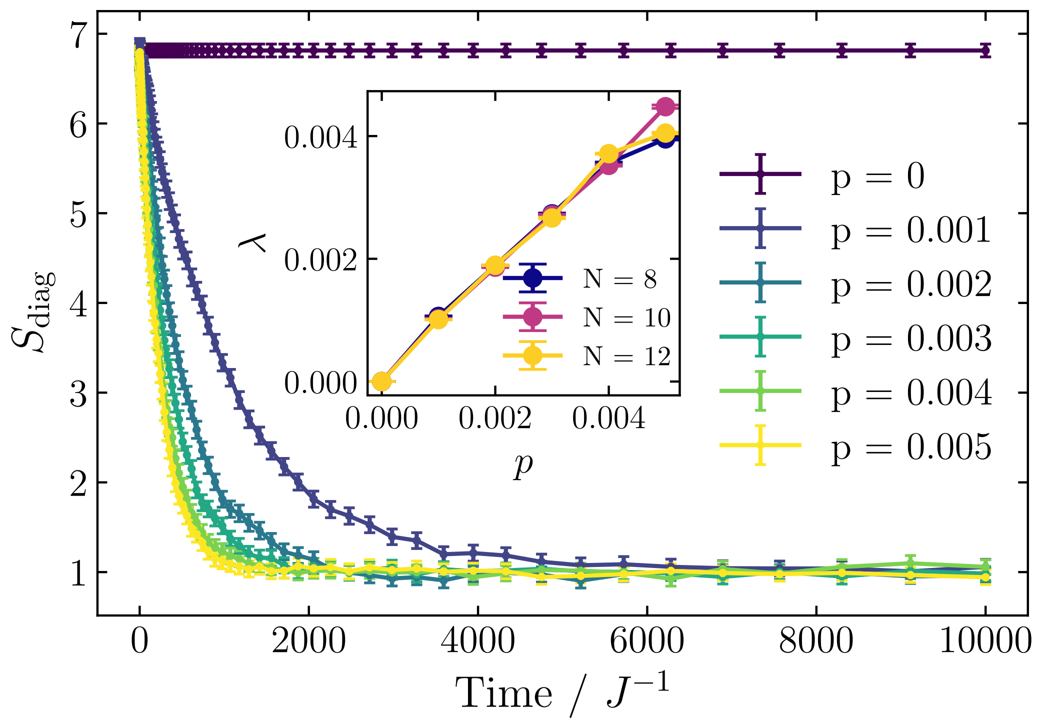

**Figure 4.4:** Dynamics of the diagonal entropy $S_{\mathrm{diag}}$ using the energy eigenbasis, with Z-basis measurements and $N = 12$. $S_{\mathrm{diag}}$ is preserved by Hamiltonian evolution, so for $p = 0$ it remains constant in time. For $p > 0$, projective Z-basis measurements cause it to decay exponentially at a rate proportional to $p$. The inset shows the dependence of the early-time decay rate $\lambda$ on $p$ and $N$, with $\lambda \approx p$, independent of $N$.

approximately as $\lambda \approx p$, independent of system size. We expect this result to hold throughout the fully MBL regime as a result of the strongly localized nature of the l-bits, and the fact that the measurements are performed independently on each site.

## 4.3 Entanglement dynamics with X-basis measurements

Having seen in Section 4.2 the collapse of the MBL steady-state volume-law when the dynamics are interspersed with arbitrarily rare Z-basis measurements, we now demonstrate that this volume-law is more resilient to measurements in the X-basis. More precisely, we aim to show that there is a *nonzero* critical measurement probability $p_c^X > 0$, below which the steady-

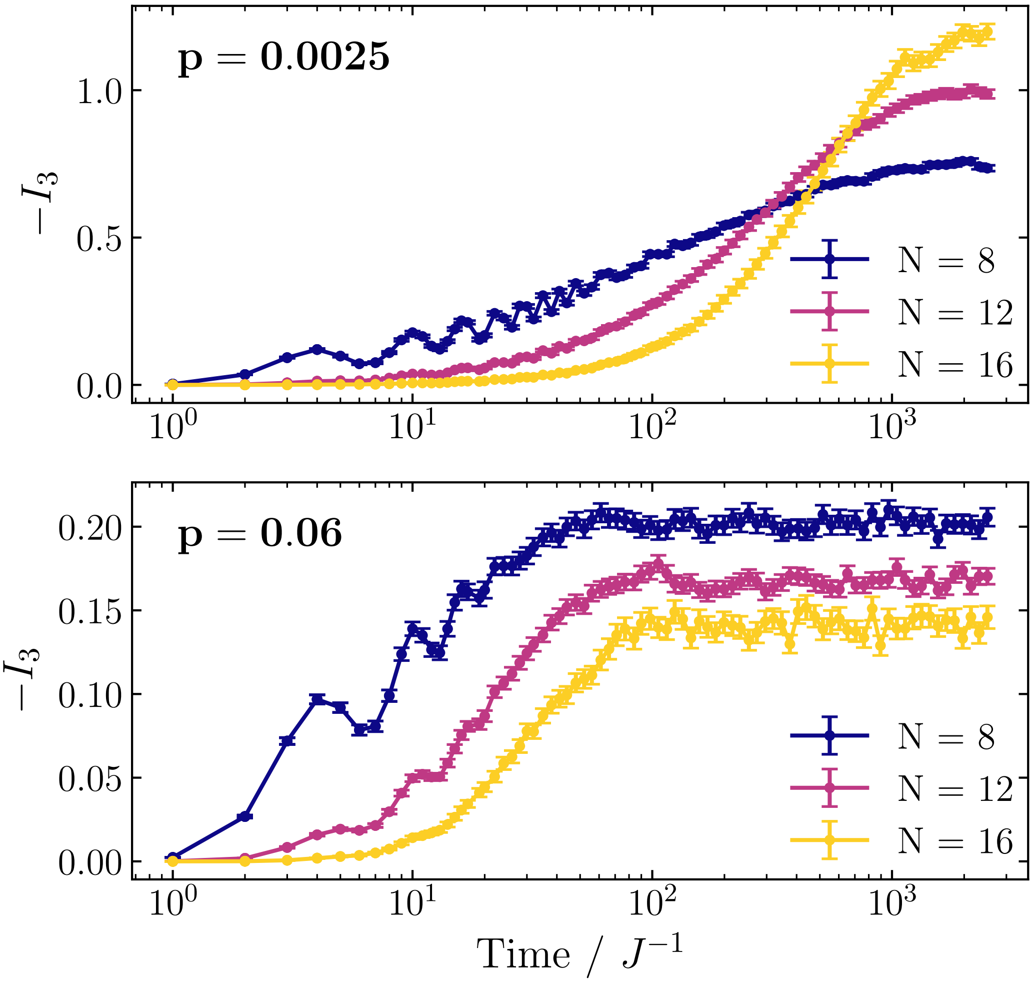

**Figure 4.5:** A comparison of the dynamics of the tripartite information $I_3$ with X-basis measurements for values of $p$ below and above the transition at $p_c^X \approx 0.014$. For $p = 0.0025$, $I_3$ grows logarithmically in time before saturating to a volume-law. By $p = 0.06$, the system size scaling has reversed, indicating a transition to an area law.

state volume-law persists. This scenario is similar to the case in previously studied chaotic systems [66–70, 72–76, 80, 82, 83, 85, 88, 89, 107].

The top panel of Fig. 4.5 shows the dynamics of the tripartite information $I_3$ for nonzero $p = 0.0025$, which is below the critical measurement probability $p_c^X \approx 0.014$. Here the dynamics are qualitatively similar to those for $p = 0$, shown in the top panel of Fig. 4.2, where the magnitude of $I_3$ grows logarithmically in time before saturating to a steady-state value which increases with system size. The bottom panel of Fig. 4.5 shows that, above the transition $p > p_c^X$, the

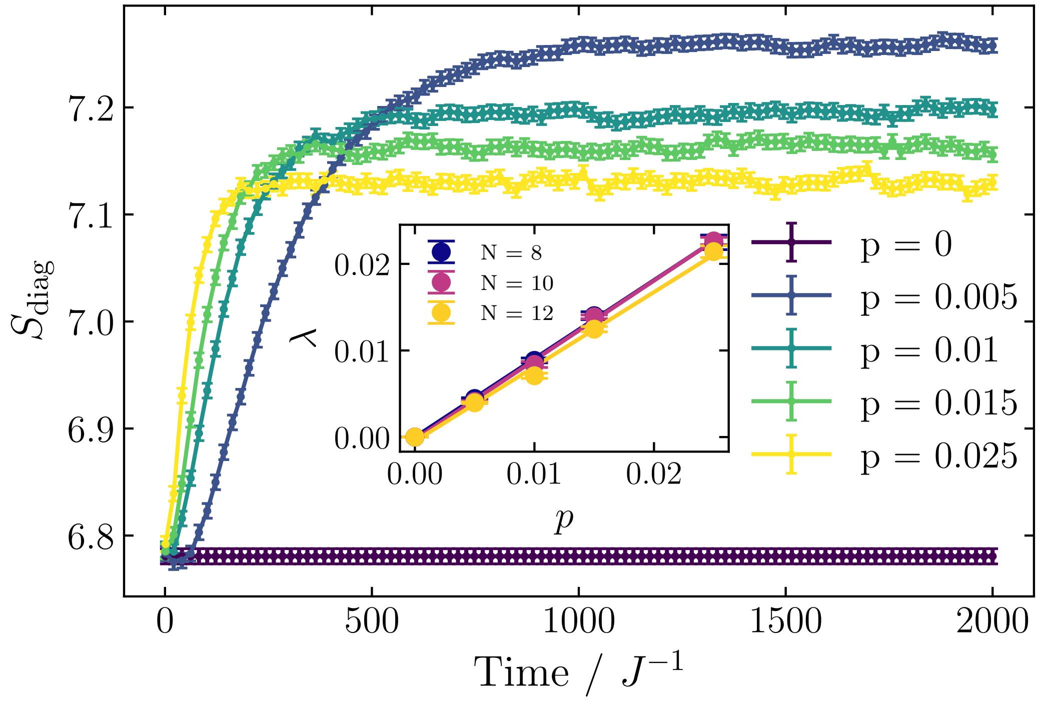

**Figure 4.6:** Dynamics of the diagonal entropy $S_{\rm diag}$ using the energy eigenbasis, with X-basis measurements and $N = 12$. $S_{\rm diag}$ is preserved by Hamiltonian evolution, so for $p = 0$ it remains constant in time. For $p > 0$, projective X-basis measurements cause it grow as $S_{\rm diag}(t) = S_{\rm diag}(0)e^{-\lambda t} + S_{\rm diag}(\infty)(1 - e^{-\lambda t})$ at a rate $\lambda$ proportional to $p$. The inset shows the dependence of the early-time decay rate $\lambda$ on $p$ and $N$, with $\lambda \approx p$, independent of $N$.

magnitude of $I_3$ still grows logarithmically in time, but no longer saturates to an extensive steady state, indicating a transition to an area law. The growth of the diagonal entropy is qualitatively similar for all nonzero $p$—it follows the functional form $S_{\rm diag}(t) = S_{\rm diag}(0)e^{-\lambda t} + S_{\rm diag}(\infty)(1 - e^{-\lambda t})$, with the growth rate $\lambda$ proportional to $p$, as shown in Fig. 4.6. Interestingly, in contrast to the case with Z-basis measurements, here $S_{\rm diag}(\infty)$ decreases with $p$. This may be a consequence of the finite disorder-strength, which means that the energy eigenstates aren't exactly product states.

It is also worth noting that, as a result of the increase in diagonal entropy induced by X-basis measurements, it is possible to boost the steady state entanglement relative to $p = 0$ for initial states with non-maximal diagonal entropy, contrary to the usual picture of measurements only destroying entanglement. Of course, this effect is relevant only for fairly small $p$, since for larger $p$ the disentangling power of the individual measurements overcomes the boost from the increased diagonal entropy.

With the goal of studying the transition point between the volume- and area-law phases, we show in Fig. 4.7 the steady state tripartite information $I_3$ as a function of measurement probability $p$ and system size $N$. To estimate the properties of the critical point, we assume a scaling function of the form $I_3(t \to \infty, p, N) = F\left[(p - p_c^X)N^{1/\nu}\right]$, and perform a fit to minimize the least-squares distance between each scaled point and the line obtained by a linear interpolation between its neighbours (see the supplementary material of Ref. [72] for more details). This yields the parameters $p_c^X = 0.014(2)$ and $\nu = 1.3(2)$, where the error bars correspond to the region where the cost function from the fit is less than 1.3 times its minimum. We expect $p_c^X$ to vary with the time step $\mathrm{d}t$, so we do not believe it will display universal behaviour. However, the critical exponent $\nu$ is close to the value of $\nu = \frac{4}{3}$ for 2+0D percolation, similar to the results in random local unitary circuits [72]. To test for the presence of conformal symmetry at the critical point, we also extract the dynamical critical exponent $z$ using the method described in Refs. [72, 85] of using the entanglement entropy of a single ancilla qubit as an order parameter for the transition. This yields $z = 0.98(4)$, as shown in Fig. 4.9, close to the value of $z = 1$ for conformal symmetry.

Finally, having obtained an estimate for the critical point, we examine the scaling of the steady-state entanglement entropy $S_n^l(p = p_c^X)$ with subsystem size $l$ at criticality, where $n$ indicates the Rényi index. In random circuit models with interspersed measurements, $S_n^l(p = p_c^X)$ was found to scale logarithmically with $l$, suggesting an underlying conformal field theory (CFT) description. In Fig. 4.8b, we plot $S_n^l(p = p_c^X)$ as a function of $\ln l$, and find a similar logarithmic scaling, albeit for fairly small subsystem sizes. The coefficient $\alpha(n)$ of the log term depends on the Rényi index $n$, as shown in Fig. 4.8c, with the dependence well described by $\alpha(n) = \alpha(\infty)(1 + 1/n)$,

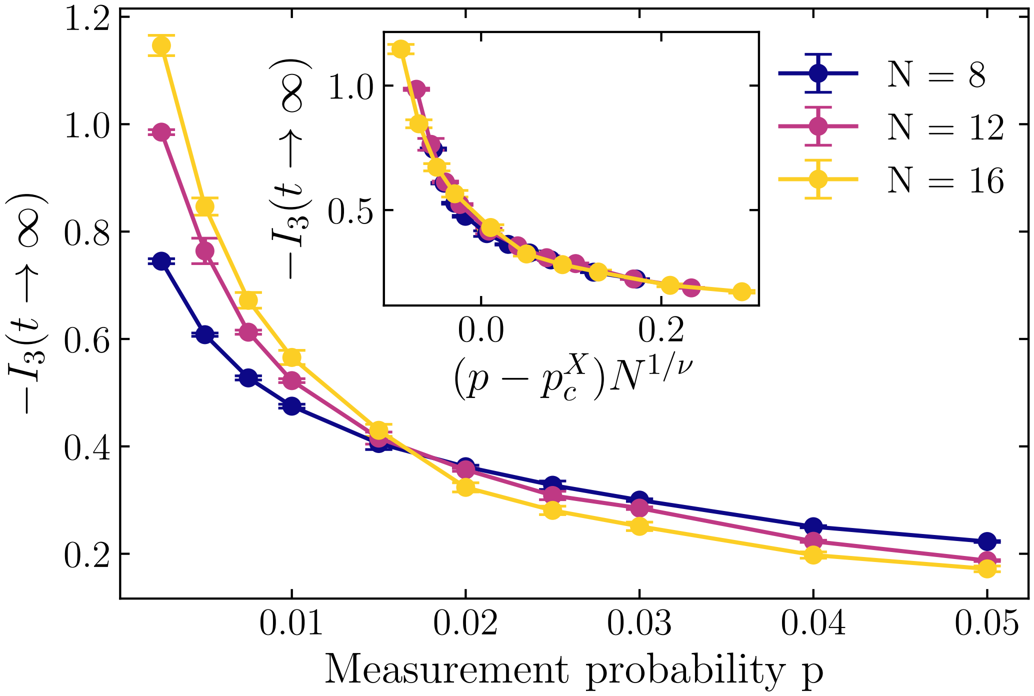

**Figure 4.7:** The steady state tripartite information $I_3$ as a function of measurement probability $p$ and system size $N$. The inset shows a data collapse with the fitted parameters $p_c^X = 0.014(2)$ and $\nu = 1.3(2)$.

which is the behaviour expected for unitary CFTs [129]. Interestingly, in Ref. [72] the authors found for spin-$\frac{1}{2}$ Haar-random circuits that $\alpha(n)$ was not quite described by a fit of this form, but rather required an offset, $\alpha(n) = a(1 + 1/n) + b$. This departure from the behaviour of unitary CFTs could be seen as consistent with the fact that, in the analytically solvable limit of infinite local Hilbert space dimension $q \to \infty$, the measurement-induced transition in a Haar-random circuit is described by a *non-unitary* CFT [75], though there may be important differences between $q \to \infty$ and finite $q$. Still, that $\alpha(n)$ in this spin-$\frac{1}{2}$ hybrid-MBL system is instead well described by the formula for a unitary CFT suggests that the transition in this system is quite distinct in character from that in Haar-random circuits. Finally, we note in passing that the value of $\alpha(\infty) \approx 0.34$ in this system is far from the value of $\alpha(\infty) \approx 0.49$ observed numerically in spin-$\frac{1}{2}$ Haar-random circuits [72], but close to the value of $\alpha(n) = \frac{1}{3}$ for all $n \geq 1$ predicted in Ref. [75] for

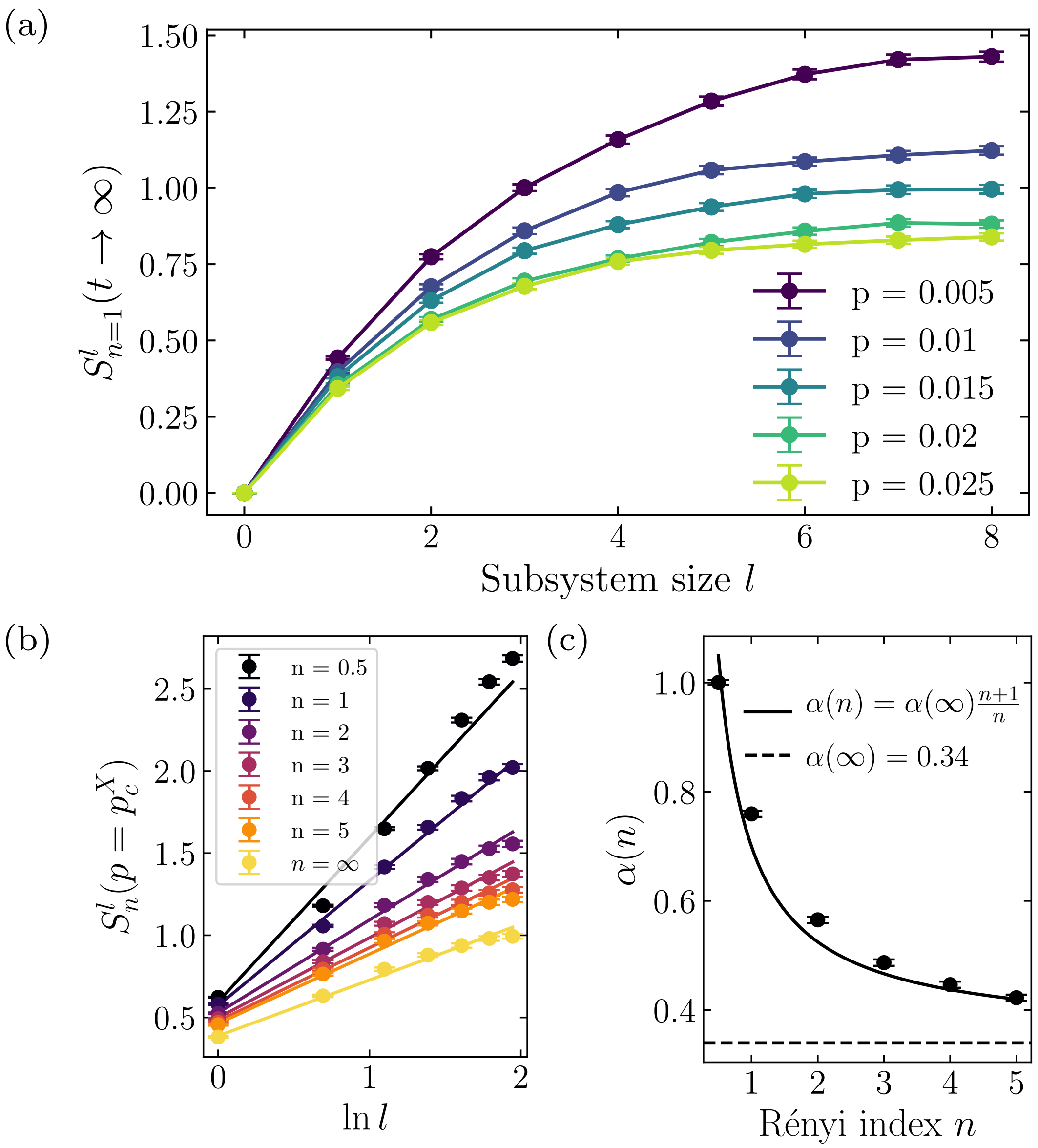

**Figure 4.8:** **(a)** Scaling of the steady-state von Neumann entropy with subsystem size $l$. The transition from volume to area-law occurs at $p^X_c \approx 0.014$. **(b)** The steady-state Rényi-$n$ entropies at criticality as a function of $\ln l$. The straight lines are fits to $S^l_n(p = p^X_c) = \alpha(n) \ln l + \beta(n)$. **(c)** The dependence of the log coefficient $\alpha(n)$ on the Rényi index $n$. The solid line is a fit to the form $\alpha(n) = \alpha(\infty)(1 + 1/n)$, where $\alpha(\infty) \approx 0.34$.

the $q \longrightarrow \infty$ Haar-random circuit model with periodic boundary conditions, though as emphasized this limit is far from the system considered here. It is also somewhat close to the value of $\ln 2 \times \frac{\sqrt{3}}{\pi} \approx 0.38$ for 2+0D percolation with periodic boundary conditions [68, 130, 131], but, at least in hybrid Haar-random circuits, this value is correct only for the Rényi-0 entropy [75].

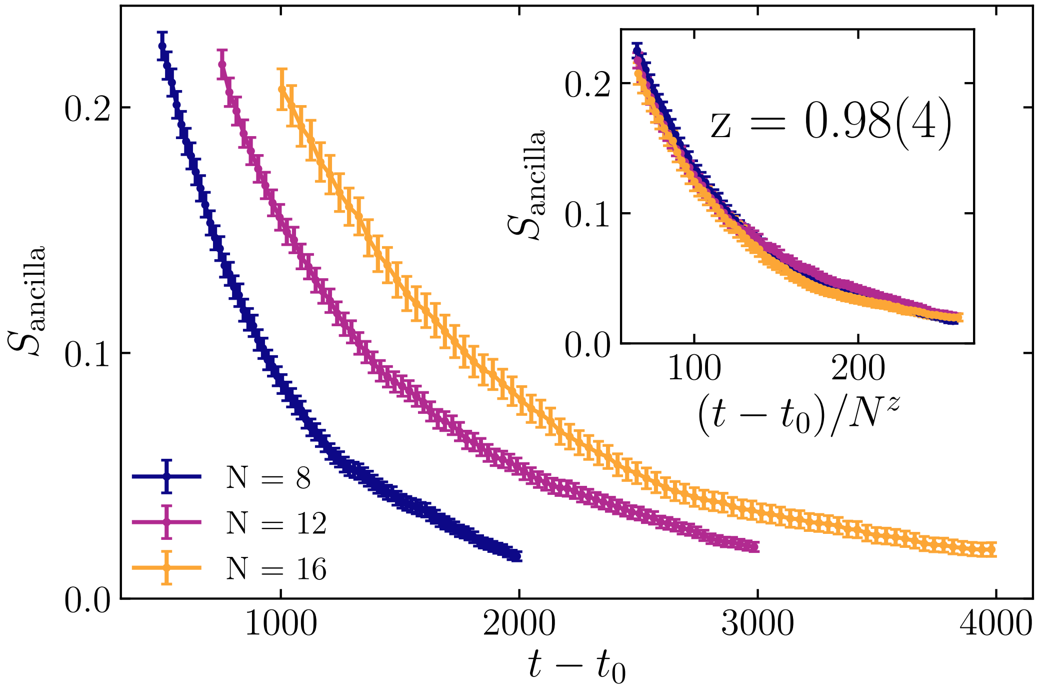

**Figure 4.9:** Extracting the dynamical critical exponent $z = 0.98(4)$ using the entanglement entropy of an ancilla qubit as an order parameter for the transition [72, 85]. The ancilla is maximally entangled with the bulk system at the saturation time $t_0$ determined by the dynamics of $I_3$, and then we continue with the dynamics described in Section 4.1 (acting only on the original spins). In performing the data collapse, we exclude times shortly after $t_0$ because the scaling only occurs after an intermediate timescale.

For both of these numerical comparisons, it is important to note that Refs. [68, 72] both use base-2 logs, whereas we use natural logs, so one has to multiply their values by ln 2 to compare.

## 4.4 Discussion

Measurement-induced entanglement transitions represent an interesting new class of phase transition which shine light on the resilience of quantum entanglement against a classicality-inducing environment. They were initially explored for systems at opposite ends of the spectrum of many-body quantum dynamics: chaotic random unitary circuits, and integrable models. In this work we have demonstrated that the nature of the measurement-induced transition in many-body localized (MBL) systems can interpolate between these two extremes, in a way which is consistent with the standard phenomenology of MBL. If the measurements are made in a basis which is scrambled by the MBL dynamics, then the transition from volume- to area-law entanglement occurs at a nonzero measurement probability $p$, similar to previously studied chaotic systems. On the other hand, if the measurements are made in a basis which remains localized by the MBL dynamics, then the volume-law collapses for any nonzero $p$. This distinction does not appear with random unitary circuits, since all local operators are scrambled in time. In MBL systems, the existence of an extensive number of local integrals of motion, the 'l-bits', means that not all local operators are scrambled. Instead, only those operators which have low overlap with the l-bits are scrambled, and it is for these operators that the volume-law will persist for $0 \leq p < p_c$ if measurements are made in the basis of their eigenstates.

One obvious question is how the measurement-induced entanglement transition (MIT) intersects with the MBL transition. At sufficiently low disorder strength $W < W_c$, the Hamiltonian in Eq. (4.1) is chaotic [126, 128], i.e. it satisfies the eigenstate thermalization hypothesis [3, 4]. One might expect the MIT in this chaotic Hamiltonian system with short-range interactions to be in the same universality class as the MIT in random local unitary circuits with the same local Hilbert space dimension. But, from the analysis of the scaling of the critical Rényi entropies in Section 4.3, it appears that the MIT in the MBL phase may be in a distinct universality class to that in Haar-random local unitary circuits. This begs the question of how the conformal field theory describing the MIT critical point changes as one sweeps the disorder strength $W$ across the MBL transition.

It is worth noting that one key difference between the model considered in this paper and random-circuit models is that here there is quenched (spatial) disorder in the unitary part of the dynamics. This is noteworthy because the critical exponent $\nu = 1.3(2)$ we extract violates a naive application of the Harris criterion $\nu \geq 2/d$ with $d = 1$ [132, 133]. This is despite the fact that we observe $z \approx 1$ at the critical point. We speculate two possible reasons for this violation. The first is that the randomness of the measurements in both space and time means that the overall 'disorder' in this problem is no longer quenched, so the Harris criterion may not apply. The second is based on the recent conjecture by Li et al. [76] that the critical points of these hybrid quantum circuits are described by Euclidean CFTs, where the physical time coordinate essentially acts as a second spatial coordinate. In that sense, the Harris criterion may still apply, but with $d = 2$ rather than $d = 1$.

We also discussed in Section 4.3 how X-basis measurements with small but nonzero $p$ can actually *increase* the steady-state entanglement relative to $p = 0$ for initial states with non-maximal diagonal entropy, as a consequence of the increase in diagonal entropy induced by X-basis measurements. This may be somewhat counterintuitive, given the usual picture of measurements destroying entanglement, but suggests the possibility that measurements could be used as a tool to produce states with desirable properties [134], such as high entanglement, in systems where simply evolving with random unitaries is not feasible.

More broadly, there is also the question of how measurements affect the characteristics of phases of pure-unitary dynamics. We have seen, such as in Fig. 4.5, that at least some of the aspects of MBL phenomenology remain preserved in the volume-law phase even for nonzero $p$, such as the monotonic logarithmic growth of entanglement in time. However, it has also been argued [67] that a steady-state volume law stable to $p > 0$ necessarily implies the existence of a subleading logarithmic correction to the volume law, $S(A) \sim \alpha \ln |A| + s|A|$. This has been observed in random Clifford models [70] and appears analytically as an entropic contribution to the free-energy cost of an 'entanglement domain wall' [100], so this is one aspect which is qualitatively modified by the presence of measurements. It would be enlightening to see if such a subleading correction is also present in the steady-state of this hybrid MBL system, but this is likely out of reach of the small system sizes accessible by exact diagonalization. This may therefore be an opportunity for NISQ-era [135] quantum simulators to probe new physics out of the reach of numerics. Direct measurement of the entanglement entropy associated with a single quantum trajectory may be difficult, owing to the need to perform the exponentially many experimental repetitions associated with the postselection of measurement outcomes [74] and the complexity of measuring an entropy [110, 136]. However, there have been proposals for more experimentally feasible probes of the entanglement transition based on the Fisher information [74] and coupled ancilla qubits [85]. It would be interesting to see if these or new techniques could be developed to allow for experimental detection of novel physics, such as the subleading logarithmic corrections to the entanglement entropy, induced by measurements of quantum systems.

# Chapter 5

# Measurement-induced criticality in Clifford circuits

Measurement-induced phase transitions occur in a wide variety of models, including random circuits [66–86], Hamiltonian systems [87–95], and measurement-only models [78, 96–98], and exhibit universal behavior. However, the determination of the relevant universality classes has proved to be a subtle issue. In certain 1+1D systems there is a 'dimensional correspondence', where the measurement-induced transition in the 1+1D quantum system corresponds to an ordering transition in a 2+0D statistical mechanical model. Through these models, it has become clear that there is an important link between measurement-induced transitions and classical percolation, but the precise nature of this relationship is still unclear. For example, for 1+1D Haar-random circuits there are two distinct mappings to 2D percolation: one for the $(n = 0)$-Rényi entropy (Hartley entropy) [68] which employs the minimal cut formalism [137], and another for the $(n \geq 1)$-Rényi entropies [74, 75] which uses the replica-trick to map the problem to 2D percolation in the limit of large local Hilbert space dimension $q \to \infty$.

However, there is both analytical [75] and numerical evidence [72, 76, 138] to suggest that away from this limit the universality class should be distinct from percolation. Puzzlingly, despite this evidence, numerics on 1+1D

Haar-random and Clifford circuits give many *bulk* exponents which are close to those of percolation. It has been suggested [75] that this could be an indication that the finite $q$ fixed point is close to the percolation fixed point in the RG phase diagram.

Despite the results in 1+1D, it was not previously clear whether this proximity to percolation holds in higher dimensions. To address this, in the first part of this chapter we study the critical properties of the measurement-induced transition in 2+1D Clifford circuits. First, we precisely locate the critical point using the tripartite information $I_3$ (see Section 5.2), which has been argued to be scale-invariant at criticality, thereby providing a good estimator of the critical probability $p_c$. Having fixed $p_c$, we then find an inverse power-law for

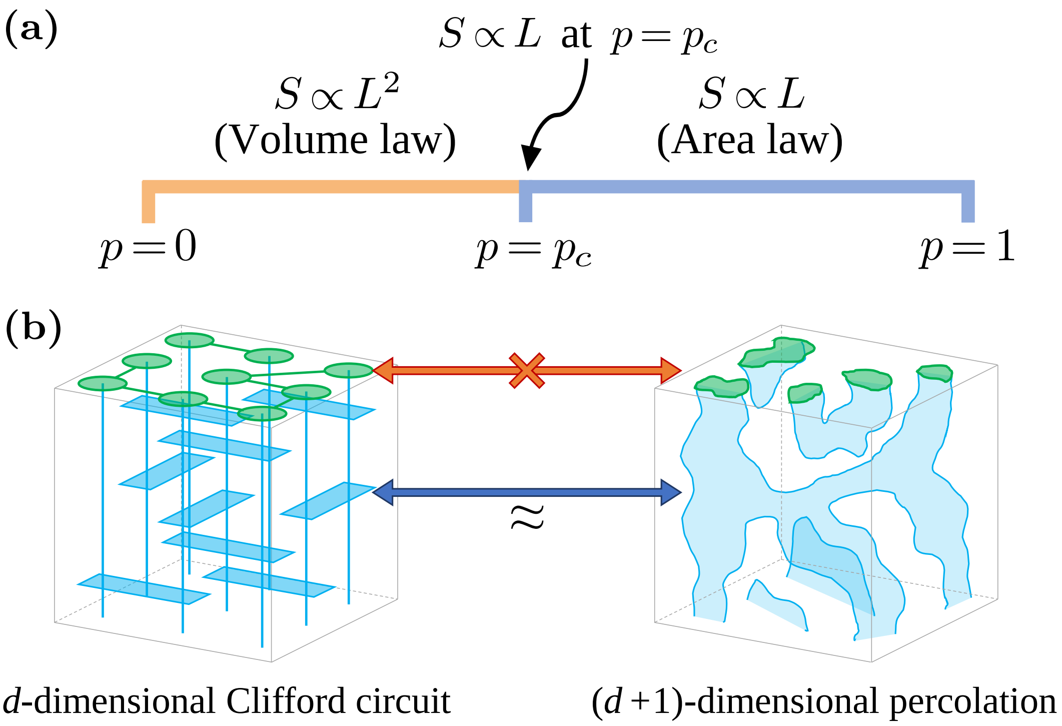
(a)
$S \propto L$ at $p = p_c$
$S \propto L^2$
(Volume law)
$S \propto L$
(Area law)
$p = 0$
$p = p_c$
$p = 1$
(b)
$\approx$
$d$-dimensional Clifford circuit
$(d+1)$-dimensional percolation

**Figure 5.1:** **(a)** Phase diagram for the measurement-induced transition in 2+1D local random Clifford circuits. For measurement probabilities $p < p_c$ the steady state exhibits volume-law entanglement, while for $p \geq p_c$ the steady state is area-law entangled. The entanglement transition and the purification transition coincide. **(b)** The critical point of a $d$-dimensional circuit appears to be described by bulk exponents from the $(d+1)$D percolation. However, entanglement cluster exponents do not match the percolation surface exponents.

the critical entanglement dynamics, $S(t, L) \sim L(1 - a/t)$, which saturates to an area-law (see Fig. 5.1a). We provide a heuristic justification for this scaling based on the 'minimal cut' prescription, which assumes a percolation-like picture. The steady-state area-law scaling is consistent with the behavior of conformal field theories in dimensions $d > 2$ [63, 64].

We note that the accurate determination of the critical point using $I_3$ was important to correctly determine the critical scaling, since even small deviations can result in scaling which looks like $S \sim \mathcal{O}(L \log L)$ (c.f. Ref. [84] and the discussion in Section 5.B).

Next we analyze the connection between this measurement-induced entanglement transition and quantum error-correction through the lens of the purification transition [73, 74, 80, 85, 139], which is characterized by a transition in the purification time of an initially maximally-mixed state—in the 'mixed phase' the state purifies in a time exponential in system size $L$, whereas in the 'pure phase' it purifies in a time polynomial in $L$. This purification transition can be viewed as a transition in the quantum channel capacity density of the hybrid quantum circuit, which governs whether the circuit can be used to generate a finite-rate quantum error-correcting code—the code rate is finite in the mixed phase, and goes to zero as one approaches the pure phase. In other words, these hybrid quantum circuits can form *emergent* quantum error-correcting codes which protect against errors given precisely by the measurements involved in the circuit.

It is not *a priori* obvious that these two measurement-induced transitions should coincide: the entanglement transition concerns spatial correlations in a quantum state at a fixed time, whereas the purification transition concerns correlations between quantum states at different times [80]. Their coincidence in 1+1D was explained by the fact that the 2+0D statistical mechanical model governing the purification transition is the same as that of the entanglement transition, just with different boundary conditions [74, 76]. In these models,

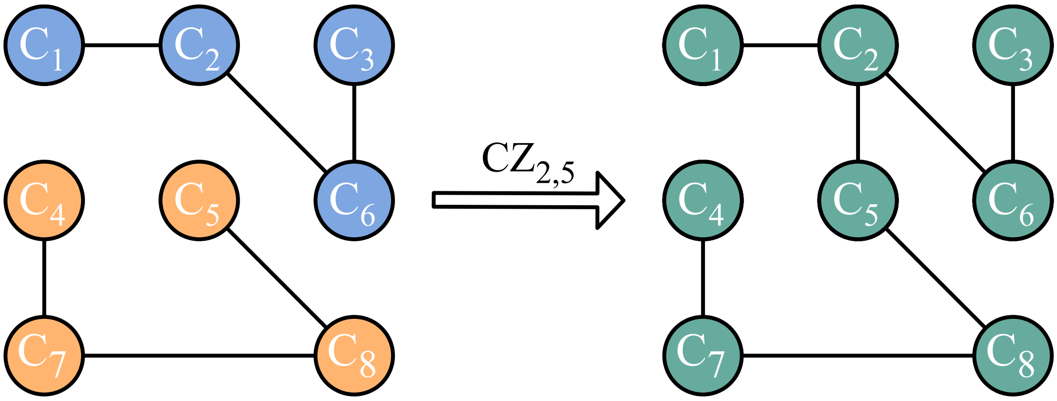

**Figure 5.2:** We employ a graph-state based simulation algorithm [140], where the data encoding the state consists of a graph $\mathcal{G}$ and a list $\{C_i\}_{i=1}^{L^d}$ of one-qubit Cliffords. The entanglement structure is completely fixed by $\mathcal{G}$. Entanglement clusters can be found by a breadth-first search on $\mathcal{G}$, and are here highlighted in different colors. In general the action of a Clifford gate corresponds to updating $\mathcal{G}$ and the list of one-qubit Cliffords. Here we illustrate the simple case of a CZ gate acting on two qubits whose one-qubit Cliffords commute with CZ; in this case the CZ gate simply toggles an edge between the qubits.

the time coordinate of the physical circuit plays the role of imaginary time in the stat-mech model, giving an emergent symmetry between space and time [76]. In higher dimensions, however, the symmetry between space and time can be broken quite naturally. Our precise handle on the critical point allows us to demonstrate that the purification transition in 2+1D Clifford circuits continues to coincide with the entanglement transition, suggesting this phenomenon may be generic in all dimensions.

The coincidence of these two transitions then allows us to utilize the entangling and purifying dynamics of entangled ancilla qubits to extract various bulk and surface critical exponents of the transition in 2+1D Clifford circuits, and to provide evidence of conformal symmetry at the critical point (see Section 5.3). The *bulk* exponents extracted in this way are within error-bars of 3D percolation (see Table 5.1). Interestingly, we do observe small deviations from percolation in certain surface critical exponents (see Section 5.3). This is similar to the behavior observed numerically in 1+1D circuits with qubits [72, 76, 85].

| Exponent | Quantum circuits | | Classical percolation | | |
|---|---|---|---|---|---|
| | 1+1D C | 2+1D C | 1D P | 2D P | 3D P |
| $\nu$ | 1.24(7) | 0.85(9) | 1 | 4/3 = 1.333 | 0.8774 |
| $\eta$ | 0.22(1) | −0.01(5) | 1 | 5/24 = 0.208 | −0.047 |
| $\eta_{\parallel}$ | 0.63(1) | 0.85(4) | 1 | 2/3 = 0.667 | 0.95 |
| $\eta_{\perp}$ | 0.43(2) | 0.46(8) | 1 | 7/16 = 0.438 | 0.45 |
| $\beta$ | 0.14(1) | 0.40(1) | 0 | 5/36 = 0.139 | 0.43 |
| $\beta_s$ | 0.39(2) | 0.74(2) | 0 | 4/9 = 0.444 | 0.85 |
| $z$ | 1.06(4) | 1.07(4) | | | |
| | | Entanglement clusters | | | |
| $\beta_{ec}/\nu$ | -0.009(2) | 0.00(2) | | | |
| $\beta_s/\nu$ | | | 0 | 1/3 = 0.333 | 0.974 |
| $\beta/\nu$ | | | 0 | 5/48 = 0.104 | 0.49 |
| $\gamma_{ec}/\nu$ | 0.95(1) | 1.84(2) | | | |
| $\gamma_{1,1}/\nu$ | | | 0 | 1/3 = 0.333 | 0.060 |
| $\gamma/\nu$ | | | 1 | 43/24 = 1.792 | 2.09 |
| $\tau$ | 2.04 | 1.98(1) | 2 | 187/91 = 2.055 | 2.19 |

**Table 5.1:** Critical exponents of the measurement-induced transition in hybrid 1+1D and 2+1D random Clifford circuits, compared with those of 1D, 2D and 3D percolation (1D P, 2D P, and 3D P respectively). Exponents which appear to differ from percolation are highlighted in red. Those exponents which describe the scaling of entanglement clusters are labelled by the subscript $ec$, and are compared with the bulk and surface exponents for percolation. The exponents for 1+1D Clifford circuits, excluding those describing entanglement clusters, are taken from Ref. [72].

We perform our simulations using a graph-state based algorithm (see Fig. 5.2) [140], which provides easy access to geometric information about the entanglement structure—the entanglement is completely fixed by the underlying graph. This allows us to employ graph-theoretic clustering tools to analyze *entanglement clusters* in the steady-state (see Section 5.4). If we naively assume that the critical point has a simple geometric map to percolation, then the critical properties of these entanglement clusters should be governed by the *surface* exponents of percolation, given that the clusters exist on the final timeslice of the $(d + 1)$-dimensional bulk. To confirm this naive expectation, we first analyze entanglement clusters in the projective transverse field Ising model, which is a measurement-only Clifford model known to have a simple geometric map to percolation [92]. There we indeed find critical scaling of the entanglement clusters consist with surface percolation exponents.

However, moving on to the Clifford circuits, we find that, both in 1+1D and 2+1D, the entanglement clusters are governed by exponents significantly different from those of surface percolation (see Fig. 5.1b). We interpret this as further evidence that the measurement-induced transition in qubit Clifford circuits is in a different universality class to percolation. Lessons from Haar-random circuits also tell us that, even when a map to percolation does exist, it may be highly non-trivial in nature, occurring for example only in a replica limit [74, 75]. The deviation from surface percolation exponents in the Clifford models indicates that, even if a map to percolation does exist in certain limits, it may not have such a simple geometric interpretation as do the analogous maps for the projective transverse field Ising model [92] and the Hartley entropy in Haar-random circuits [68].

## 5.1 Methods

### 5.1.1 Model

In Sections 5.2 and 5.3 we study a 2+1D model of local random Clifford dynamics interspersed with random projective measurements. Each time step consists of a round of random 2-qubit Clifford gates with disjoint support applied to nearest-neighbors, followed by a round of projective measurements in the $\sigma^z$ basis, where each qubit has probability $p$ of being measured. The gates are drawn uniformly over the whole 2-qubit Clifford group. The pattern of gates applied at a given time step is determined by two indices: a ‘sublattice index’, which takes values in $\mathbb{Z}_2$, and a ‘clock index’, which takes values in $\mathbb{Z}_4$. Arranging the qubits in an $L \times L$ square lattice with periodic boundary conditions, the sublattice index determines which sublattice of qubits will act as the ‘controls’ for the Clifford gates (see Fig. 5.3a). Given a choice of sublattice, the clock index then determines which direction the Clifford gates act in relative to the control qubits. The values 0, 1, 2, and 3 correspond to gates acting up, right, down, and left from the control qubits respectively (see

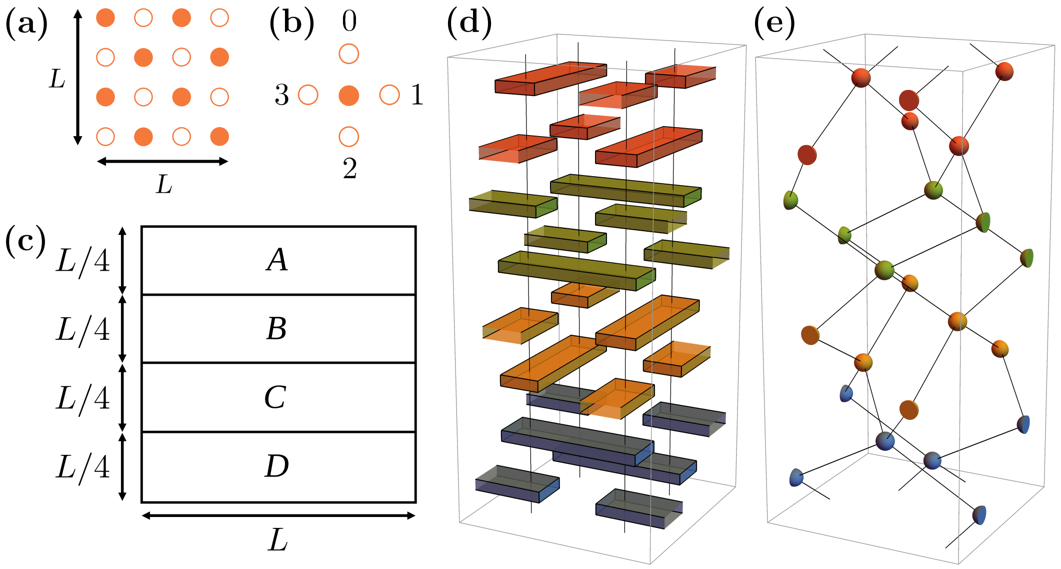

**Figure 5.3:** **(a)** The sublattice index determines which sublattice of qubits, denoted by ● or ○, are used as the 'controls' for the Clifford gates in that time step. **(b)** Given a choice of sublattice index, the clock index determines in which direction each Clifford gate acts relative to the control. **(c)** The geometry used to calculate the tripartite information $I_3(A : B : C)$. **(d)** One period of the gate sequence on a $2 \times 2$ lattice with periodic boundary conditions, and time moving in the vertical direction. Different colors label different values of the clock index. **(e)** Unit cell of the underlying lattice structure, obtained by contracting each Clifford gate into a point.

Fig. 5.3b). At the $n$th time step, the sublattice index has the value $n \pmod 2$, and the clock index has the value $\lfloor n/2 \rfloor \pmod 4$, so that the overall gate sequence has period 8 (see Fig. 5.3d). Since the support of the Clifford gates changes with each time step, certain quantities that depend on making a 'cut', such as the entanglement entropy of a given region, exhibit a mild periodicity related to how often the gates cross the cut. To get well-defined steady-state values, we perform a window-average over a window matching the period of the oscillations (equal to 4 time steps in this case)—all quantities in this paper have been averaged in this way.

It is worth noting that this choice of gate protocol is by no means unique. On grounds of universality, we expect the main effect of a different choice of local quantum circuit is to change the critical measurement probability $p_c$, with the critical exponents unaffected. One alternative was explored in

Ref. [84], which used 4-local gates instead of our 2-local gates. For rank-1 measurements, they observe a critical probability of $p_c \approx 0.54$, which is roughly the square root of our estimated value of $p_c \approx 0.312(2)$. They do observe a different correlation length exponent $\nu$, on which we comment in Section 5.2.

In Section 5.4, as well as studying the 2+1D Clifford model we have just outlined, we also study a 1+1D Clifford model. This is identical to that studied in many previous works studying the 1+1D problem, and can be thought of as being controlled by a single ‘sublattice index’, resulting in a ‘brick-wall’ structure of alternating layers of Clifford gates interspersed with random projective measurements.

### 5.1.2 Simulation method

To simulate the hybrid Clifford dynamics, we used a graph-state based algorithm [140]. This makes use of the remarkable fact that every stabilizer state can be represented as a graph state, up to the action of some 1-qubit Cliffords [141]. Simulation of stabilizer states then takes the form of updating the underlying graph structure and the list of 1-qubit Cliffords, which can be done in polynomial time.

In more detail, graph states are a class of pure quantum states whose structure is determined entirely by an underlying graph $\mathcal{G} = (V, E)$. Each graph vertex $v \in V$ corresponds to a qubit, and the graph edges $E$ determine the preparation procedure for the state. To prepare the graph state $|\mathcal{G}\rangle$, we start from the initial product state $|\psi_0\rangle = [(|0\rangle + |1\rangle)/\sqrt{2}]^{\otimes N}$, where $N$ is the number of qubits, and then apply a CZ gate to each pair of qubits which are connected by an edge in the graph $\mathcal{G}$.

Stabilizer states are the states which can be prepared from the initial product state $|0\rangle^{\otimes N}$ by acting with gates from the $N$-qubit Clifford group $\mathcal{C}_N$. The set of stabilizer states is larger than that of graph states, but not by much: all stabilizer states can be written as a graph state, up to the action of some gates from the 1-qubit Clifford group $\mathcal{C}_1$ [which contains only 24 gates, up to phase]. Single qubit gates are then trivial to perform, taking $\Theta(1)$ time. Two-qubit Cliffords take time $\mathcal{O}(d^2)$, where $d$ is the maximum vertex degree of the qubits involved in the gate, and single-qubit Z-basis measurements take time $\mathcal{O}(d)$. This makes graphs with low connectivity, which can roughly be identified with low entangled states, easier to simulate.

To wit, the graph structure completely determines the entanglement of the corresponding quantum state. Given a bipartition of the system into subsystems $A$ and $B$, the (Rényi or von Neumann) entanglement entropy $S_A$ is given by

$$S_A = \text{rank}(\Gamma_{AB}), \tag{5.1}$$

where $\Gamma_{AB}$ is the submatrix of the adjacency matrix characterizing edges between subsystems $A$ and $B$ [141]. We note that for stabilizer states all Rényi entropies (including the von Neumann entropy) are equal [142].

To simulate an initially mixed state $\rho$, we introduce an auxiliary system to obtain a purification of $\rho$. We then perform time-evolution on the resultant pure state, with the quantum circuit acting as the identity on the purifying system. For the maximally-mixed initial state on $N$ qubits, $\rho = \mathbb{1}/2^N$, this corresponds to the pure state simulation of $N$ Bell pairs, where the system dynamics acts only on one half of the Bell pairs. This purification simulation method does mean that $N$-qubit mixed states are harder to simulate than $N$-qubit pure states, but not as hard as $2N$-qubit pure states, since the purifying qubits typically have a lower vertex degree than the original qubits.

### 5.1.3 Transition diagnostics

As well as the entanglement entropy $S_A$, we also study the tripartite mutual information

$$I_3(A:B:C) = I_2(A:B) + I_2(A:C) - I_2(A:BC), \tag{5.2}$$

where $I_2(A:B) = S_A + S_B - S_{AB}$ is the mutual information. It is easy to see that for pure states, given a partition of the system into 4 subsystems, the tripartite information of 3 of the subsystems does not depend on the choice of subsystems, so from now on we will simply write $I_3 \equiv I_3(A:B:C)$. We calculate $I_3$ for the partition shown in Fig. 5.3c. Notice that a vertical slice of this geometry gives a circle divided into four equal sections. In 1+1D this partitioning was successfully employed to study the entanglement transition because, at least within the minimal cut picture [137], it cancels out any boundary terms corresponding to the entanglement cost of a domain wall traversing from the circuit boundary to the percolating cluster in the bulk of the circuit [72, 80]. This then suggests that in 1+1D, $I_3$ is extensive in the volume-law phase, $\mathcal{O}(1)$ at criticality, and zero in the area-law phase. In 2+1D, we argue that, for this particular choice of geometry, $I_3$ remains $\mathcal{O}(1)$ at criticality, with its overall behavior described by

$$I_3(p,L) = \begin{cases} \mathcal{O}(L^2), & p < p_c \\ \mathcal{O}(1), & p = p_c \\ 0, & p > p_c \end{cases} \tag{5.3}$$

This implies that the values of $I_3(p,L)$ should coincide for different system sizes at $p = p_c$, allowing for reliable location of the critical point. We further discuss our choice of geometry for $I_3$ in Section 5.B.

## 5.2 Entanglement transition

To accurately estimate the location of the critical point, it is necessary to determine the correct scaling of $I_3$. To that end, we must rule out plausible scalings which are different from the one proposed in Eq. (5.3). We have also investigated the possibility that $I_3 \propto L$ at the critical point, which would suggest that the values of $I_3(p,L)/L$ should coincide at $p = p_c$. We detail evidence against this scaling form in Section 5.A.

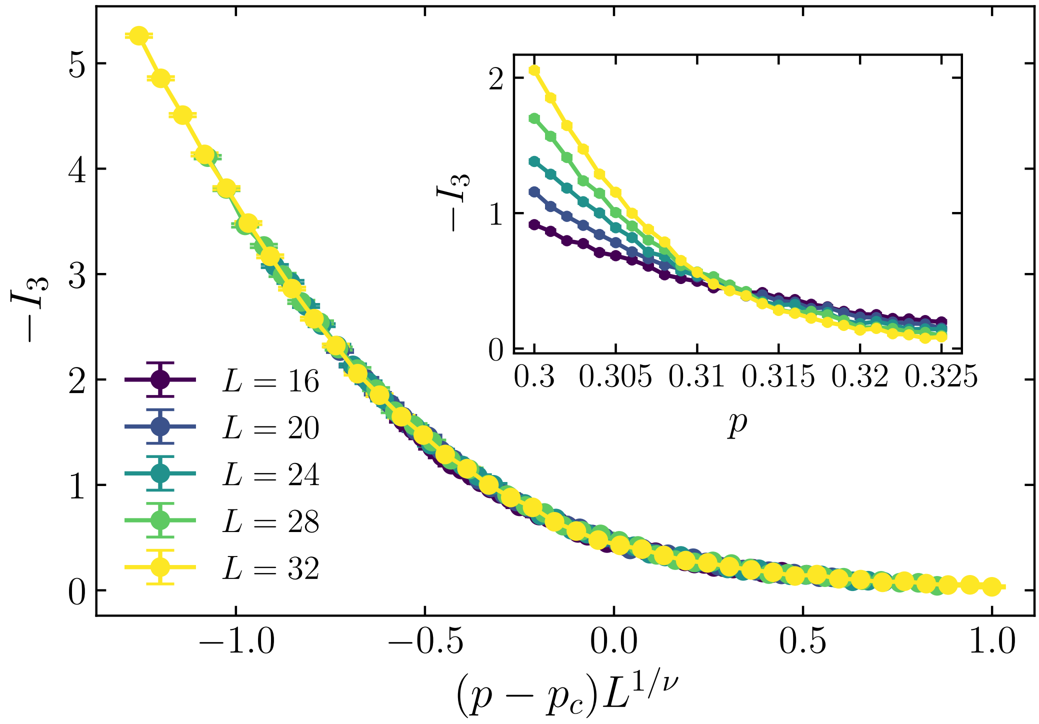

**Figure 5.4:** The steady-state $I_3$ as a function of $(p - p_c)L^{1/\nu}$, where $p_c \approx 0.312(2)$ and $\nu \approx 0.85(9)$. The inset shows the uncollapsed data. This dataset consists of $5 \times 10^4$ circuit realizations.

The steady-state values of $I_3(p, L)$ are plotted in Fig. 5.4. Given the scaling in Eq. (5.3), the curves should coincide at the critical point. To determine the critical point and the correlation length exponent $\nu$ we make the finite-size scaling ansatz

$$I_3(p, L) \sim F\left[(p - p_c)L^{1/\nu}\right], \tag{5.4}$$

where $F[\cdot]$ is a single-parameter scaling function. We determine the optimal parameters by minimizing a cost function $\epsilon(p_c, \nu)$ which measures deviations of a point from a linear interpolation between its neighbors [72, 143] (see Section 5.B for details). The resulting data collapse is of excellent quality, with $p_c \approx 0.312(2)$ and $\nu \approx 0.85(9)$, where the error bars correspond to the range of values for which the cost function is less than 2 times its minimum value. We note that this value of $\nu$ is reasonably close to the 3D percolation value of $\nu_{\text{perc}} \approx 0.877$ [144], suggesting that the close relationship between exponents of the entanglement transition and percolation, even at low local Hilbert space dimension, continues to hold in 2+1D. We also note that our value of $\nu$ is significantly larger than that reported in Ref. [84] ($\nu \approx 0.67$); we attribute this to the fact that we extract $\nu$ by a data collapse not of the half-plane entanglement but of the tripartite information, which coincides for different system sizes at the critical point and so provides a much more accurate estimator of the critical point. A similar scenario occurs in 1+1D [72]. We discuss this further in Section 5.B.

Let us briefly comment on the value of $p_c \approx 0.312$ obtained for the critical measurement probability. This value coincides with the threshold for site percolation on the simple cubic lattice [145], but as far as we are aware this is a coincidence; in fact our gate model maps to the lattice shown in Fig. 5.3e, which exhibits a bond percolation transition at $p_c = 0.3759(2)$. We expect other gate models to give different values of $p_c$ (see Ref. [84]) but the same critical exponents. It is also interesting to compare our value of $p_c$ to the upper bound derived in Ref. [73], which modeled the volume-law phase as forming a dynamically-generated non-degenerate quantum error-correcting code, allowing them to apply the quantum Hamming bound. The bound on $p_c$ depends only on the local Hilbert space dimension $q$ (not on the spatial dimension), and for $q = 2$ gives $p_c \lesssim 0.1893$. While this bound was satisfied by 1+1D Haar-random and Clifford circuits ($p_c \approx 0.17$ [72]), here we see that it is strongly violated in 2+1D Clifford circuits. A similar violation has also been observed in all-to-all models [80], where it was pointed out that if these hybrid dynamics which violate this upper bound are to generate quantum error-correcting codes, these codes must be *degenerate*. Finally, we note that the value of $I_3$ at criticality, $I_3^{2+1D}(p_c) = -0.47(8)$, is within error-bars of the value for 1+1D Clifford circuits, $I_3^{1+1D}(p_c) = -0.56(9)$ [72], suggesting the possibility that at criticality $I_3$ could reach an $\mathcal{O}(1)$ constant which is independent of dimension.

Having established the location of the critical point via finite-size scaling of $I_3$, we study the scaling properties of the entanglement entropy in the different phases. We propose the following scaling for the 2+1D circuit:

$$S(p,L) \sim \begin{cases} L(1-\frac{a}{\xi}) + A\frac{L^2}{\xi^2}, & p < p_c, \\ L, & p = p_c, \\ L(1-\frac{a}{\xi}), & p > p_c, \end{cases} \tag{5.5}$$

where $\xi = |p - p_c|^{-\nu}$ is the correlation length and $a, A$ are unknown constants. Such scaling implies the data collapse of the entropy is possible using a similar ansatz as in the 1+1D circuit [68, 70],

$$S(p,L) - S(p_c,L) = F[(p-p_c)L^{1/\nu}], \tag{5.6}$$

where $F[\cdot]$ is a single-parameter scaling function, depending only on $L/\xi$.

In order to see the origin of this proposed scaling form, we draw from the similarity to the 1+1D case, where the behavior of entropy can be intuitively understood by considering the Hartley entropy $S_0$. For Haar random circuits $S_0$ can be mapped exactly to classical percolation in 2D [68]: each projective measurement cuts a bond of the underlying lattice and prevents percolation; Hartley entropy of a region is then calculated as the minimal number of cuts needed to separate said region at the final-time boundary from the rest of the circuit. This mapping extends naturally to $d$+1D circuits, where $S_0$ corresponds to a minimal-cut $d$-dimensional membrane. Near criticality, the 'nodes-and-links' picture of percolation [146, 147] gives an insight into the scaling properties of $S_0$ (see Fig. 5.5) and shows two important contributions: from the bulk, and from the edge.

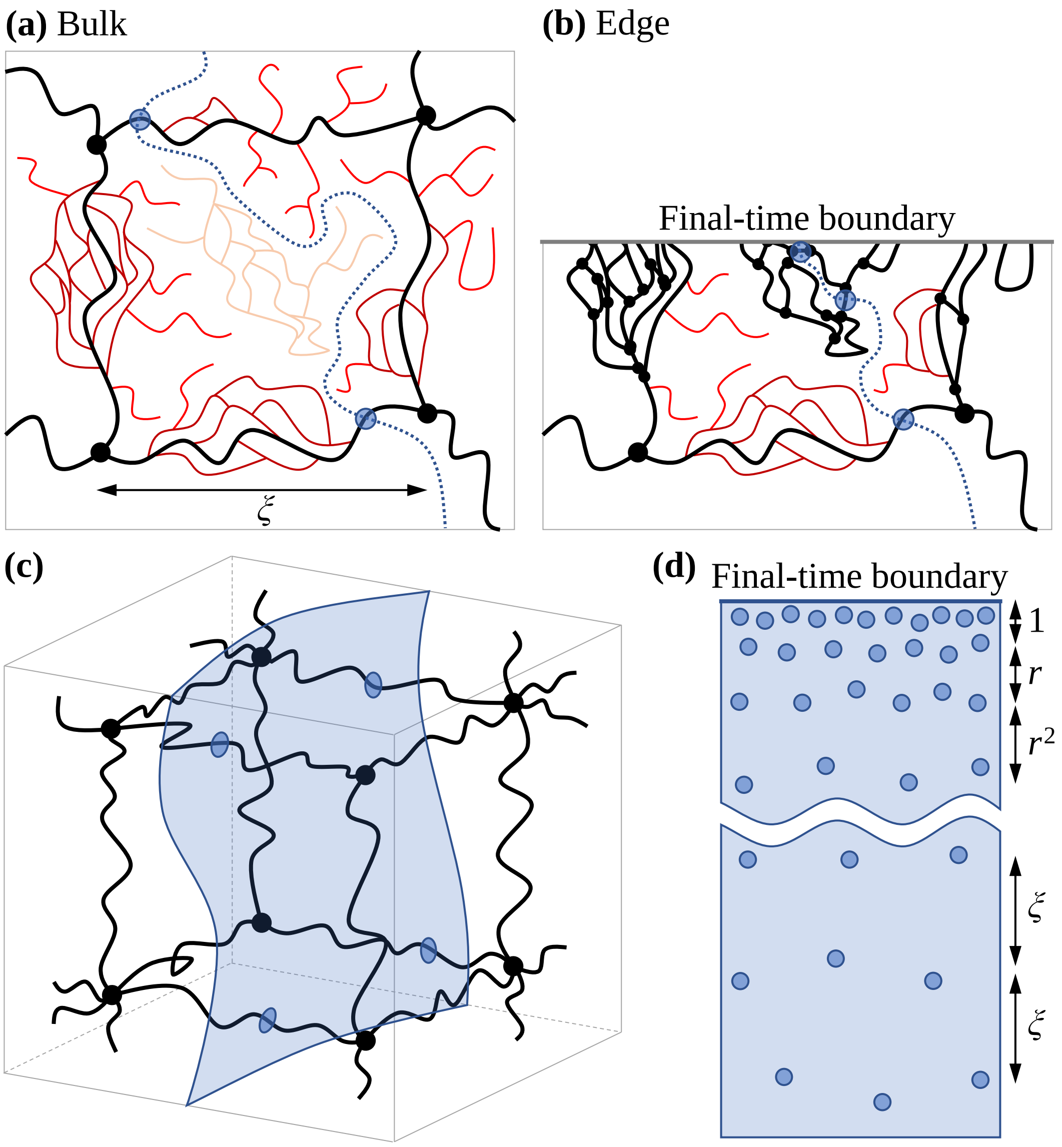

**Figure 5.5:** 'Nodes and links' picture of percolation. **(a)** An example of percolation in the bulk of a 2D system. Percolating bonds cluster within nodes (black dots) connected by links (thick black lines), forming a 'wire frame'. Average distance between nodes is the correlation length $\xi$. There are also smaller structures on the links (dark red), dead ends (red) and structures unconnected to the frame (orange). Minimal-cut path (blue dotted line) can be deformed to only cut through the links (cuts indicated by transparent blue circles), causing an $O(1)$ contribution to the entropy. **(b)** The same example, but in the presence of the final-time boundary. Every structure touching the edge is promoted to be part of the frame. Minimal-cut path generically starts within a smaller structure of size $O(1)$, having now to traverse through larger and larger chambers in order to reach structures of size $\xi$. **(c)** Percolation in the bulk of a 3D system (showing only nodes and links for simplicity). Minimal-cut membrane can be deformed, contributing $O(1)$ to the entropy per one cell of the frame. **(d)** Flattened minimal-cut membrane, showing all the necessary cuts. Near the edge, the membrane traverses layers of structures of increasingly larger sizes (with approximate common ratio $r$).

For $p < p_c$, percolation in the bulk of the circuit is possible due to unbroken bonds forming a ‘wire frame’ consisting of dense clusters of bonds (nodes) connected by long chains of unbroken bonds (links). Each cell in the frame is of the size of the correlation length $\xi$ and, if traversed by the minimal-cut membrane, gives a contribution of $O(1)$ to the entropy [see Fig. 5.5(a) and (c) for 2D and 3D examples]. Counting the number of cells results in the bulk of the circuit contributing $\sim (L/\xi)^d$ to $S_0$, the source of the volume-law scaling.

The second relevant contribution comes from the final-time boundary of the circuit [see Fig. 5.5(b)]. This edge cuts through not only the links and nodes discussed above, but also through smaller structures, dead ends, and other structures normally unconnected to the main mesh. This results in the minimal-cut membrane having to generically cut through a large number of small mesh cells right next to the boundary, then through layers of consecutively larger cells, until the cell size reaches $\xi$ [see Fig. 5.5(d)]. Assuming a geometric progression of cell sizes with common ratio $r > 1$ [68], the number of cells in the $i$th layer is $\sim (L/r^i)^{d-1}$, while the total number of layers is $\sim \log_r \xi$. We then arrive at an important result: the total contribution from the boundary for 1+1D is $\sim \log \xi$, while for higher dimensions is $\sim (1 - a/\xi^{d-1})L^{d-1}$. This term is in general responsible for the area-law scaling, but at the critical point $p = p_c$ (when $\xi \rightarrow L$) it results in *logarithmic* scaling in 1+1D, and *area-law* scaling in higher dimensions.

We can also use this analysis to predict the time-dependence of the entanglement entropy at criticality. For intermediate times $1 \ll t \ll \min(\xi, L)$, the circuit is shallow, and the minimal cut membrane will pass from the final time boundary to the initial time boundary. This is because at $t = 0$ the system is in a product state and the membrane can traverse the initial boundary freely. Hence, the main contribution to the entropy will be from summing over progressively larger cells up until the circuit depth of $t$, i.e. the number of layers is now only $\sim \log_r t$. Thus, the geometric sum $\sum_i^{\log_r t} (L/r^i)^{d-1}$ gives

$$S(t, L) \sim L^{d-1}\left(1 - \frac{a}{t^{d-1}}\right) \tag{5.7}$$

for some $\mathcal{O}(1)$ constant $a$. For the special case of $d = 1$ the sum reduces to the logarithmic scaling $S(t, L) \sim \log t$ [68], but in higher dimensions the growth takes the form of an inverse power-law in time, eventually saturating to an area-law. We can write this as a scaling form $S(t, L) - bL^{d-1} \sim f(t/L)$ with $f(x) \sim -x^{-(d-1)}$ as $x \to 0$ and $f(x) \to$ const. as $x \to \infty$, consistent with a dynamical critical exponent of $z = 1$ (see also Fig. 5.7b and Fig. 5.C1c).

Fig. 5.6 presents a summary of our results for the entanglement entropy, showing an excellent agreement with the scaling ansatze in Eqs. (5.5) and (5.7). Notably, in the steady state we observe *area-law* scaling at the critical point (consistent with the recent results of Ref. [98]), possibly with subleading *additive* logarithmic corrections, but *not* with multiplicative logarithmic corrections ($L \log L$), as implied in Ref. [84]. We note however that if one assumes a lower transition point ($p \approx 0.29$), numerics may seem like a $L \log L$ behavior for small system sizes, suggesting that correctly locating the critical value $p_c$ is crucial to making any statements on scaling of entropy at criticality. As explained above, data collapse of $I_3$ pinpoints the precise value of $p_c$, allowing us to determine the correct critical scaling behavior.

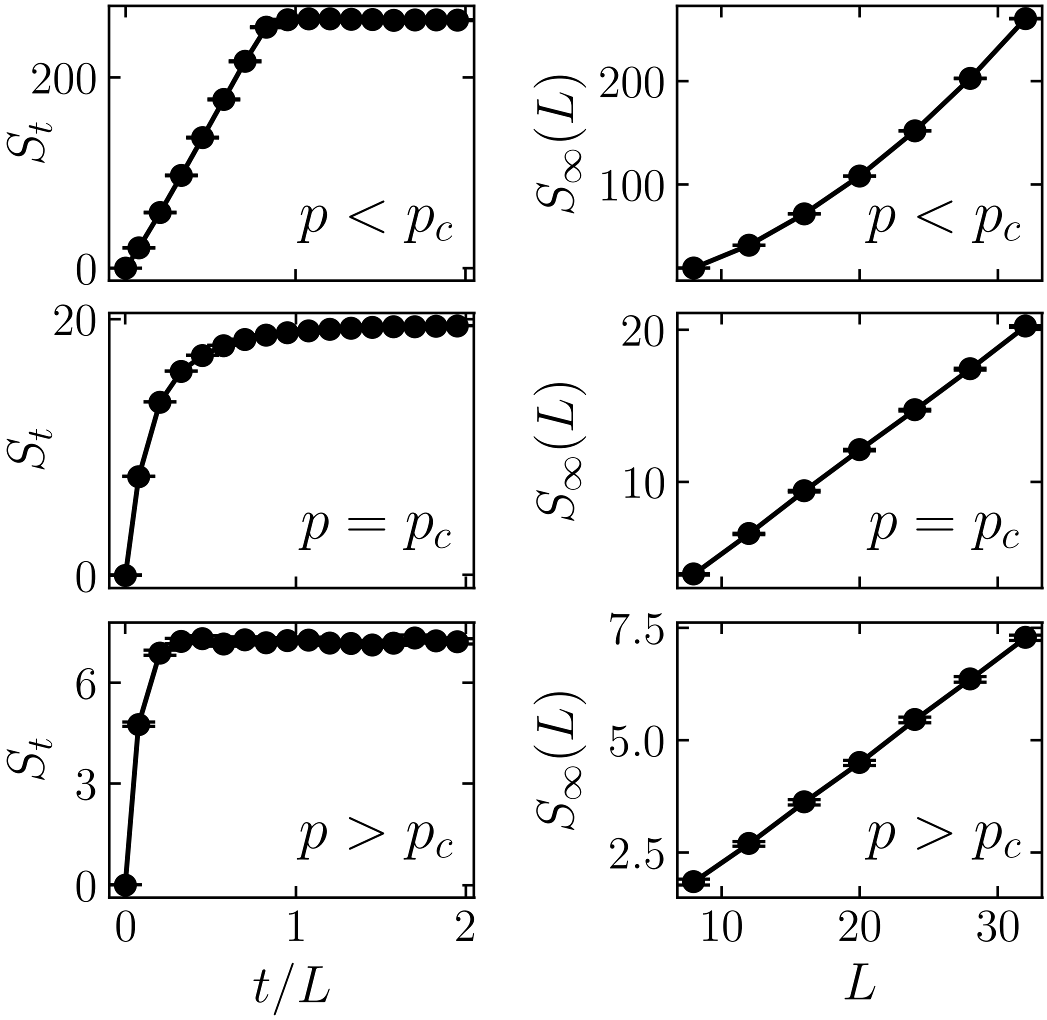

**Figure 5.6:** Dynamics and steady-state behavior of the half-plane entanglement $S(L/2 \times L)$ in the volume-law ($p < p_c$), critical ($p = p_c$), and area-law ($p > p_c$) phases. The left column shows the dynamics for $L = 32$, with $S_t \sim Lt$ for $p < p_c$, $S_t \sim L(1 - a/t)$ for $p = p_c$, and $S_t$ saturating in $\mathcal{O}(1)$ time for $p > p_c$. The right column shows the steady-state scaling, with $S_\infty(L) \sim \mathcal{O}(L^2)$ for $p < p_c$, and $S_\infty(L) \sim \mathcal{O}(L)$ for $p \geq p_c$. We use $p = 0.1$, $p = 0.312$, and $p = 0.4$ for the volume-law, critical, and area-law plots respectively.

Moreover, at these system sizes we cannot directly observe the presence of a subleading additive $\log L$ term, but we also cannot rule it out since it may have a small coefficient. Such a subleading additive $\log L$ is predicted by a calculation from capillary wave theory [100, 148] which evaluates the free energy cost of inserting an Ising domain wall membrane in the quantum circuit's spacetime bulk, with the boundary condition that at the boundary of the circuit corresponding to the final time the membrane is pinned to the region for which one wants to calculate the entanglement entropy. The subleading $\log L$ then corresponds to an entropic contribution to the free energy from 'thermal' fluctuations of the membrane at finite 'temperature' (here corresponding to nonzero measurement probability). In general, the appearance at criticality of an area-law with additive log corrections is reminiscent of the behavior of higher-dimensional conformal field theories [63, 64]. There is also the possibility of a sublinear power-law correction, analogous to the $\sim L^{0.38}$ correction observed numerically in 1+1D Clifford circuits [100], which could indicate a more complex entanglement domain wall structure than the simple Ising structure that predicts the logarithmic correction.

Finally, regarding the critical entanglement dynamics, we note that one must be careful to distinguish the inverse power-law behaviour of Eq. (5.7) from logarithmic growth. In Section 5.C we provide a plot of the critical entropy dynamics at $L = 92$ on a log scale, which demonstrates that the growth is not logarithmic in time, and provide further evidence for the inverse power-law scaling.

## 5.3 Purification transition

In this section, we investigate the purification transition and demonstrate that it coincides with the entanglement transition studied in Section 5.2. To do so we study the entanglement entropy density $S/L^2$ of a maximally-mixed initial state after being time-evolved for time $t = 4L$. In the 'pure phase', the state purifies in time linear in system size $L$, implying $S/L^2 \longrightarrow 0$ for $t \propto L$ but sufficiently large ($t = 4L$ suffices), while in the 'mixed phase' the purification time is exponential in $L$, so that after the time $t = 4L$ we expect the entropy density to remain finite. Fig. 5.7 shows the entanglement entropy density as a function of measurement probability $p$. The entropy density vanishes close to the critical point $p_c \approx 0.312$ of the entanglement transition. For these system sizes, there still exists some appreciable finite-size drift, but it appears to be such that the entropy density vanishes increasingly close to $p_c \approx 0.312$ as the system size increases. The black dashed curve shows the function $A(p_c - p)^{2\nu}$, with $A$ a constant and $p_c$ and $\nu$ fixed from the entanglement transition. The exponent $2\nu$ is motivated by the scaling of the entanglement entropy in Eq. (5.5), where the $\mathcal{O}(L^2)$ term controlling the entropy density appears with the coefficient $\xi^{-2} \sim (p_c - p)^{2\nu}$. The convergence of the entropy density to the scaling form $A(p_c - p)^{2\nu}$ therefore provides strong evidence that the purification transition indeed coincides with the entanglement transition and that the estimation of $\nu$ in the previous section is correct.

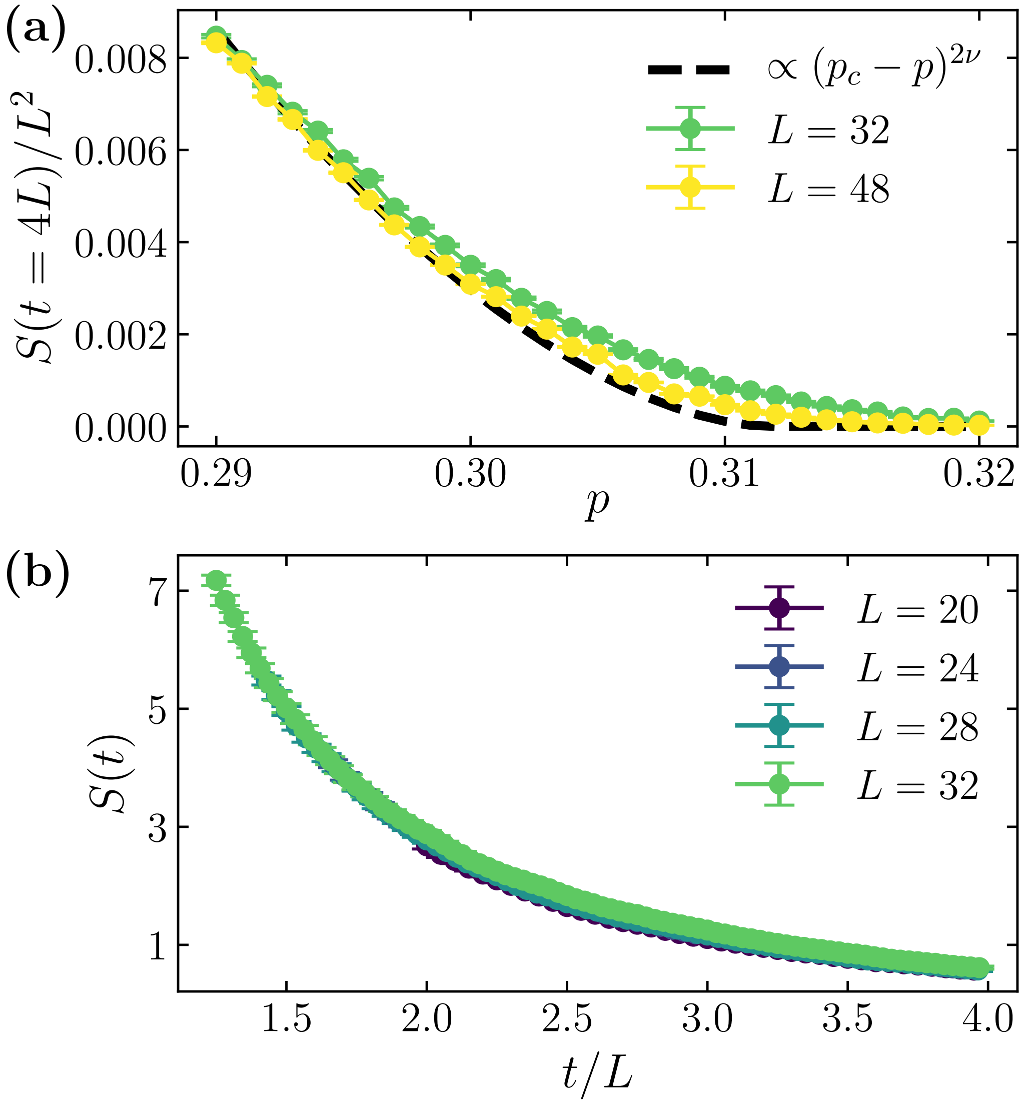

**Figure 5.7:** **(a)** The entropy density of an initially maximally-mixed state after evolving for a time $t = 4L$. The black dashed line shows the function $A(p_c - p)^{2\nu}$ with $A \approx 11.7$, and $p_c$ and $\nu$ determined from finite-size scaling of $I_3$. At these system sizes there is still some finite-size drift in the data, but it seems to be approaching the curve described by $A(p_c - p)^{2\nu}$. **(b)** Purification dynamics at $p = p_c$. The data collapse onto a single curve when plotted in terms of $t/L$, indicating a dynamical critical exponent of $z \approx 1$ [the optimal fitted value is $z = 1.07(4)$]. Non-universal early-time dynamics are excluded from the fit.

Having established the coincidence of these two transitions, we now extract further critical exponents of the transition using the local order parameter proposed in Ref. [85] of the entanglement entropy of an ancilla qubit entangled with the system but not directly acted on by the circuit dynamics. First, we extract the anomalous scaling exponents $\eta$, $\eta_{\|}$, and $\eta_{\perp}$ controlling the power-law decay of bulk-bulk, surface-surface, and surface-bulk two-point correlation functions at criticality. In percolation, these quantities control the probabilities that two distant sites, living either in the bulk or on the surface, belong to the same cluster. To determine these exponents we study the dynamics at $p = p_c$ of the mutual information between two ancilla qubits separated by a distance $L/2$ [72], which provides an upper bound on connected correlation functions [149]. The ancilla qubits are entangled with the system at a time $t_0$. We use different values of $t_0$ and different boundary conditions to extract the different exponents: $\{t_0 = 2L, \text{periodic}\}$ for $\eta$, $\{t_0 = 0, \text{periodic}\}$ for $\eta_{\|}$, and $\{t_0 = 2L, \text{open}\}$ for $\eta_{\perp}$. Conformal symmetry $z = 1$ at the critical point (see Fig. 5.7b) implies that in $D$ spacetime dimensions the mutual information between two qubits separated by a distance $r$ should assume the scaling form

$$I_2(t,r) \sim \frac{1}{r^{D-2+\eta}}\, G\left[\frac{t-t_0}{r}\right], \tag{5.8}$$

where $G[\cdot]$ is a single-parameter scaling function, and the exponent depends on the choice of $t_0$ and boundary conditions, as outlined above. Thus in this 2+1D spacetime circuit, we can extract the exponents by performing data collapses of $L^{1+\eta} I_2[(t-t_0)/L, L/2]$, as shown in Fig. 5.8. For the bulk-bulk exponent $\eta$ and the surface-bulk exponent $\eta_{\perp}$, we obtain the values $\eta \approx -0.01(5)$ and $\eta_{\perp} \approx 0.46(8)$, which are within error-bars of the 3D percolation values $\eta_{\text{perc}} = -0.047$ and $\eta_{\perp,\text{perc}} = 0.45$ [150]. We note in passing that the data collapse for $\eta_{\perp}$ is not as good quality as that for $\eta$, resulting in larger error bars using the methodology described in Section 5.B. However, there does not appear to be a systematic drift with increasing system size. We attempted to improve the collapse quality by using a large number of circuit realizations ($10^6$ for $\eta_\perp$), but some discrepancy is still evident. This could possibly be a result of $\eta_\perp$ being particularly sensitive to any miscalibration of the critical point $p_c$, despite the precision to which we have pinpointed $p_c$ in this work.

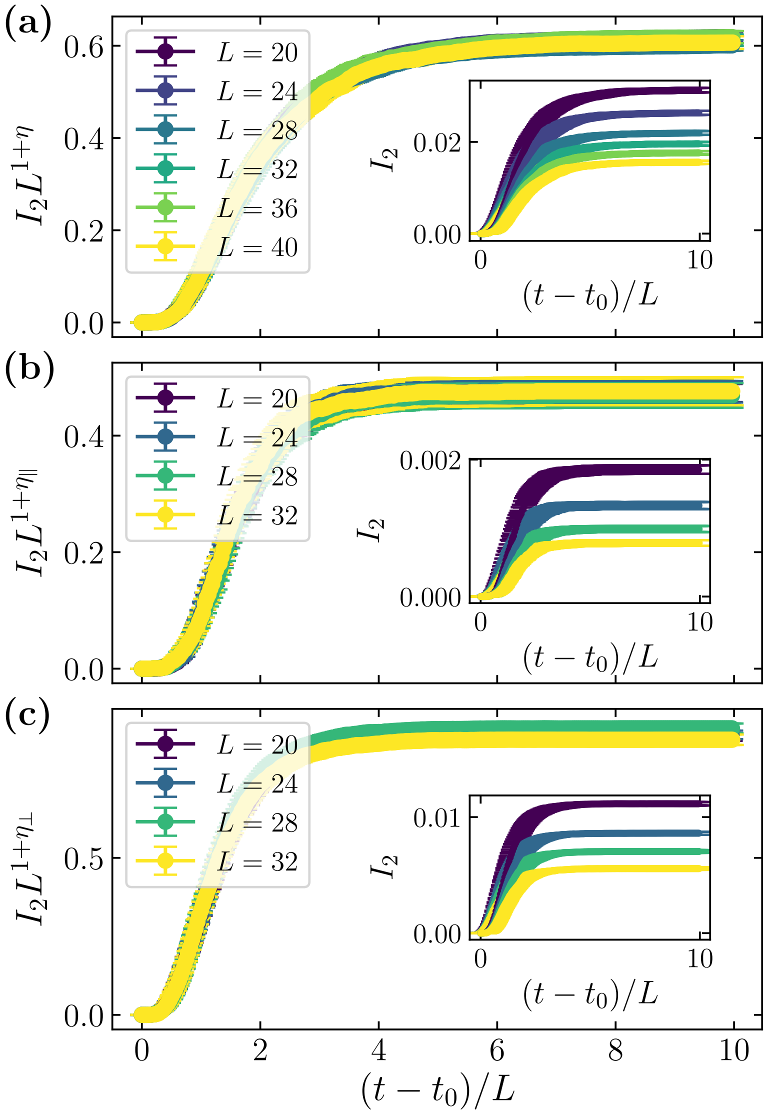

**Figure 5.8:** Extraction of the anomalous scaling exponents $\eta \approx -0.01(5)$, $\eta_\parallel \approx 0.85(4)$, and $\eta_\perp \approx 0.46(8)$, shown in **(a)**, **(b)**, and **(c)** respectively, via data collapse at $p = p_c$ of the mutual information $I_2$ between two ancilla qubits which are entangled at time $t_0$ with two system qubits a distance $L/2$ apart. The different exponents are extracted using different boundary conditions and different values of $t_0$ [see main text]. The insets show the uncollapsed data. The $\eta$ dataset consists of $2.5 \times 10^5$ circuit realizations, while the $\eta_\parallel$ and $\eta_\perp$ datasets each consist of $1 \times 10^6$ circuit realizations.

Moving on to the surface-surface exponent $\eta_{\parallel}$, we obtain the value $\eta_{\parallel} \approx 0.85(4)$. This is *not* within error-bars of the 3D percolation value $\eta_{\parallel,\mathrm{perc}} = 0.95$, indicating a possible difference in surface behavior. The error-bars on our exponent estimates capture only the statistical error, so it is possible that there are still significant finite-size corrections. However, we note that a similar deviation in $\eta_{\parallel}$ (and in $\eta_{\perp}$), was observed in 1+1D Haar-random circuits (though not in Clifford circuits) [72]. In this case, a deviation only in $\eta_{\parallel}$ would not be consistent with the scaling relation $2\eta_{\perp} = \eta + \eta_{\parallel}$, but the error-bars on our estimates are large enough that there could also be small deviations in $\eta_{\perp}$ that provide the necessary contribution to restore the scaling relation.

Next, we extract the exponents $\beta$ and $\beta_s$ controlling the behavior of the order parameter as a function of $p$. In percolation, $\beta$ controls the probability $P(p) \sim |p - p_c|^{\beta}$ that a site in the bulk will belong to the infinite percolating cluster, while $\beta_s$ does the same but for a site on the surface. To extract these exponents we study the entanglement entropy of an ancilla qubit, entangled with the system at time $t_0 = 2L$ for $\beta$ and time $t_0 = 0$ for $\beta_s$, and subsequently time-evolved for a further time $t = 2L$. Fig. 5.9 shows the ancilla entropy $S_{\mathrm{ancilla}}$ as a function of measurement probability $p$ for the cases relevant to $\beta$ and $\beta_s$. For the bulk exponent $\beta$, the data are well described by the function $B(p - p_c)^{\beta}$ with $B$ a constant, $p_c \approx 0.312$ fixed by the entanglement transition, and $\beta \approx 0.40(1)$. This is close to the 3D percolation value of $\beta_{\mathrm{perc}} \approx 0.43$. However, for the surface exponent $\beta_s$, the data are well described by the function $C(p_c - p)^{\beta_s}$, where $\beta_s \approx 0.74(2)$. This is somewhat different from the 3D percolation value of $\beta_{s,\mathrm{perc}} \approx 0.85$. The value of $\beta_s$ is quite sensitive to the value of $p_c$; we estimate that to obtain $\beta_s \approx 0.85$ one would have to have $p_c \approx 0.318$, which does not seem tenable given the clear crossing point in $I_3$ (see inset of Fig. 5.4). There are also some small deviations from the scaling around $p \approx p_c$, but these seem to decrease with system size. We therefore tentatively conclude that the surface critical exponent $\beta_s$ may also differ from 3D percolation. The fact that we observe both the surface exponents $\beta_s$ and

$\eta_\parallel$ to be smaller than the corresponding values from percolation is consistent with the scaling relation $2\beta_s = \nu(D-2+\eta_\parallel)$, where $D = 3$ is the number of spacetime dimensions.

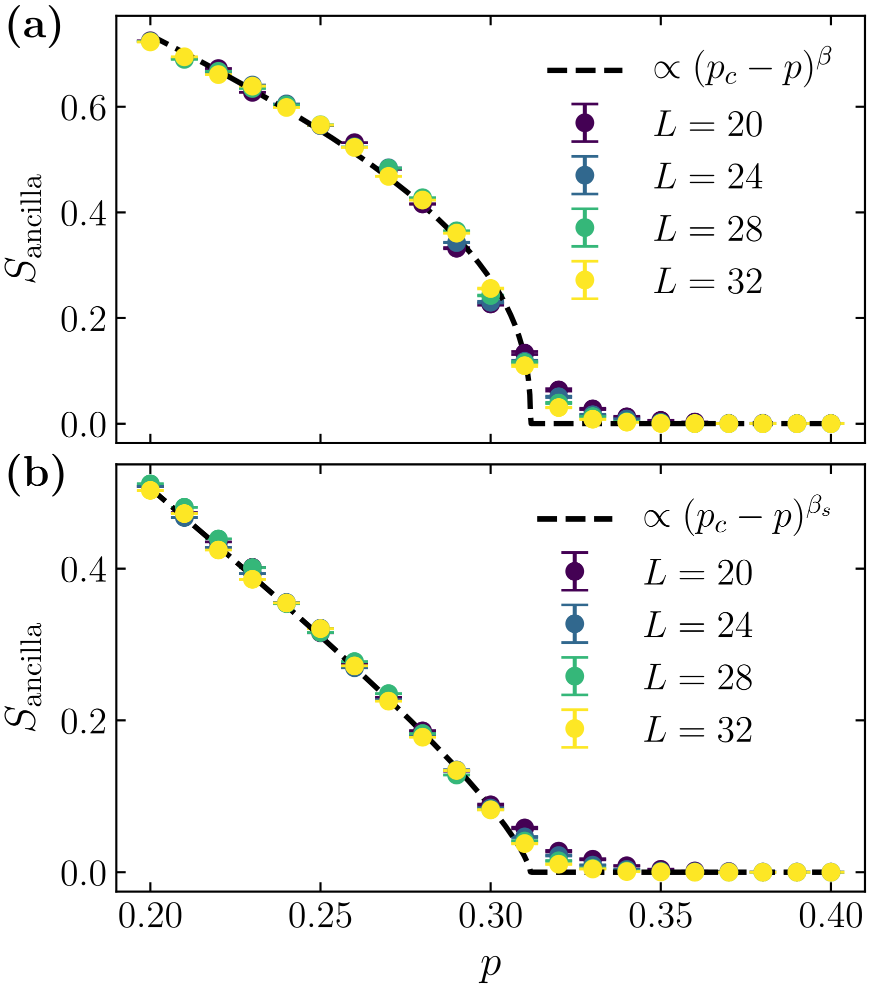

**Figure 5.9:** Extracting the exponents $\beta$ and $\beta_s$ using the entropy $S_{\text{ancilla}}$ of an ancilla qubit which is maximally entangled with a bulk qubit at a time $t_0$, and then further evolved for a time $t = 2L$. **(a)** The bulk exponent $\beta$ is extracted using $t_0 = 2L$. The black dashed curve shows the function $B(p_c - p)^\beta$ where $B \approx 3.2$ and $\beta \approx 0.40(1)$. **(b)** The surface exponent $\beta_s$ is extracted using $t_0 = 0$. There the black dashed curve shows the function $C(p_c - p)^{\beta_s}$ where $C \approx 4.6$ and $\beta_s \approx 0.74(2)$. In both cases, $p_c \approx 0.312$ is fixed by finite-size scaling of $I_3$. This dataset consists of $1 \times 10^4$ circuit realizations.

## 5.4 Entanglement clusters

Finally, with the aim of further exploring connections with percolation, we investigate entanglement clusters in the steady state. Working within the graph-state framework for simulating stabilizer states, we define an entanglement cluster in the graph-theoretic sense: two spins are in the same cluster if there is a connected path between them (see Fig. 5.2 for an example). We will mainly study the size $s$ of the clusters, defined for a given cluster as the number of spins it contains. This is clearly quite a coarse-grained notion of entanglement, since different spins in the same cluster can be entangled by different amounts. Nonetheless, it provides some insight into how multipartite is the steady-state entanglement.

If we assume that there is a percolation-like statistical mechanical model controlling the critical point, then naively one would expect the scaling of the entanglement clusters to be controlled by surface exponents of $(d+1)$-dimensional percolation. We will focus on two quantities, the largest entanglement cluster size $s_{\max}$, and the mean entanglement cluster size $\overline{s}$. Within the percolation language, these correspond to the 'surface area' of the infinite percolating cluster (assuming the largest surface cluster coincides with the largest bulk cluster), and the mean 'surface area' of clusters with at least one site on the surface, where by 'surface area' we mean the number of sites in the cluster that lie on the surface. In a $(d+1)$-dimensional percolation model with finite linear extent $L$, these should scale as $s_{\max}/L^d \sim L^{-\beta_s/\nu}$ and $\overline{s} \sim L^{\gamma_{1,1}/\nu}$ respectively.

To check this naive expectation, we first analyzed the scaling of entanglement clusters within the projective transverse field Ising model (PTFIM), as discussed in more detail in Section 5.D. This is a measurement-only model exhibiting an entanglement transition which is known to be in the percolation universality class [92]. Conveniently, it also only involves Clifford operations, so can be simulated using the graph-state framework, and therefore provides a useful testbed for the scaling properties of the entanglement clusters. The results are summarized in Fig. 5.D1, where we show data for the mean cluster size and largest cluster size for the PTFIM in both 1+1D and 2+1D. In 1+1D, these quantities both scale as power-laws with exponents closely matching the expected values from surface 2D percolation. In 2+1D, the largest cluster size also follows a power-law closely matching the expectation from surface 3D percolation. The mean cluster size appears to have a slightly larger exponent than expected, but it is possible that this discrepancy is due to significant finite-size effects, as we discuss in more detail in Section 5.D. Nonetheless, taken as a whole we believe these results provide reasonable evidence to suggest that if the critical circuit dynamics has a simple geometric map to percolation, as in the PTFIM, then we should expect the scaling of the entanglement clusters to be controlled by surface exponents of $(d+1)$-dimensional percolation.

In fact, we will see that the critical properties of the entanglement clusters in the steady-state of the random Clifford circuits scale with exponents quite distinct from those of surface $(d+1)$-dimensional percolation. Several of them are controlled by exponents close to those of bulk $d$-dimensional percolation, but it is possible this could be a coincidence. We offer two possible interpretations of these results. First, this could be further evidence that the measurement-induced transition in random Clifford circuits on qubits is in a distinct universality class to percolation, which is the conclusion of several recent studies [72, 76, 138]. Second, lessons from Haar-random circuits [75] suggest that, even if a map to percolation does exist in certain limits, it may be highly non-trivial, and in particular may not have a simple geometric interpretation as for the PTFIM and the Hartley entropy in Haar circuits [68]. As a consequence it is less obvious that the critical properties of the entanglement clusters in random Clifford circuits should be controlled by the surface exponents $\beta_s$ and $\gamma_{1,1}$ that are relevant for models that do have a simple geometric map to percolation.

Before we go into more detail, we make a brief comment about notation. As we just discussed, in the absence of a simple geometric map to percolation, it is not obvious that the mean and largest cluster sizes should be controlled by the surface exponents $\gamma_{1,1}$ and $\beta_s$ as they are in the PTFIM. For this reason we will label exponents for the entanglement clusters with the subscript $ec$, and do not claim that they should necessarily match the exponents $\gamma_{1,1}$ and $\beta_s$ in all models.

To find the entanglement clusters, we employ a breadth-first search on the graph storing the steady state [151]. Fig. 5.10 shows the behavior of the average cluster size $\overline{s} = \sum_s n_s s^2 / \sum_{s'} n_{s'} s'$, where the cluster number $n_s$ is the number of clusters of size $s$ normalized by the system volume $L^d$. Note that this quantity measures the average cluster size if *sites* are randomly selected with equal probability—if instead *clusters* are randomly selected with equal probability then the corresponding average is $\sum_s n_s s / \sum_{s'} n_{s'}$. Assuming critical scaling of the form $\overline{s} \sim L^{\gamma_{ec}/\nu}$, the inset to Fig. 5.10a shows a log-log plot of this quantity for 1+1D Clifford circuits, with a fitted exponent of $\gamma_{ec}/\nu \approx 0.95(1)$ shown by the solid red line, close to the value of $\gamma/\nu = 1$ for 1D bulk percolation [147], and far from the value $\gamma_{1,1}/\nu = 1/3$ for surface 2D percolation [152]. The analogous plot for 2+1D Clifford circuits is shown in the inset to Fig. 5.10b, where the fitted exponent $\gamma_{ec}/\nu \approx 1.84(2)$ is close to the value $\gamma/\nu = 43/24 \approx 1.79$ for bulk 2D percolation, and far from the value $\gamma_{1,1}/\nu \approx 0.060(12)$ for surface 3D percolation [152].

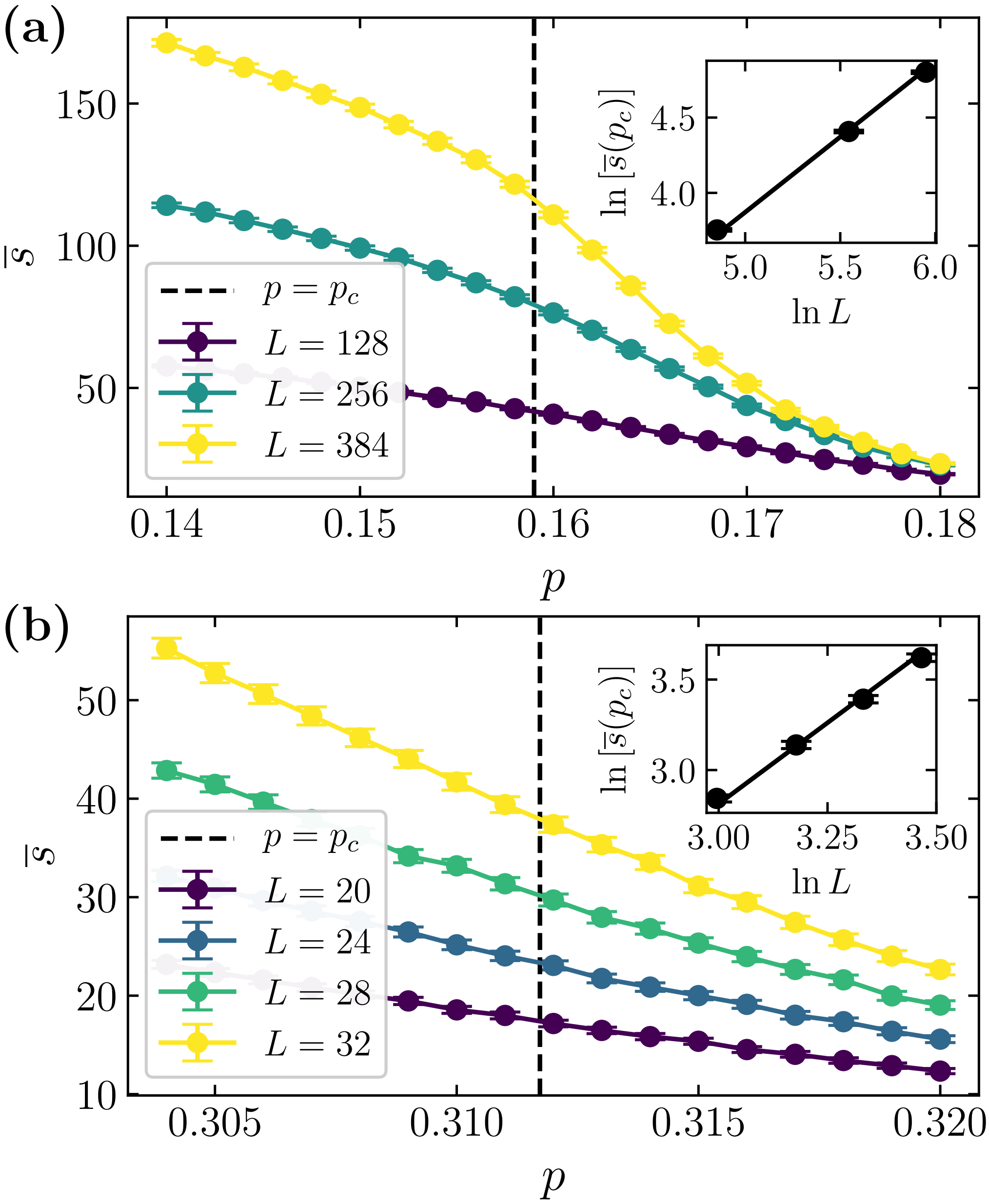

**Figure 5.10:** The average size $\overline{s}$ of all entanglement clusters in the steady-state for **(a)** 1+1D and **(b)** 2+1D Clifford circuits. The insets show log-log plots of this quantity at $p = p_c$, with the behaviour well described by the power law $\overline{s} \sim L^{\gamma_{ec}/\nu}$, where $\gamma_{ec}/\nu = 0.95(1)$ for 1+1D and $\gamma_{ec}/\nu = 1.84(2)$ for 2+1D (power-law fits shown in solid red).

Fig. 5.11 shows the average over circuit realizations of the size $s_{\text{max}}$ of the largest steady-state cluster in each realization, as a fraction of system size. This is a measure of the surface fractal dimension $d_f$ of the infinite cluster since by definition $s_{\text{max}} \sim L^{d_f} \sim L^{d-\beta_s/\nu}$. The inset to Fig. 5.11a shows a log-log plot of $\overline{s_{\text{max}}}(p_c)/L^d \sim L^{-\beta_{ec}/\nu}$ for 1+1D Clifford circuits, which is well described by the fitted exponent $\beta_{ec}/\nu \approx -0.009(2)$. This is close to the value $\beta/\nu = 0$ for 1D bulk percolation, and far from the exponent $\beta_s/\nu = 1/3$ for surface 2D percolation. In 2+1D, we find that there are significant finite-size effects affecting the scaling of the largest cluster size. For small system sizes, $L \lessapprox 32$, the power-law exponent is close to the bulk 2D percolation exponent $\beta/\nu = 5/48 \approx 0.10$, but this appears to be a finite-size effect. At larger system sizes the exponent saturates to approximately zero, with the fitted value $\beta_{ec}/\nu \approx 0.00(2)$, which is very far from the surface 3D percolation exponent of $\beta_s/\nu \approx 0.97$ [153].

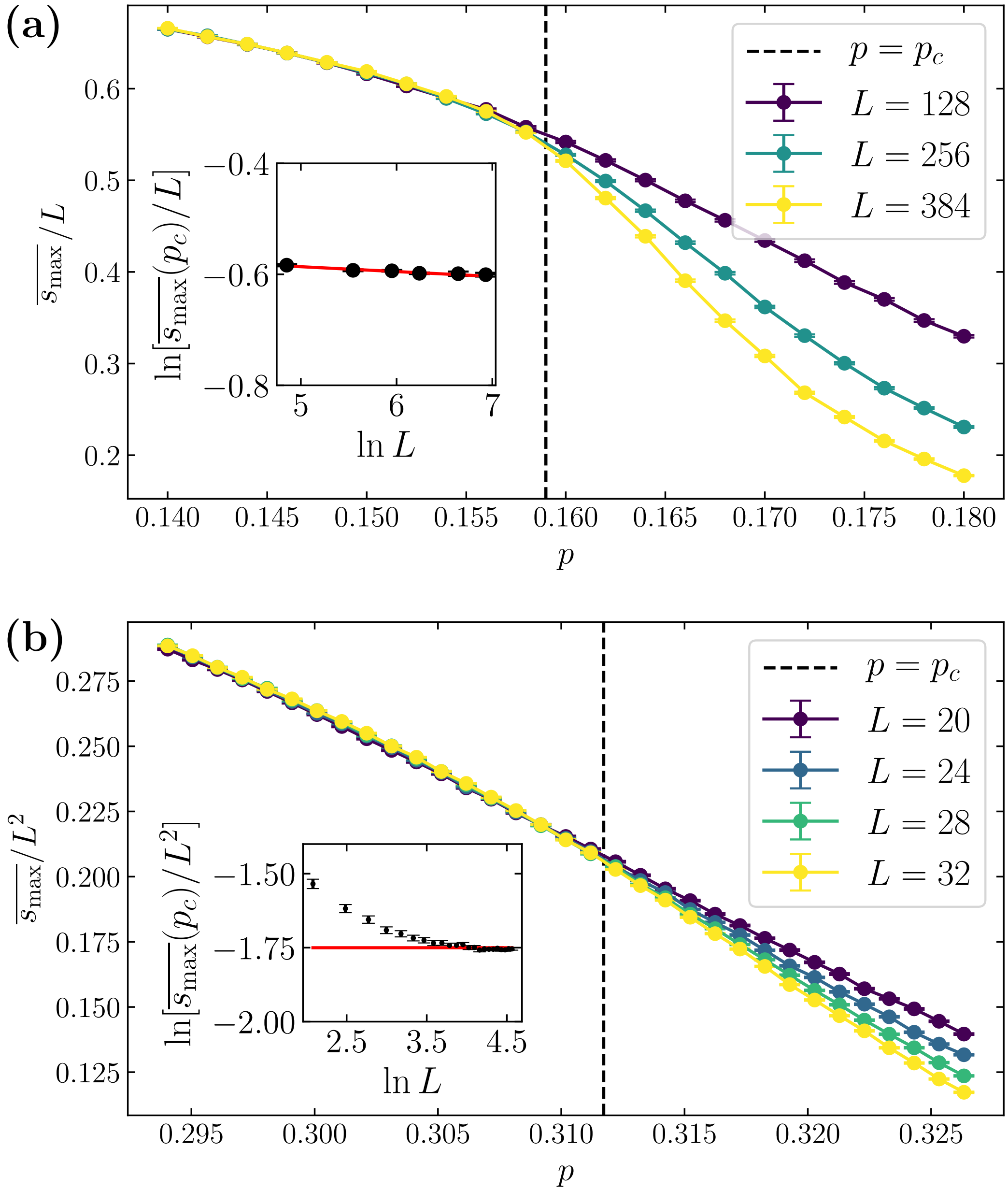

**Figure 5.11:** The average size $\overline{s_{\max}}$ of the largest entanglement cluster in the steady state for **(a)** 1+1D and **(b)** 2+1D Clifford circuits. The insets show log-log plots of this quantity at $p = p_c$, with the behavior well described by the power law $\overline{s_{\max}}(p_c)/L^d \sim L^{-\beta_{ec}/\nu}$, where $\beta_{ec}/\nu = -0.009(2)$ for 1+1D and $\beta_{ec}/\nu = 0.00(2)$ for 2+1D (power-law fits shown in solid red). Note there are strong finite-size effects in 2+1D, so there the fit is only to sizes $L \geq 40$.

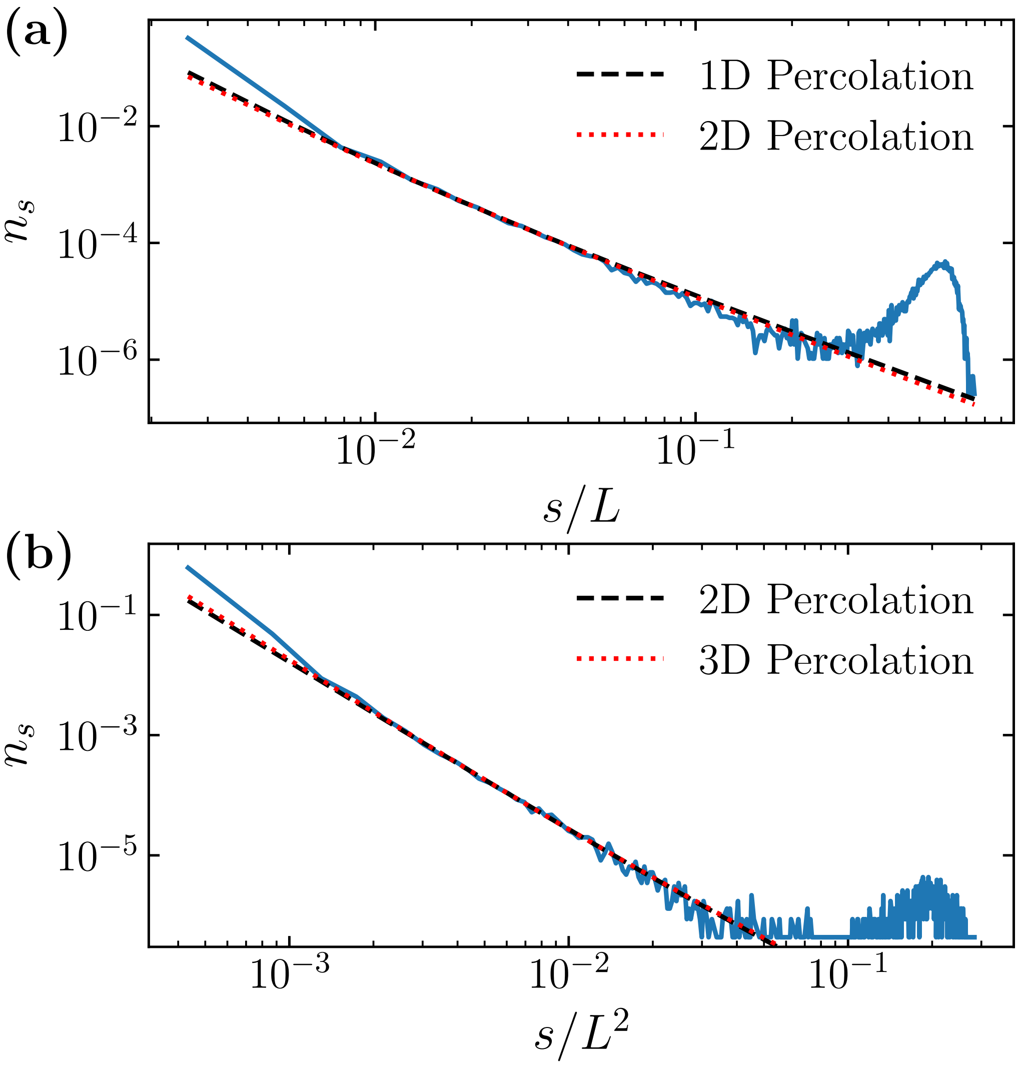

**Figure 5.12:** Distribution function $n_s$ of the entanglement cluster sizes $s$ in the $p = p_c$ steady state for **(a)** 1+1D and **(b)** 2+1D Clifford circuits, with system sizes $L = 348$ and $L^2 = 48^2$ respectively. For $1 \ll s \ll L^d$, the probability distribution follows a power-law distribution $n_s \sim s^{-\tau}(c_0 + c_1 s^{-\Omega})$ with the leading-order correction to scaling controlled by the exponent $\Omega$. The dashed and dotted lines show fits using the exponents from $d$- and $(d+1)$-dimensional percolation respectively. The peak at large $s$ corresponds to the percolating cluster of size $O(L^d)$ present for $p \leq p_c$.

Finally, in Fig. 5.12 we show the distribution $n_s$ of all cluster sizes $s$, which at $p = p_c$ and for $1 \ll s \ll L^d$ follows a power-law $n_s \sim s^{-\tau}(c_0 + c_1 s^{-\Omega} + \cdots)$, with the leading-order correction to scaling controlled by the exponent $\Omega$. A comment on this scaling form is necessary if we are to make a comparison with 1D percolation. As noted above, for 1D percolation the critical probability is $p_c = 1$. This has the consequence that, strictly at $p = p_c$, there is only a single cluster which covers the whole system, $s_{\max} = L$, so for cluster sizes $s < s_{\max}$ the cluster number $n_s = 0$. Nonetheless, one can meaningfully define the Fisher exponent $\tau$ by analyzing the behavior of $n_s$ for $p < p_c$, where one finds $\tau = 2$ for 1D percolation. However, a key difference between the 1+1D hybrid quantum circuits we study and 1D percolation is that for the quantum circuits, $1 - p_c \approx 0.84$ is different from unity, so there is still randomness at the critical point, and thus we can observe a full distribution of cluster sizes. This provides justification for continuing to use the scaling form $n_s \sim s^{-\tau}(c_0 + c_1 s^{-\Omega} + \cdots)$ to describe the cluster distribution function in 1+1D hybrid circuits.

In this case, it is harder to distinguish the behavior of $d$- and $(d+1)$-dimensional percolation, since the exponents for the leading term, $\tau_{\mathrm{1D}} = 2$, $\tau_{\mathrm{2D}} = 187/91 \approx 2.05$ [147] and $\tau_{\mathrm{3D}} \approx 2.19$ [145], are all quite similar in magnitude. Indeed both $\tau_{\mathrm{1D}}$ and $\tau_{\mathrm{2D}}$ provide a reasonable fit to our 1+1D data (see Fig. 5.12a), and both $\tau_{\mathrm{2D}}$ and $\tau_{\mathrm{3D}}$ provide a reasonable fit to our 2+1D data (see Fig. 5.12b). An independent statistical bootstrap analysis [154] gives the exponents $\tau \approx 2.04$ and $\Omega \approx 0.15$ in 1+1D, and $\tau \approx 1.98$ and $\Omega \approx 1.04$ in 2+1D. However, it is hard to call these values physically meaningful, since allowing for variation in the scaling correction exponent $\Omega$ provides considerable freedom to optimize the quality of the fit. What is at least clear is that the Fisher exponent $\tau$ is close to values predicted by percolation theory in *low dimensions*, since our fitted values are far from the mean-field value $\tau = 2.5$.

We conclude this section by noting that the entanglement cluster distribution is qualitatively similar to the stabilizer length distribution (SLD) introduced by Li, Chen and Fisher in Ref. [70]. Indeed, both have a power-law tail, and a volume-law peak which disappears upon entering the area-law phase. Furthermore, at criticality the exponent $\tau$ of the power-law tail is close to 2 in both cases. In 1+1D the SLD has the nice property that it can be used to calculate the entanglement entropy itself—for example, a power-law exponent of 2 gives rise to a subleading $\log L$ contribution to the entanglement entropy. However, it is not clear how to generalize the SLD to higher dimensions in a way that preserves this ability to calculate the entanglement entropy from the analogous 'stabilizer volume distribution'. From the entanglement cluster distribution we analyze here, it is possible to calculate the entanglement entropy provided one makes certain simplifying assumptions about the fractal structure of the entanglement clusters, but we defer further analysis of this link to future work.

## 5.5 Discussion

We have provided an extensive study of the critical properties of the measurement-induced transition in 2+1D Clifford circuits. Analogously to the situation in 1+1D, we have found several bulk critical exponents which are within error-bars of those from 3D percolation, but there appear to be some differences in surface behavior. We should note that these critical exponent estimates should be treated with some amount of caution, especially for small system sizes, as conformal field theories with zero central charge (like those appearing in current theories of the 1+1D transition [75]) can have logarithmic corrections to scaling [155, 156], which could result in systematic errors.

Nonetheless, focusing on this surface behavior, we studied the critical scaling of entanglement clusters in the steady state, and found that — in contrast to models with a simple geometric map to percolation — Clifford circuits have entanglement cluster exponents which differ significantly from those of surface percolation. We take this as evidence that in 1+1D and 2+1D the measurement-induced transition in qubit Clifford circuits is in a distinct universality class from percolation.

Presumably the entanglement clusters are governed by surface exponents of the as yet unknown $(d+1)$-dimensional statistical mechanical model applicable to Clifford circuits. It remains a significant question why the bulk exponents of this model look so much like those of percolation, even though this system is far from where the percolation picture should be applicable. There have been recent developments in the machinery required to average over random Clifford unitaries [157], which should prove helpful in developing this statistical mechanical model. However, the reduced structure relative to Haar-random unitaries makes it less obvious how to perform the replica limit required to give the correct critical physics.

We have also shown the coincidence of the purification transition and the entanglement transition in 2+1D. This may at first be surprising, given that the entanglement transition concerns spatial correlations between equal-time wavefunctions, while the purification transition concerns correlations in time of a non-local quantity. The results in this paper indicate that these two transitions may coincide in all dimensions. One possible explanation for this could be the conjecture of Ref. [76] that the non-unitary nature of the dynamics results in the real time coordinate in $d$ spatial dimensions acting as imaginary time in the corresponding $(d+1)$-dimensional statistical mechanical model. In this sense space and time may become symmetric, so the coincidence of the entanglement transition and the purification transition would be less surprising. The coincidence of these transitions and our entanglement cluster analysis also suggest a way to investigate connections with quantum error-correction—the emergence of the critical entanglement cluster can be seen as the germination of the quantum error-correcting code that characterizes the stability of the volume-law phase.

Moving into higher dimensions raises several questions. One interesting direction is that of 'measurement-protected order' [78, 79], analogous to the 'localization-protected order' afforded by many-body localization (MBL) [158, 159]. It is tempting to view the area-law side of the measurement-induced transition as a 'trivial' phase, but recent work has demonstrated that there can be stable symmetry-protected topological (SPT) order in the area-law phase, motivated by comparisons with the area-law ground states of gapped Hamiltonians. However, it is only in dimensions $d \geq 2$ that true topological order can exist [160], so it would be interesting to see if non-trivial topological order could be realized in the steady states of 2+1D hybrid quantum circuits. There is also the question of which types of order can be stabilized by measurements. There are significant constraints on possible phases stabilized by MBL: non-Abelian symmetries are forbidden [161], for example, as well as chiral order [162]. It is also possible that true MBL does not exist in $d > 1$ [163]. It is an important topic for future research to determine which restrictions, if any, are applicable to measurement-protected order. This may allow for considerably more freedom in the more general paradigm of understanding and classifying non-equilibrium phases of matter.

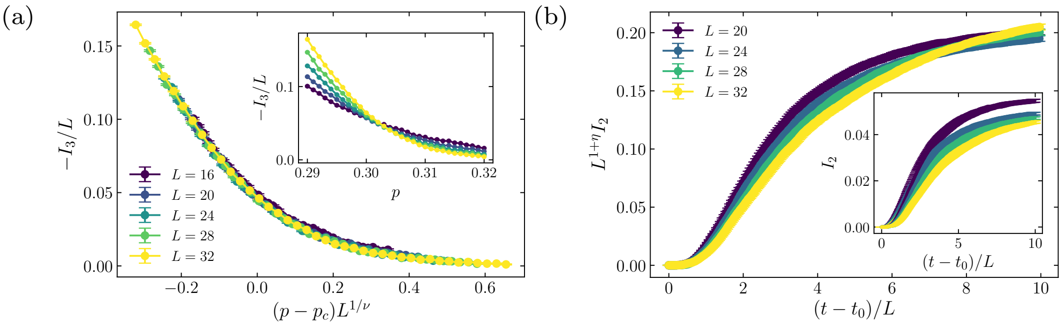

**Figure 5.A1:** **(a)** The steady-state values of $I_3/L$ as a function of $(p - p_c)L^{1/\nu}$, where $p_c \approx 0.303$ and $\nu \approx 1.07$. The inset shows the uncollapsed data. This dataset consists of 50,000 circuit realizations. **(b)** Analogous to Fig. 5.8a, except performed at the alternative critical point $p_c \approx 0.303$ estimated from the data collapse of $I_3/L$. The main plot shows the 'optimal' collapse at $\eta = -0.57$ as determined by minimizing the cost function in Section 5.B, but this clearly does not produce a good data collapse.

## 5.A Alternative scaling forms for $I_3$

In this section we detail some evidence against the hypothesis that $I_3 \sim \mathcal{O}(L)$ at $p = p_c$. Finite-size scaling of $I_3/L$ results in the critical point $p_c \approx 0.303$ with $\nu \approx 1.07$ (see Fig. 5.A1a). However, if we attempt to use this critical point to estimate other critical exponents from standard finite-size scaling arguments, we are unable to obtain a good data collapse, indicating the absence of scaling behavior. For example, to extract the anomalous scaling exponent $\eta$, we follow the procedure detailed in Section 5.3, where $\eta$ is chosen to optimize the data collapse of the dynamics of the mutual information between two ancilla qubits. Whereas this was possible for the critical point $p_c \approx 0.312$ obtained from finite-size scaling of $I_3$ (see Fig. 5.8a), for the purported critical point $p_c \approx 0.303$ from $I_3/L$ scaling, there was not a value of $\eta$ for which a good data collapse was possible (see Fig. 5.A1b). Moreover, the data collapse in Fig. 5.A1a is of visibly worse quality than the excellent collapse in Fig. 5.4. We also see in Section 5.3 that the purification transition seems to coincide with the critical point $p_c \approx 0.312$ from $I_3$ scaling, with a dynamical critical exponent $z \approx 1$ indicating the emergence of conformal symmetry. Given that these facts mirror the situation in 1+1D, this provides further *a posteriori* justification for the scaling $I_3 \sim \mathcal{O}(1)$ at criticality.

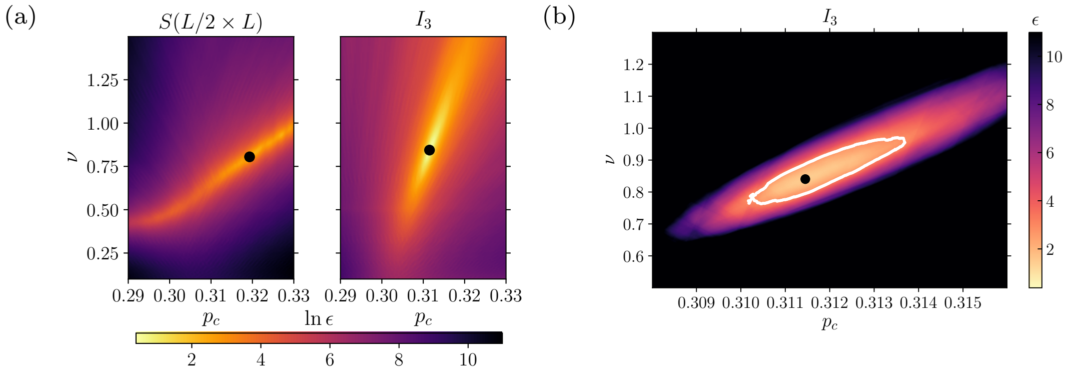

**Figure 5.B1:** **(a)** The logarithm of the cost function $\epsilon$ measuring the quality of the data collapse for different values of $p_c$ and $\nu$, compared between two possible indicators of the entanglement transition: the half-plane entanglement entropy $S(L/2)$, and the tripartite information $I_3$. The black dots show the minimum of the cost function for each indicator. See the appendix for a definition of the cost function $\epsilon$. **(b)** A linear-scale close-up of the cost function for the $I_3$ data collapse around the estimated critical point, which is indicated by the black dot. The white line indicates the boundary of the region for which the cost function is less than 2 times its minimum value; this is the region from which the error bars are calculated. At the estimated critical point the cost function attains the value $\epsilon = 1.47$, close to the optimal value $\epsilon \approx 1$.

## 5.B Details of the finite-size scaling

To perform the data collapses, we use a cost function $\epsilon(p_c, \nu)$ which uses linear interpolation to find the parameters $(p_c, \nu)$ which cause the data to best collapse on to a single curve [72, 143]. In more detail, given a set of parameters $(p_c, \nu)$, for each value of $p$ and $L$ we create an $x$-value $x := (p - p_c)L^{1/\nu}$, with a corresponding $y$-value $y(p, L)$ and error $d(p, L)$. We then sort the triples $(x_i, y_i, d_i)$ according to their $x$-values, and evaluate the cost function

$$\epsilon(p_c, \nu) := \frac{1}{n-2} \sum_{i=2}^{n-1} w(x_i, y_i, d_i | x_{i-1}, y_{i-1}, d_{i-1}, x_{i+1}, y_{i+1}, d_{i+1}), \tag{5.9}$$

where $w(x_i, y_i, d_i | x_{i-1}, y_{i-1}, d_{i-1}, x_{i+1}, y_{i+1}, d_{i+1})$ is defined as

$$w := \left( \frac{y - \bar{y}}{\Delta(y - \bar{y})} \right)^2, \tag{5.10}$$

$$\bar{y} := \frac{(x_{i+1} - x_i) y_{i-1} - (x_{i-1} - x_i) y_{i+1}}{x_{i+1} - x_{i-1}}, \tag{5.11}$$

$$|\Delta(y - \bar{y})|^2 := d_i^2 + \left( \frac{x_{i+1} - x_i}{x_{i+1} - x_{i-1}} \right)^2 d_{i-1}^2 + \left( \frac{x_{i-1} - x_i}{x_{i+1} - x_{i-1}} \right)^2 d_{i+1}^2. \tag{5.12}$$

The function $w$ measures the deviation of a point from the line obtained by a linear interpolation of its nearest neighbours, weighted by the errors in each data point. Values of $(p_c, \nu)$ for which $\epsilon(p_c, \nu) \approx 1$ are considered optimal.

As discussed in Section 5.2, our finite-size scaling analysis yields the correlation length exponent $\nu \approx 0.85(9)$, which is significantly different to that observed in Ref. [84]. We attribute this to the fact that we extract $\nu$ by a data collapse not of the half-plane entanglement, as in Ref. [84], but of the tripartite information, which coincides for different system sizes at the critical point and so provides a much more accurate estimator of the critical point. To further this point, we show in Fig. 5.B1a a comparison of the cost function $\epsilon(p_c, \nu)$ landscape in log scale between the half-plane entropy $S(L/2 \times L)$ and the tripartite information $I_3$. The entropy cost function plot shows a clear 'ridge' region where $\epsilon$ is roughly constant, spanning the whole range of values of $p_c$ and with a large variation of $\nu$ along the ridge (see also Fig. 2 in the Erratum of Ref. [84]). On the other hand, the $I_3$ cost function plot is much more localized around the estimated critical parameters, reaching a smaller value of $\epsilon$ than the entropy plot. This localization is less obvious viewed in log scale, but the log was necessary for a meaningful visual comparison of the cost function plots for the two indicators. Fig. 5.B1b shows a linear-scale version of the cost function plot for $I_3$, which allows for a clearer visualization of the localization of the cost function minimum. The estimated critical point is indicated by the large black dot, while the surrounding white line gives

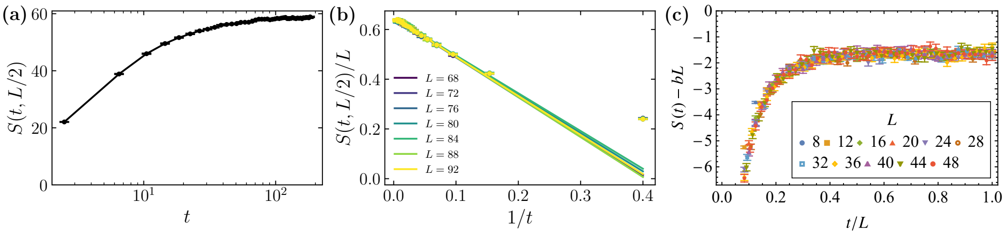

**Figure 5.C1:** The dynamics of the half-plane von Neumann entropy at the critical point $p_c = 0.312$ of the 2+1D Clifford model. **(a)** The data are not linear on a log scale, indicating that the entanglement growth is *not* logarithmic in time (system size is $L = 92$). **(b)** A plot of $S(t, L/2)/L$ as a function of $1/t$, where the linear trend provides support for the scaling $S(t, L) \sim L(1 - a/t)$. **(c)** Scaling collapse of $S(t) - bL$ vs $t/L$, with $b = 0.685$ producing the best fit.

the boundary of the region where the cost function is less than 2 times its minimum value, from which we calculate the error bars in $p_c$ and $\nu$. Notice that at the estimated critical point, the cost function reaches a value $\epsilon = 1.47$ close to 1, indicating a good-quality data collapse.

Furthermore, a comment on the used system sizes is necessary. One could argue that the 4 subsystems used to calculate $I_3$ have the vertical dimension $L_y \leq 8$, which may be small enough to exhibit substantial finite-size effects, hindering our ability to properly locate the critical point. However, $I_3$ in 1+1D circuits shows almost no finite-size drift at criticality already for systems of size $L \geq 16$ [72] (subsystems of size $\geq 4$). Using our data from Fig. 5.4, one can assess that the crossings of $I_3$ exhibit no statistically significant drift above roughly $L \geq 16$, strongly implying little to no finite-size effects in $I_3$ at criticality for the system sizes considered. We also note that the data collapse is of exceptional quality, again strongly ruling out any substantial finite-size drifts.

## 5.C Critical entanglement dynamics

In Fig. 5.C1 we plot the dynamics of the half-plane von Neumann entropy at the 2+1D critical point $p_c = 0.312$. Because the entanglement is relatively small at the critical point, we are able to simulate a large system with linear size $L = 92$. In Fig. 5.C1a the time axis is on a logarithmic scale, and we can see that the data do not appear linear on this scale, thereby demonstrating that the entanglement growth is not logarithmic in time. Note that we are plotting here the window-averaged entropy, averaged over a window of 4 timesteps, which is why there is not data at every timestep. This is to remove a periodicity effect related to how often the Clifford gates cross the cut used to define the entanglement entropy, as discussed in Section 5.1.2A.

As we discuss in Section 5.2, we instead argue that the entanglement growth scales as $S(t, L) = bL(1 - a/t)$ in 2+1D, where $a, b$ are some $\mathcal{O}(1)$ constants. Evidence for this is shown in Fig. 5.C1b, where the data appears approximately linear when plotted as a function of $1/t$. Note that the data appears linear on this scale, with the straight lines showing linear fits. The gradients and y-intercepts of these fits are approximately the same for different system sizes, supporting the idea that $a$ and $b$ are $\mathcal{O}(1)$ constants. Note that we only expect this scaling to hold for intermediate times, so there are some deviations from this behavior at early times. Finally, in Fig. 5.C1c, we show a data collapse of $S(t) - bL$ vs $t/L$ with $b = 0.685$, supporting the scaling ansatz $S(t) - bL \sim f(t/L)$ consistent with a dynamical critical exponent of $z = 1$.

## 5.D Entanglement clusters in the projective transverse field Ising model

The projective transverse field Ising model (PTFIM) is a measurement-only model exhibiting an entanglement transition which is known to be in the percolation universality class [92]. Conveniently, it also only involves Clifford operations, so can be simulated using the graph-state framework, and therefore provides a useful testbed for the scaling properties of the entanglement clusters we analyze in Section 5.4.

Referring the reader to Ref. [92] for the full details, the PTFIM is defined as

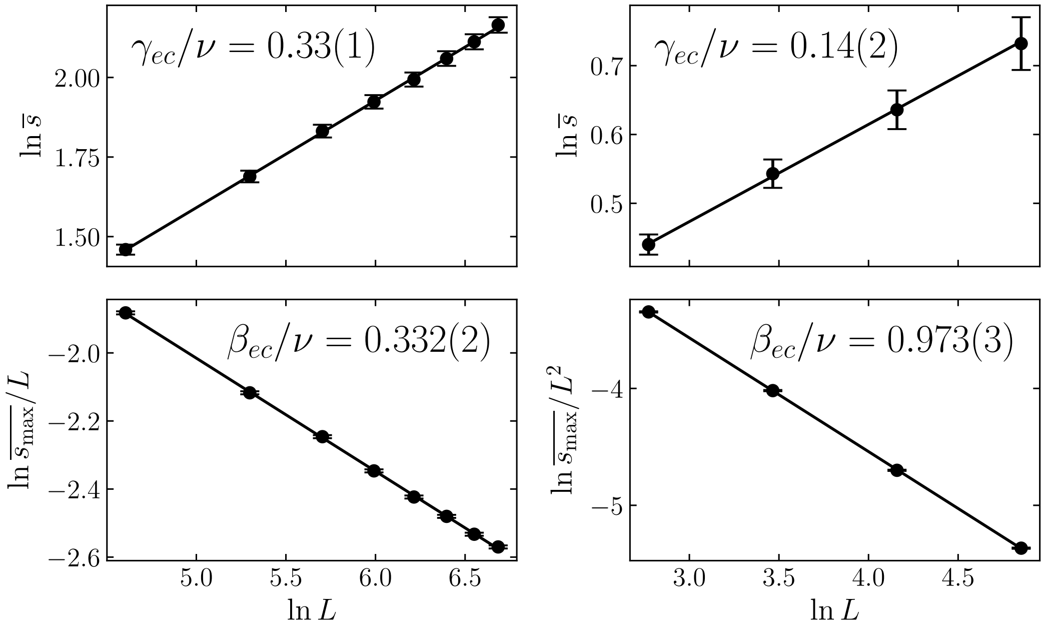

**Figure 5.D1:** The mean cluster size $\overline{s}$ and largest cluster size $s_{\text{max}}/L^d$ for the projective transverse field Ising model in 1+1D (left column) and 2+1D (right column). These should scale as $\overline{s} \sim L^{\gamma_{1,1}/\nu}$ and $s_{\text{max}}/L^d \sim L^{-\beta_s/\nu}$ respectively. The critical exponents are all close to the corresponding surface critical exponents of percolation in $(d+1)$-dimensions, with the exception of the mean cluster size in 2+1D, as we discuss in the main text.

follows. We define the model on a hypercubic lattice for simplicity. Each site of the lattice contains a spin. The model involves two types of measurements: on-site measurements of $\sigma^x$, and measurements of $\sigma^z\sigma^z$ for spins connected by an edge. The system is initialized in the product state $|+\rangle^{\otimes N}$, where $|+\rangle = (|0\rangle + |1\rangle)/\sqrt{2}$. Then, at each timestep, for each site $i$ assign the variable $x_i = 1$ with probability $p$ and $x_i = 0$ otherwise, and for each edge $e$ connecting spins $i$ and $j$, assign the variable $z_e = 1$ with probability $1-p$ and $z_e = 0$ otherwise. These variables determine the sites and edges on which the observables $\sigma_i^x$ and $\sigma_i^z\sigma_j^z$ are measured. The edge observables are measured first, followed by the site observables. On a $d$-dimensional hypercubic lattice, this process maps on to bond percolation on a $(d+1)$-dimensional hypercubic lattice.

As previously, we focus on two properties of the surface clusters: the largest cluster size $s_{\text{max}}$, and the mean cluster size $\overline{s}$. In a system with $d$ spatial dimensions and linear size $L$, these should scale as $s_{\text{max}}/L^d \sim L^{-\beta_s/\nu}$ and $\overline{s} \sim L^{\gamma_{1,1}/\nu}$ respectively. Our results for the PTFIM in 1+1D and 2+1D are shown in the left and right columns of Fig. 5.D1, where we perform simulations up to $L = 800$ and $L = 128$ respectively. In 1+1D, the resulting exponents for the entanglement clusters are $\gamma_{ec}/\nu = 0.33(1)$ for the mean cluster size and $\beta_{ec}/\nu = 0.332(2)$ for the largest cluster size. These are very close to the corresponding surface exponents for 2D percolation, $\gamma_{1,1}/\nu = 1/3$ and $\beta_s/\nu = 1/3$. In 2+1D, the extracted exponent for the largest cluster size is $\beta_{ec}/\nu = 0.973(3)$, which is very close to the exponent $\beta_s/\nu \approx 0.9754(4)$ for 3D percolation [153]. For the mean cluster size in 2+1D, the situation is less clear. We extract an exponent for the entanglement clusters of $\gamma_{ec}/\nu = 0.14(2)$. The exponent $\gamma_{1,1}$ does not appear to be well documented for 3D percolation, however, from the scaling relation $\gamma_{1,1}/\nu = d - 1 - 2\beta_s/\nu$ [152, 164] we estimate the value $\gamma_{1,1}/\nu = 0.0492(8)$, which is not compatible within error bars of the exponent $\gamma_{ec}/\nu$. Nonetheless, it is very likely that there are large finite size effects for this exponent — we have performed percolation simulations (see Fig. 5.D2) to reproduce the quoted value for $\gamma_{1,1}/\nu$, and found that we had to be very careful with the subleading corrections to scaling in order to get the correct exponent, even up to surprisingly large

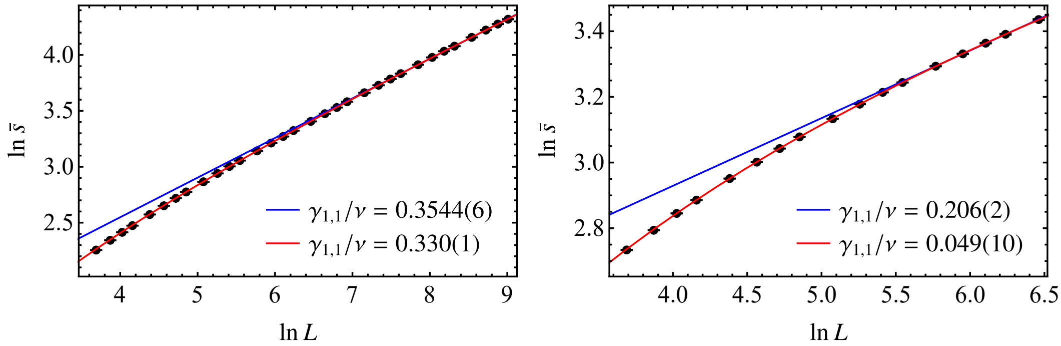

**Figure 5.D2:** The mean surface cluster size $\overline{s}$ for the site percolation on a 2D square lattice (left) and a 3D simple cubic lattice (right). Blue line is a fit to $\overline{s} = aL^{\gamma_{1,1}/\nu}$ for the largest system sizes, while the red line includes a constant correction to scaling, $\overline{s} = aL^{\gamma_{1,1}/\nu} + b$. Corresponding estimates of $\gamma_{1,1}/\nu$ are given in the legend.

system sizes ($L \leq 640$). Without accounting for the corrections, we obtain a larger exponent, $\gamma_{1,1}/\nu \sim 0.206(2)$, while including a constant correction gives $\gamma_{1,1}/\nu \sim 0.049(10)$, a value close to the expectation from the scaling relation. For the 2+1D Clifford circuit we have simulated up to $L = 128$ at criticality, but it is possible that there are still significant finite size corrections to $\gamma_{ec}/\nu$ that are not captured by the statistical error bars we quote here. It, however, needs to be noted that there are relatively large error bars on $\overline{s}$ for PTFIM in 2+1D which could conceal finite size effects, while the corresponding results for Clifford circuit have smaller error bars and seem to exhibit small finite size effects.

# Bibliography

[1] M. B. Hastings, "Quasi-adiabatic continuation in gapped spin and fermion systems: Goldstone's theorem and flux periodicity", Journal of Statistical Mechanics: Theory and Experiment **2007**, P05010–P05010 (2007).

[2] J. M. Deutsch, "Quantum statistical mechanics in a closed system", Physical Review A **43**, 2046–2049 (1991).

[3] M. Srednicki, "Chaos and quantum thermalization", Physical Review E **50**, 888–901 (1994).

[4] L. D'Alessio, Y. Kafri, A. Polkovnikov, and M. Rigol, "From quantum chaos and eigenstate thermalization to statistical mechanics and thermodynamics", Advances in Physics **65**, 239–362 (2016).

[5] N. D. Mermin and H. Wagner, "Absence of Ferromagnetism or Antiferromagnetism in One- or Two-Dimensional Isotropic Heisenberg Models", Physical Review Letters **17**, 1133–1136 (1966).

[6] P. C. Hohenberg, "Existence of Long-Range Order in One and Two Dimensions", Physical Review **158**, 383–386 (1967).

[7] J. Fröhlich and C. Pfister, "On the absence of spontaneous symmetry breaking and of crystalline ordering in two-dimensional systems", Communications in Mathematical Physics **81**, 277–298 (1981).

[8] S. Bravyi and B. Terhal, "A no-go theorem for a two-dimensional self-correcting quantum memory based on stabilizer codes", New Journal of Physics **11**, 043029 (2009).

[9] F. Wilczek, “Quantum Time Crystals”, Physical Review Letters **109**, 160401 (2012).

[10] P. Bruno, “Comment on "Quantum Time Crystals"”, Physical Review Letters **110**, 118901 (2013).

[11] P. Bruno, “Comment on "Space-Time Crystals of Trapped Ions"”, Physical Review Letters **111**, 029301 (2013).

[12] P. Bruno, “Impossibility of Spontaneously Rotating Time Crystals: A No-Go Theorem”, Physical Review Letters **111**, 070402 (2013).

[13] H. Watanabe and M. Oshikawa, “Absence of Quantum Time Crystals”, Physical Review Letters **114**, 251603 (2015).

[14] H. Watanabe, M. Oshikawa, and T. Koma, “Proof of the Absence of Long-Range Temporal Orders in Gibbs States”, Journal of Statistical Physics **178**, 926–935 (2020).

[15] Y. Huang, “Absence of temporal order in states with fast decay of spatial correlations”, (2019), arXiv:`1912.01210`.

[16] H. Araki, “Gibbs states of a one dimensional quantum lattice”, Communications in Mathematical Physics **14**, 120–157 (1969).

[17] D. Pérez-García and A. Pérez-Hernández, “Locality estimes for complex time evolution in 1D”, (2020), arXiv:`2004.10516`.

[18] D. V. Else, B. Bauer, and C. Nayak, “Floquet Time Crystals”, Physical Review Letters **117**, 090402 (2016).

[19] N. Y. Yao, A. C. Potter, I.-D. Potirniche, and A. Vishwanath, “Discrete Time Crystals: Rigidity, Criticality, and Realizations”, Physical Review Letters **118**, 030401 (2017).

[20] A. Lazarides, A. Das, and R. Moessner, “Equilibrium states of generic quantum systems subject to periodic driving”, Physical Review E **90**, 012110 (2014).

[21] V. Khemani, A. Lazarides, R. Moessner, and S. L. Sondhi, “Phase Structure of Driven Quantum Systems”, Physical Review Letters **116**, 250401 (2016).

[22] D. V. Else, B. Bauer, and C. Nayak, “Prethermal Phases of Matter Protected by Time-Translation Symmetry”, Physical Review X **7**, 011026 (2017).

[23] B. Kraus, H. P. Büchler, S. Diehl, A. Kantian, A. Micheli, and P. Zoller, “Preparation of entangled states by quantum Markov processes”, Physical Review A **78**, 042307 (2008).

[24] S. Diehl, A. Micheli, A. Kantian, B. Kraus, H. P. Büchler, and P. Zoller, “Quantum states and phases in driven open quantum systems with cold atoms”, Nature Physics **4**, 878–883 (2008).

[25] F. Verstraete, M. M. Wolf, and J. Ignacio Cirac, “Quantum computation and quantum-state engineering driven by dissipation”, Nature Physics **5**, 633–636 (2009).

[26] J. Zhang, P. W. Hess, A. Kyprianidis, P. Becker, A. Lee, J. Smith, G. Pagano, I.-D. Potirniche, A. C. Potter, A. Vishwanath, N. Y. Yao, and C. Monroe, “Observation of a discrete time crystal”, Nature **543**, 217–220 (2017).

[27] N. Y. Yao, C. R. Laumann, S. Gopalakrishnan, M. Knap, M. Müller, E. A. Demler, and M. D. Lukin, “Many-Body Localization in Dipolar Systems”, Physical Review Letters **113**, 243002 (2014).

[28] A. L. Burin, “Many-body delocalization in a strongly disordered system with long-range interactions: Finite-size scaling”, Physical Review B **91**, 094202 (2015).

[29] V. Khemani, R. Moessner, and S. L. Sondhi, “A Brief History of Time Crystals”, (2019), arXiv:`1910.10745`.

[30] M. Ippoliti, K. Kechedzhi, R. Moessner, S. L. Sondhi, and V. Khemani, “Many-body physics in the NISQ era: quantum programming a discrete time crystal”, (2021), arXiv:`2007.11602`.

[31] J. Randall, C. E. Bradley, F. V. van der Gronden, A. Galicia, M. H. Abobeih, M. Markham, D. J. Twitchen, F. Machado, N. Y. Yao, and T. H. Taminiau, “Observation of a many-body-localized discrete time crystal with a programmable spin-based quantum simulator”, (2021), arXiv:`2107.00736`.

[32] J. O'Sullivan, O. Lunt, C. W. Zollitsch, M. L. W. Thewalt, J. J. L. Morton, and A. Pal, "Signatures of discrete time crystalline order in dissipative spin ensembles", New Journal of Physics **22**, 085001 (2020).

[33] S. Choi, J. Choi, R. Landig, G. Kucsko, H. Zhou, J. Isoya, F. Jelezko, S. Onoda, H. Sumiya, V. Khemani, C. von Keyserlingk, N. Y. Yao, E. Demler, and M. D. Lukin, "Observation of discrete time-crystalline order in a disordered dipolar many-body system", Nature **543**, 221–225 (2017).

[34] J. Rovny, R. L. Blum, and S. E. Barrett, "Observation of Discrete-Time-Crystal Signatures in an Ordered Dipolar Many-Body System", Physical Review Letters **120**, 180603 (2018).

[35] E. Levi, M. Heyl, I. Lesanovsky, and J. P. Garrahan, "Robustness of Many-Body Localization in the Presence of Dissipation", Physical Review Letters **116**, 237203 (2016).

[36] M. V. Medvedyeva, T. Prosen, and M. Žnidarič, "Influence of dephasing on many-body localization", Physical Review B **93**, 094205 (2016).

[37] S. Wimperis, "Broadband, Narrowband, and Passband Composite Pulses for Use in Advanced NMR Experiments", Journal of Magnetic Resonance, Series A **109**, 221–231 (1994).

[38] C. W. von Keyserlingk, V. Khemani, and S. L. Sondhi, "Absolute stability and spatiotemporal long-range order in Floquet systems", Physical Review B **94**, 085112 (2016).

[39] N. V. Prokof'ev and P. C. E. Stamp, "Theory of the spin bath", Reports on Progress in Physics **63**, 669 (2000).

[40] M. Bortz and J. Stolze, "Exact dynamics in the inhomogeneous central-spin model", Physical Review B **76**, 014304 (2007).

[41] E. A. Chekhovich, M. N. Makhonin, A. I. Tartakovskii, A. Yacoby, H. Bluhm, K. C. Nowack, and L. M. K. Vandersypen, "Nuclear spin effects in semiconductor quantum dots", Nature Materials **12**, 494–504 (2013).

[42] A. V. Khaetskii, D. Loss, and L. Glazman, "Electron Spin Decoherence in Quantum Dots due to Interaction with Nuclei", Physical Review Letters **88**, 186802 (2002).

[43] E. A. Yuzbashyan, B. L. Altshuler, V. B. Kuznetsov, and V. Z. Enolskii, "Solution for the dynamics of the BCS and central spin problems", Journal of Physics A: Mathematical and General **38**, 7831–7849 (2005).

[44] W. Yao, R.-B. Liu, and L. J. Sham, "Theory of electron spin decoherence by interacting nuclear spins in a quantum dot", Physical Review B **74**, 195301 (2006).

[45] G. Chen, D. L. Bergman, and L. Balents, "Semiclassical dynamics and long-time asymptotics of the central-spin problem in a quantum dot", Physical Review B **76**, 045312 (2007).

[46] Ł. Cywiński, W. M. Witzel, and S. Das Sarma, "Electron Spin Dephasing due to Hyperfine Interactions with a Nuclear Spin Bath", Physical Review Letters **102**, 057601 (2009).

[47] E. Barnes, Ł. Cywiński, and S. Das Sarma, "Nonperturbative Master Equation Solution of Central Spin Dephasing Dynamics", Physical Review Letters **109**, 140403 (2012).

[48] G. Wolfowicz, A. M. Tyryshkin, R. E. George, H. Riemann, N. V. Abrosimov, P. Becker, H.-J. Pohl, M. L. W. Thewalt, S. A. Lyon, and J. J. L. Morton, "Atomic clock transitions in silicon-based spin qubits", Nature Nanotechnology **8**, 561–564 (2013).

[49] W. M. Witzel, M. S. Carroll, A. Morello, Ł. Cywiński, and S. Das Sarma, "Electron Spin Decoherence in Isotope-Enriched Silicon", Physical Review Letters **105**, 187602 (2010).

[50] W. M. Witzel, M. S. Carroll, Ł. Cywiński, and S. Das Sarma, "Quantum decoherence of the central spin in a sparse system of dipolar coupled spins", Physical Review B **86**, 035452 (2012).

[51] N. Bar-Gill, L. M. Pham, C. Belthangady, D. Le Sage, P. Cappellaro, J. R. Maze, M. D. Lukin, A. Yacoby, and R. Walsworth, "Suppression of spin-bath

dynamics for improved coherence of multi-spin-qubit systems", Nature Communications **3**, 858 (2012).

[52]M. B. Hastings and X.-G. Wen, "Quasiadiabatic continuation of quantum states: The stability of topological ground-state degeneracy and emergent gauge invariance", Physical Review B **72**, 045141 (2005).

[53]D. N. Page, "Average entropy of a subsystem", Physical Review Letters **71**, 1291–1294 (1993).

[54]M. Žnidarič, T. Prosen, and P. Prelovšek, "Many-body localization in the Heisenberg $XXZ$ magnet in a random field", Physical Review B **77**, 064426 (2008).

[55]M. Serbyn, Z. Papić, and D. A. Abanin, "Universal Slow Growth of Entanglement in Interacting Strongly Disordered Systems", Physical Review Letters **110**, 260601 (2013).

[56]J. H. Bardarson, F. Pollmann, and J. E. Moore, "Unbounded Growth of Entanglement in Models of Many-Body Localization", Physical Review Letters **109**, 017202 (2012).

[57]D. A. Huse, R. Nandkishore, and V. Oganesyan, "Phenomenology of fully many-body-localized systems", Physical Review B **90**, 174202 (2014).

[58]A. Nanduri, H. Kim, and D. A. Huse, "Entanglement spreading in a many-body localized system", Physical Review B **90**, 064201 (2014).

[59]M. B. Hastings, "An area law for one-dimensional quantum systems", Journal of Statistical Mechanics: Theory and Experiment **2007**, P08024–P08024 (2007).

[60]A. Anshu, I. Arad, and D. Gosset, "Entanglement subvolume law for 2d frustration-free spin systems", in Proceedings of the 52nd Annual ACM SIGACT Symposium on Theory of Computing, STOC 2020 (June 2020), pp. 868–874.

[61]N. Schuch, M. M. Wolf, F. Verstraete, and J. I. Cirac, "Entropy Scaling and Simulability by Matrix Product States", Physical Review Letters **100**, 030504 (2008).

[62] U. Schollwöck, "The density-matrix renormalization group in the age of matrix product states", Annals of Physics, January 2011 Special Issue **326**, 96–192 (2011).

[63] P. Calabrese and J. Cardy, "Entanglement entropy and quantum field theory", Journal of Statistical Mechanics: Theory and Experiment **2004**, P06002 (2004).

[64] E. Fradkin and J. E. Moore, "Entanglement Entropy of 2D Conformal Quantum Critical Points: Hearing the Shape of a Quantum Drum", Physical Review Letters **97**, 050404 (2006).

[65] M. Heyl, "Dynamical quantum phase transitions: a review", Reports on Progress in Physics **81**, 054001 (2018).

[66] Y. Li, X. Chen, and M. P. A. Fisher, "Quantum Zeno effect and the many-body entanglement transition", Physical Review B **98**, 205136 (2018).

[67] A. Chan, R. M. Nandkishore, M. Pretko, and G. Smith, "Unitary-projective entanglement dynamics", Physical Review B **99**, 224307 (2019).

[68] B. Skinner, J. Ruhman, and A. Nahum, "Measurement-Induced Phase Transitions in the Dynamics of Entanglement", Physical Review X **9**, 031009 (2019).

[69] M. Szyniszewski, A. Romito, and H. Schomerus, "Entanglement transition from variable-strength weak measurements", Physical Review B **100**, 064204 (2019).

[70] Y. Li, X. Chen, and M. P. A. Fisher, "Measurement-driven entanglement transition in hybrid quantum circuits", Physical Review B **100**, 134306 (2019).

[71] J. Napp, R. L. La Placa, A. M. Dalzell, F. G. S. L. Brandao, and A. W. Harrow, "Efficient classical simulation of random shallow 2D quantum circuits", (2019), arXiv:`2001.00021`.

[72] A. Zabalo, M. J. Gullans, J. H. Wilson, S. Gopalakrishnan, D. A. Huse, and J. H. Pixley, "Critical properties of the measurement-induced transition in random quantum circuits", Physical Review B **101**, 060301 (2020).

[73] R. Fan, S. Vijay, A. Vishwanath, and Y.-Z. You, "Self-Organized Error Correction in Random Unitary Circuits with Measurement", (2020), arXiv:2002.12385.

[74] Y. Bao, S. Choi, and E. Altman, "Theory of the phase transition in random unitary circuits with measurements", Physical Review B **101**, 104301 (2020).

[75] C.-M. Jian, Y.-Z. You, R. Vasseur, and A. W. W. Ludwig, "Measurement-induced criticality in random quantum circuits", Physical Review B **101**, 104302 (2020).

[76] Y. Li, X. Chen, A. W. W. Ludwig, and M. P. A. Fisher, "Conformal invariance and quantum non-locality in hybrid quantum circuits", (2020), arXiv:2003.12721.

[77] O. Shtanko, Y. A. Kharkov, L. P. García-Pintos, and A. V. Gorshkov, "Classical Models of Entanglement in Monitored Random Circuits", (2020), arXiv:2004.06736.

[78] A. Lavasani, Y. Alavirad, and M. Barkeshli, "Measurement-induced topological entanglement transitions in symmetric random quantum circuits", (2020), arXiv:2004.07243.

[79] S. Sang and T. H. Hsieh, "Measurement Protected Quantum Phases", (2020), arXiv:2004.09509.

[80] M. J. Gullans and D. A. Huse, "Dynamical Purification Phase Transition Induced by Quantum Measurements", Physical Review X **10**, 041020 (2020).

[81] M. Szyniszewski, A. Romito, and H. Schomerus, "Universality of entanglement transitions from stroboscopic to continuous measurements", (2020), arXiv:2005.01863.

[82] L. Zhang, J. A. Reyes, S. Kourtis, C. Chamon, E. R. Mucciolo, and A. E. Ruckenstein, "Nonuniversal entanglement level statistics in projection-driven quantum circuits", Physical Review B **101**, 235104 (2020).

[83] S. Choi, Y. Bao, X.-L. Qi, and E. Altman, "Quantum Error Correction in Scrambling Dynamics and Measurement-Induced Phase Transition", Physical Review Letters **125**, 030505 (2020).

[84] X. Turkeshi, R. Fazio, and M. Dalmonte, "Measurement-induced criticality in $(2+1)$-dimensional hybrid quantum circuits", Physical Review B **102**, 014315 (2020).

[85] M. J. Gullans and D. A. Huse, "Scalable Probes of Measurement-Induced Criticality", Physical Review Letters **125**, 070606 (2020).

[86] A. Nahum, S. Roy, B. Skinner, and J. Ruhman, "Measurement and Entanglement Phase Transitions in All-To-All Quantum Circuits, on Quantum Trees, and in Landau-Ginsburg Theory", PRX Quantum **2**, 010352 (2021).

[87] X. Cao, A. Tilloy, and A. De Luca, "Entanglement in a fermion chain under continuous monitoring", SciPost Physics **7**, 024 (2019).

[88] Q. Tang and W. Zhu, "Measurement-induced phase transition: A case study in the nonintegrable model by density-matrix renormalization group calculations", Physical Review Research **2**, 013022 (2020).

[89] S. Goto and I. Danshita, "Measurement-Induced Transitions of the Entanglement Scaling Law in Ultracold Gases with Controllable Dissipation", (2020), arXiv:`2001.03400`.

[90] O. Alberton, M. Buchhold, and S. Diehl, "Trajectory dependent entanglement transition in a free fermion chain – from extended criticality to area law", (2020), arXiv:`2005.09722`.

[91] O. Lunt and A. Pal, "Measurement-induced entanglement transitions in many-body localized systems", Physical Review Research **2**, 043072 (2020).

[92] N. Lang and H. P. Büchler, "Entanglement transition in the projective transverse field Ising model", Physical Review B **102**, 094204 (2020).

[93] X. Chen, Y. Li, M. P. A. Fisher, and A. Lucas, "Emergent conformal symmetry in nonunitary random dynamics of free fermions", Physical Review Research **2**, 033017 (2020).

[94] C. Liu, P. Zhang, and X. Chen, "Non-unitary dynamics of Sachdev-Ye-Kitaev chain", (2020), arXiv:`2008.11955`.

[95] Y. Fuji and Y. Ashida, "Measurement-induced quantum criticality under continuous monitoring", Physical Review B **102**, 054302 (2020).

[96] M. Ippoliti, M. J. Gullans, S. Gopalakrishnan, D. A. Huse, and V. Khemani, “Entanglement phase transitions in measurement-only dynamics”, (2020), arXiv:2004.09560.

[97] M. Van Regemortel, Z.-P. Cian, A. Seif, H. Dehghani, and M. Hafezi, “Entanglement entropy scaling transition under competing monitoring protocols”, (2020), arXiv:2008.08619.

[98] A. Lavasani, Y. Alavirad, and M. Barkeshli, “Topological order and criticality in (2+1)D monitored random quantum circuits”, (2020), arXiv:2011.06595.

[99] R. Vasseur, A. C. Potter, Y.-Z. You, and A. W. W. Ludwig, “Entanglement transitions from holographic random tensor networks”, Physical Review B **100**, 134203 (2019).

[100] Y. Li and M. P. A. Fisher, “Statistical Mechanics of Quantum Error-Correcting Codes”, (2020), arXiv:2007.03822.

[101] A. Kitaev and J. Preskill, “Topological Entanglement Entropy”, Physical Review Letters **96**, 110404 (2006).

[102] F. G. S. L. Brandão, A. W. Harrow, and M. Horodecki, “Local Random Quantum Circuits are Approximate Polynomial-Designs”, Communications in Mathematical Physics **346**, 397–434 (2016).

[103] E. Onorati, O. Buerschaper, M. Kliesch, W. Brown, A. H. Werner, and J. Eisert, “Mixing Properties of Stochastic Quantum Hamiltonians”, Communications in Mathematical Physics **355**, 905–947 (2017).

[104] J. Cotler, N. Hunter-Jones, J. Liu, and B. Yoshida, “Chaos, complexity, and random matrices”, Journal of High Energy Physics **2017**, 48 (2017).

[105] A. Nahum, S. Vijay, and J. Haah, “Operator Spreading in Random Unitary Circuits”, Physical Review X **8**, 021014 (2018).

[106] C. W. von Keyserlingk, T. Rakovszky, F. Pollmann, and S. L. Sondhi, “Operator Hydrodynamics, OTOCs, and Entanglement Growth in Systems without Conservation Laws”, Physical Review X **8**, 021013 (2018).

[107] J. Lopez-Piqueres, B. Ware, and R. Vasseur, "Mean-field theory of entanglement transitions from random tree tensor networks", (2020), arXiv:`2003.01138`.

[108] D. Rossini and E. Vicari, "Measurement-induced dynamics of many-body systems at quantum criticality", Physical Review B **102**, 035119 (2020).

[109] M. J. Gullans, S. Krastanov, D. A. Huse, L. Jiang, and S. T. Flammia, "Quantum coding with low-depth random circuits", (2020), arXiv:`2010.09775`.

[110] R. O'Donnell and J. Wright, "Quantum Spectrum Testing", in Proceedings of the forty-seventh annual ACM symposium on Theory of Computing, STOC '15 (June 2015), pp. 529–538.

[111] R. Islam, R. Ma, P. M. Preiss, M. Eric Tai, A. Lukin, M. Rispoli, and M. Greiner, "Measuring entanglement entropy in a quantum many-body system", Nature **528**, 77–83 (2015).

[112] C. Noel, P. Niroula, A. Risinger, L. Egan, D. Biswas, M. Cetina, A. V. Gorshkov, M. Gullans, D. A. Huse, and C. Monroe, "Observation of measurement-induced quantum phases in a trapped-ion quantum computer", (2021), arXiv:`2106.05881`.

[113] J. Z. Imbrie, "On Many-Body Localization for Quantum Spin Chains", Journal of Statistical Physics **163**, 998–1048 (2016).

[114] V. Ros, M. Müller, and A. Scardicchio, "Integrals of motion in the many-body localized phase", Nuclear Physics B **891**, 420–465 (2015).

[115] Y. Huang, Y.-L. Zhang, and X. Chen, "Out-of-time-ordered correlators in many-body localized systems", Annalen der Physik **529**, 1600318 (2017).

[116] R.-Q. He and Z.-Y. Lu, "Characterizing many-body localization by out-of-time-ordered correlation", Physical Review B **95**, 054201 (2017).

[117] B. Swingle and D. Chowdhury, "Slow scrambling in disordered quantum systems", Physical Review B **95**, 060201 (2017).

[118] X. Chen, T. Zhou, D. A. Huse, and E. Fradkin, "Out-of-time-order correlations in many-body localized and thermal phases", Annalen der Physik **529**, 1600332 (2017).

[119] R. Fan, P. Zhang, H. Shen, and H. Zhai, "Out-of-time-order correlation for many-body localization", Science Bulletin **62**, 707–711 (2017).

[120] I. MacCormack, M. T. Tan, J. Kudler-Flam, and S. Ryu, "Operator and entanglement growth in non-thermalizing systems: many-body localization and the random singlet phase", (2020), arXiv:`2001.08222`.

[121] A. Chandran, I. H. Kim, G. Vidal, and D. A. Abanin, "Constructing local integrals of motion in the many-body localized phase", Physical Review B **91**, 085425 (2015).

[122] L. Rademaker and M. Ortuño, "Explicit Local Integrals of Motion for the Many-Body Localized State", Physical Review Letters **116**, 010404 (2016).

[123] D. Pekker, B. K. Clark, V. Oganesyan, and G. Refael, "Fixed Points of Wegner-Wilson Flows and Many-Body Localization", Physical Review Letters **119**, 075701 (2017).

[124] A. K. Kulshreshtha, A. Pal, T. B. Wahl, and S. H. Simon, "Behavior of l-bits near the many-body localization transition", Physical Review B **98**, 184201 (2018).

[125] M. Goihl, M. Gluza, C. Krumnow, and J. Eisert, "Construction of exact constants of motion and effective models for many-body localized systems", Physical Review B **97**, 134202 (2018).

[126] A. Pal and D. A. Huse, "Many-body localization phase transition", Physical Review B **82**, 174411 (2010).

[127] D. J. Luitz, N. Laflorencie, and F. Alet, "Many-body localization edge in the random-field Heisenberg chain", Physical Review B **91**, 081103 (2015).

[128] E. V. H. Doggen, F. Schindler, K. S. Tikhonov, A. D. Mirlin, T. Neupert, D. G. Polyakov, and I. V. Gornyi, "Many-body localization and delocalization in large quantum chains", Physical Review B **98**, 174202 (2018).

[129]P. Calabrese and A. Lefevre, "Entanglement spectrum in one-dimensional systems", Physical Review A **78**, 032329 (2008).

[130]J. Cardy, "Linking Numbers for Self-Avoiding Loops and Percolation: Application to the Spin Quantum Hall Transition", Physical Review Letters **84**, 3507–3510 (2000).

[131]J. Jiang and C.-L. Yao, "Critical first-passage percolation starting on the boundary", Stochastic Processes and their Applications **129**, 2049–2065 (2019).

[132]A. B. Harris, "Effect of random defects on the critical behaviour of Ising models", Journal of Physics C: Solid State Physics **7**, 1671–1692 (1974).

[133]J. T. Chayes, L. Chayes, D. S. Fisher, and T. Spencer, "Correlation length bounds for disordered Ising ferromagnets", Communications in Mathematical Physics **120**, 501–523 (1989).

[134]S. Roy, J. T. Chalker, I. V. Gornyi, and Y. Gefen, "Measurement-induced steering of quantum systems", (2019), arXiv:`1912.04292`.

[135]J. Preskill, "Quantum Computing in the NISQ era and beyond", Quantum **2**, 79 (2018).

[136]T. Li and X. Wu, "Quantum Query Complexity of Entropy Estimation", IEEE Transactions on Information Theory **65**, 2899–2921 (2019).

[137]A. Nahum, J. Ruhman, S. Vijay, and J. Haah, "Quantum Entanglement Growth under Random Unitary Dynamics", Physical Review X **7**, 031016 (2017).

[138]A. Zabalo, M. J. Gullans, J. H. Wilson, R. Vasseur, A. W. W. Ludwig, S. Gopalakrishnan, D. A. Huse, and J. H. Pixley, "Operator scaling dimensions and multifractality at measurement-induced transitions", (2021), arXiv:`2107.03393`.

[139]L. Fidkowski, J. Haah, and M. B. Hastings, "How Dynamical Quantum Memories Forget", Quantum **5**, 382 (2021).

[140]S. Anders and H. J. Briegel, "Fast simulation of stabilizer circuits using a graph-state representation", Physical Review A **73**, 022334 (2006).

[141] M. Hein, J. Eisert, and H. J. Briegel, “Multiparty entanglement in graph states”, Physical Review A **69**, 062311 (2004).

[142] D. Fattal, T. S. Cubitt, Y. Yamamoto, S. Bravyi, and I. L. Chuang, “Entanglement in the stabilizer formalism”, (2004), arXiv:`quant-ph/0406168`.

[143] N. Kawashima and N. Ito, “Critical Behavior of the Three-Dimensional ±J Model in a Magnetic Field”, Journal of the Physical Society of Japan **62**, 435–438 (1993).

[144] Z. Koza and J. Po\la, “From discrete to continuous percolation in dimensions 3 to 7”, Journal of Statistical Mechanics: Theory and Experiment **2016**, 103206 (2016).

[145] X. Xu, J. Wang, J.-P. Lv, and Y. Deng, “Simultaneous analysis of three-dimensional percolation models”, Frontiers of Physics **9**, 113–119 (2014).

[146] A. Skal and B. Shklovskii, “Topology of an infinite cluster in the theory of percolation and its relationship to the theory of hopping conduction”, Sov Phys Semicond **8**, 1029–1032 (1975).

[147] D. Stauffer and A. Aharony, *Introduction To Percolation Theory : Second Edition* (Taylor & Francis, Dec. 2018).

[148] M. P. Gelfand and M. E. Fisher, “Finite-size effects in fluid interfaces”, Physica A: Statistical Mechanics and its Applications **166**, 1–74 (1990).

[149] M. M. Wolf, F. Verstraete, M. B. Hastings, and J. I. Cirac, “Area Laws in Quantum Systems: Mutual Information and Correlations”, Physical Review Letters **100**, 070502 (2008).

[150] J. A. Gracey, “Four loop renormalization of ${\ensuremath{\phi}}{̂3}$ theory in six dimensions”, Physical Review D **92**, 025012 (2015).

[151] T. Cormen, C. E. Leiserson, R. L. Rivest, and C. Stein, *Introduction to Algorithms*, Third (The MIT Press, 2009).

[152] K Binder, “Critical Behaviour at Surfaces”, in *Phase Transitions and Critical Phenomena*, Vol. 8, edited by C Domb and J Lebowitz (Academic Press, 1983).

[153] Y. Deng and H. W. J. Blöte, "Surface critical phenomena in three-dimensional percolation", Physical Review E **71**, 016117 (2005).

[154] B. Efron and R. J. Tibshirani, *An Introduction to the Bootstrap* (Chapman and Hall/CRC, May 1994).

[155] V. Gurarie and A. W. W. Ludwig, "Conformal algebras of two-dimensional disordered systems", Journal of Physics A: Mathematical and General **35**, L377–L384 (2002).

[156] J. Cardy, "Logarithmic conformal field theories as limits of ordinary CFTs and some physical applications", Journal of Physics A: Mathematical and Theoretical **46**, 494001 (2013).

[157] D. Gross, S. Nezami, and M. Walter, "Schur–Weyl Duality for the Clifford Group with Applications: Property Testing, a Robust Hudson Theorem, and de Finetti Representations", Communications in Mathematical Physics **385**, 1325–1393 (2021).

[158] D. A. Huse, R. Nandkishore, V. Oganesyan, A. Pal, and S. L. Sondhi, "Localization-protected quantum order", Physical Review B **88**, 014206 (2013).

[159] B. Bauer and C. Nayak, "Area laws in a many-body localized state and its implications for topological order", Journal of Statistical Mechanics: Theory and Experiment **2013**, P09005 (2013).

[160] N. Schuch, D. Pérez-García, and I. Cirac, "Classifying quantum phases using matrix product states and projected entangled pair states", Physical Review B **84**, 165139 (2011).

[161] A. C. Potter and R. Vasseur, "Symmetry constraints on many-body localization", Physical Review B **94**, 224206 (2016).

[162] A. C. Potter and A. Vishwanath, "Protection of topological order by symmetry and many-body localization", (2015), arXiv:`1506.00592`.

[163] W. De Roeck and F. Huveneers, "Stability and instability towards delocalization in many-body localization systems", Physical Review B **95**, 155129 (2017).

[164] K. De'Bell and J. W. Essam, "Series expansion studies of percolation at a surface", Journal of Physics C: Solid State Physics **13**, 4811–4821 (1980).